

# **Sedimentary processes and depositional environment of the distal part of the Bear Island Trough Mouth Fan, SW Barents Sea reconstructed from a giant piston core**

**Nora Dahl**  
*GEO-3900 Master's thesis in Geology*  
May 2016





## Abstract

Multi-proxy analyses of the giant piston core MD992301 (including lithostratigraphy, physical properties and XRF-scanning) and analyses of swath bathymetry data was integrated in order to reconstruct the glacial history and paleoenvironment of the distal parts of the INBIS channel, located between the distal Bear Island Trough Mouth Fan and Storfjorden Trough Mouth Fan. Based on the swath bathymetry data three main morphological features was identified. These features are interpreted to be upper slope gullies, debris lobes, and a larger channel identified as the INBIS channel and surrounding levees.

Core MD992301 was divided into 14 lithological units based on lithology, grain size, physical properties and geochemical elements comprising sediments from ~166,000 – 0 cal yr BP. The main sedimentary processes was sedimentation from suspension settling, mass-transport deposits and ice rafting from icebergs and sea ice, which is interpreted to be the dominating sedimentary processes within the area. The main sources of sediment were the Barents Sea Ice Sheet. Based on their distribution, the gravity flow activity in the area was restricted to periods of large-scale glaciation of the Barents Sea continental shelf.

The sedimentation rate was generally low, with the lowest values during interglacials. The estimated average sedimentation rate during LGM was estimated to be ~27.4 cm/kyr, and 5.5 cm/kyr during the present warm period, the Holocene.

The Barents Sea Ice Sheet may to have reached the outer Barents Sea continental shelf up to four times during the deposition of the MD992301 sediments. During these large-scale glaciations, the INBIS channel is believed to have been an important conduit gravity flows towards the deep sea. The onset of mass-transport within the MD992301 is hence assumed to be directly related to the activity within the proximal INBIS channel. These intervals are found to be during Saalian (MIS 6), Early Weichselian (5d and 5b) and Late Weichsel (MIS 2), where there is an increase in the frequency of turbidity currents during Last Glacial Maximum.



## Forord

Først vil jeg rette en stor takk til mine to veiledere Jan Sverre Laberg og Matthias Forwick. Takk for at døren alltid var åpen, for all hjelp, inspirasjon og kunnskap.

Innsamling av kjernemateriale ble utført av Leg  $\frac{3}{4}$  of the IMAGES V cruise by RV *Marion Dufresne* i 1999. Batymetrien brukt i oppgaven ble innsamlet av mannskapet på RV *Helmer Hanssen*. Radiokarbondateringer ble utført av Lucas Wacker fra Laboratory of Ion Beam Physics ved ETH Zürich, Sveits.

Ingvild Hald, Trine Dahl og Karina Monsen var veldig hjelpsomme i min periode på laben. Vil også rette en kjempestor takk til Ingrid, som hjalp med igangsettelsen av de ulike prosessene og XRF maskinen. Du er en knupp!

Jeg vil gjerne takke alle de fine folkene jeg har blitt kjent med i løpet av studietiden. Dere er en flott gjeng!

Kjære mamma, pappa, Birgit og bestemor. Tusen takk for gode samtaler, betryggende ord, oppmuntring og støtte gjennom de siste fem årene. Spesielt takk til Birgit, som holdt Knausen nogen lunde sivilisert det siste året, og som lagde to porsjoner middag.

Martin. Takk for at du er så tålmodig og har evnen til å si riktige ordene når jeg trenger det som mest. Du er best!

Tusen trillioner takk!

Nora Dahl

Tromsø, 15. mai 2016



## Contents

1. Introduction .....	1
1.1 Objectives .....	1
1.2 Background.....	1
2. Study area.....	3
2.1 Morphology .....	5
2.2 Marine Isotope stages .....	8
2.3 Oceanography and paleoceanography .....	9
2.3.1 Deep water formation .....	10
2.3.2 Paleoceanography .....	11
2.4 Pre-glacial tectonic and stratigraphic evolution of the Barents Sea continental margin	15
2.5 Glaciation history .....	15
2.5.1 The driving forces for the glacial fluctuations at the Barents Sea .....	15
2.5.2 Glaciation prior to the Weichselian .....	16
2.5.3 The last Ice Age – the Weichselian glaciation (117-11.5 ka) .....	18
2.5.4 Deglaciation of the Barents Sea .....	19
2.6 Deep sea sedimentary Processes and depositional environment .....	22
2.6.1 Deep sea sedimentary processes and depositional environment.....	22
2.6.2 Controlling factors on deep-water systems.....	23
2.6.3 Sediment transportation .....	23
2.6.4 Re-sedimentation processes .....	24
2.6.5 Processes during a glacial regime .....	35
2.6.6 Processes during interglacials .....	36
3. Material and methods .....	37
3.1 Swath Bathymetry .....	38
3.2 Laboratory work – Sediment cores.....	38
3.2.1. X-ray photography .....	39
3.2.2 XRF-scan .....	40
3.2.3 Multi Sensor Core Logging (MSCL).....	42
3.2.4 Magnetic susceptibility .....	43
3.2.5 Water content .....	43
3.2.6 Radiocarbon dating .....	43

3.3 Sedimentological description and logging .....	46
3.4 Grain size analysis .....	46
3.4.1 Sampling and preparation .....	46
3.4.2 Measurements and statistics.....	47
4. Results .....	49
4.1 Introduction .....	49
4.2 Swath bathymetry .....	50
4.2.1 Introduction.....	50
4.2.2 Gullies .....	53
4.2.3 Debris lobes .....	54
4.2.4 Channels.....	54
4.3 Core description.....	56
4.3.1 Lithology.....	56
4.3.2 Grain-size analysis .....	56
4.3.3 Physical properties .....	56
4.3.4 Element geochemistry.....	57
4.3.5 Radiocarbon dating .....	57
4.3.6 Visual description .....	58
4.3.7 Lithofacies.....	58
4.4 Lithology of core MD992301 .....	59
4.4.1 Unit 1 (1156- 1031 cm).....	63
4.4.2 Unit 2 (1031 – 999 cm).....	65
4.4.3 Unit 3 (999 – 961 cm).....	67
4.4.4 Unit 4 (961-943 cm).....	70
4.4.5 Unit 5 (943-937 cm).....	71
4.4.6 Unit 6 (937 -776 cm).....	73
4.4.7 Unit 7 (776 – 697 cm).....	74
4.4.8 Unit 8 (697-484 cm).....	77
4.4.9 Unit 9 (484-462 cm).....	79
4.4.10 Unit 10 (462 – 271/268 cm).....	80
4.4.11 Unit 11 (271/268 – 201 cm).....	82
4.4.12 Unit 12 (201 – 148 cm).....	85
4.4.13 Unit 13 (148 - 52 cm).....	86

4.4.14 Unit 14 (52 – 0 cm) .....	89
4.5 Chronology and sedimentation rate trough MD992301 .....	91
4.6 Summary .....	93
5. Discussion .....	95
5.1 Age model and sedimentation rates .....	96
5.1.1 Sedimentation rate MD992301 .....	96
5.1.2 Sedimentation rate compared to other areas .....	100
5.1.3 Summary .....	101
5.2 Paleoenvironment during deposition of Md992301 (0 - ~166,000 cal yr BP) .....	102
5.2.1 Part 1 .....	104
5.2.2 Part 2 .....	107
5.3 Glacial/interglacial history and paleoenvironment of the Barents Sea .....	113
5.3.1 Saalian (240,000 – 130,000: MIS 6) .....	113
5.3.2 Eemian (130,000 – 117,000: MIS 5e) .....	114
5.3.3 Early (117,000 – 74,000: MIS 5d-5a) and Mid-Weichsel (74,000 – 24,000: MIS 4-3) .....	116
5.3.4 Late Weichsel: Last glacial Maxima (24,000 – 17,000: MIS 2) .....	118
5.3.5 Deglaciation (17,000 – 11,500 MIS 2/1) .....	120
5.3.6 Holocene (11,500 – present: MIS 1) .....	122
5.4 Activity related to the INBIS channel .....	124
6. Summary and conclusion .....	127
7. Recommended further work .....	129
8. References .....	131
Appendix 1 .....	145



# 1. Introduction

## 1.1 Objectives

This master thesis was carried out at the Department of Geology, University of Tromsø - The Arctic University of Norway from August 2015 to May 2016. In the project a giant piston core taken on the southern channel levee of the INBIS channel system between Bear Island Trough Mouth Fan (TMF) and the Storfjorden TMF (Vorren et al., 1998) (figure 2a) was cored and analyzed in order to:

- Establish a lithostratigraphic log including the sediments physical and geochemical properties, and absolute dating of the cored interval,
- Describe the cored deposits, and
- Discuss the origin of the cored sediments, the sedimentary process involved and the paleoenvironment with focus on possible activity of the deep-sea channel.

## 1.2 Background

The area investigated in this study is located between the distal areas of the Bear Island TMF and Storfjorden TMF at 74°45.13 N and 010°00.82 E (figure 2a).

This area is interesting for several reasons: 1) The shelf troughs worked as drainage routes for paleo-ice streams of the Barents Sea Ice Sheet. Beneath the ice streams large amounts of sediments were transported to the shelf break/upper continental slope, subsequently released moving downslope towards the deep sea, during glacial periods (Laberg & Vorren, 1995). Most of these sediments accumulated as a glacial debris flow deposits on the Trough Mouth Fans at the mouth of troughs, 2) Some of these sediments however, were transported longer distances through channel systems including the INBIS channel system (Vorren et al., 1998), 3) So far, most studies has concentrated on the Bear Island and Storfjorden TMFs, very little is known on the activity and sedimentary processes of the INBIS channel system which is the focus of the present study.



## 2. Study area

The Bear Island TMF is located in front of a large transverse shelf through on the south western Barents Sea continental margin (figure 2a). It can be followed from the shelf break towards water depths exceeding 3000 meters where it merges with the abyssal plain in the Lofoten Basin (Laberg & Vorren, 1996b). The fan is about 750 km long and 150-200 km wide and covers a total area of 280,000 km<sup>2</sup>, limited by the Mohns and Knipovich spreading ridges towards west and northwest (Vorren & Laberg, 1997). The fan is divided into three morphological zones based on surface gradient changes; the upper fan is found from 500-1500 meters with an average gradient of 0.8°, the middle fan is extending from 1500 - 2200 meters with a gradient of 0.5° and dominated by a hummocky surface. The lower fan, from 2200 meters water depth and down to the abyssal plain has a gradient of 0.2° and is characterized by a slightly convex upward surface.

The Storfjorden TMF is located at the mouth of the Storfjorden Trough, at water depths of 400 – 2400 meters. This fan covers an area of ~35,000 km<sup>2</sup>, and has a radius of ~190 km (Vorren & Laberg, 1997). It is limited by the Knipovich spreading ridge to the west, and the Bear Island TMF to the south. The Storfjorden TMF is, like the adjacent Bear Island TMF subdivided into three morphological parts based on gradient. The upper fan: 1.8°, the middle fan: 1.0° and the lower fan: <0.2° (Laberg & Vorren, 1996a).

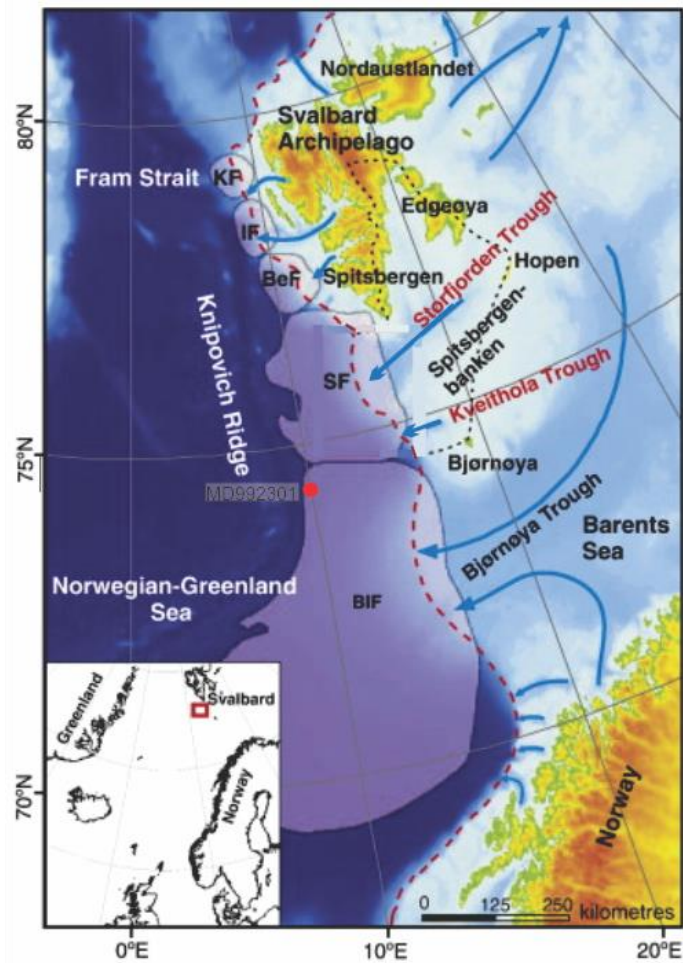


Figure 2a: Bathymetry map of the western Barents Sea obtained from the grid of the International Bathymetric Chart of the Arctic Ocean (IBCAO) (after (Jakobsson et al., 2008) (URL: <http://www.ibcao.org>)). Dotted red line: Regional LGM extent from (Landvik et al., 1998) and (Vorren et al., 1989). Blue arrows: Direction of flow of the main LGM ice streams draining the Svalbard/Barents Sea Ice Sheet according to Andreassen et al., (2008), Andreassen and Winsborrow (2009). Purple areas: extent of TMFs from Serjup et al., (2005): KF: Kongsfjorden Fan; IF: Isfjorden Fan; BeF: Bellsund Fan; SF: Storfjorden Fan; BIF: Bear Island Fan. Bold black dotted line: Inferred glacial drainage area of the Storfjorden-Kveithola depositional system. The red dot indicates the position of the core MD992301 (74°45.13 N and 010°00.82 E).

## 2.1 Morphology

The Norwegian continental margin is a passive continental margin that extends from about 62° N to 82°N. The margin includes the continental shelf (with a minimum outside Lofoten and Vesterålen: <10 km), the continental shelf break, and the slope towards the deep sea and the abyssal plane. The Norwegian-Greenland Sea is located west of the Barents Sea, and holds the Lofoten Basin where the Bear Island TMF and Storfrøden TMF are ebbing out, as well as the Mohns- and Knipovich spreading ridges forcing the Laurentian and Eurasian plate apart (figure 2.1a).

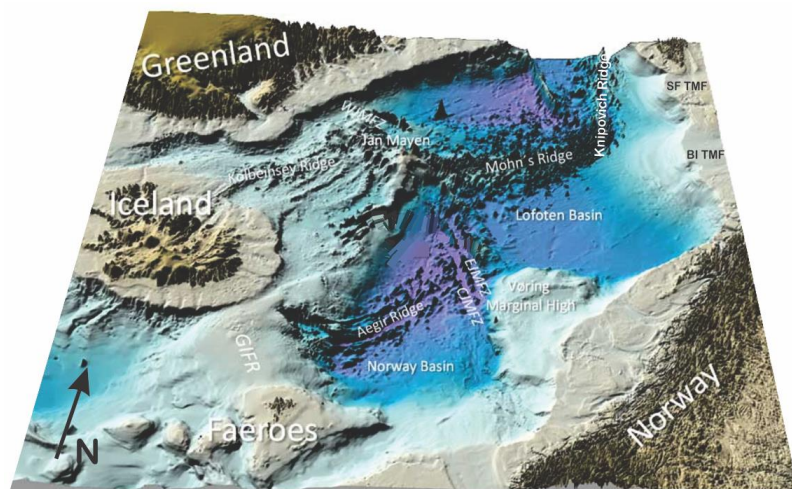


Figure 2.1a: Bathymetric map and main physiographic features of the Norwegian-Greenland Sea. (TMF= Trough Mouth Fan, JMFZ =Jan Mayen Fault Zone, WJMFZ = western Jan Mayen Fault Zone, EJMFZ = eastern Jan Mayen Fault Zone, CJMFZ = central Jan Mayen Fault Zone, GIFR = Greenland-Iceland-Faeroe ridge) (modified from (Gernigon et al., 2009).

The northernmost parts of the Norwegian Continental Margin holds the Barents Sea. The Barents Sea is an epicontinental sea that covers one of the largest continental shelves in the world (Solheim & Elverhøi, 1996). The subsurface bedrock of Jurassic, Cretaceous and Paleogene age (Bjørlykke et al., 1978) is overlaid by glacial sediments affecting the topography with structures made by large-scale glacial erosion throughout the late Cenozoic (Faleide et al., 1996; Solheim et al., 1998). The bathymetry is characterized of shallow banks at 100-200 meters water depth, separated by transverse, coast parallel troughs at water depths up to 500 meters (Solheim et al., 1998), where the largest trough is the Bear Island Trough extending in an E-W direction (figure 2.1b).

At the mouth of the troughs large trough mouth fans (TMFs) are formed due to large-scale accumulations of glacial material, and hence works as important paleoclimate archives. The TMFs along the continental margin are (from north to south): Kongsfjorden, Isfjorden,

Bellsund, Storfjorden, Kveithola and Bear Island TMF (Vorren & Laberg, 1997; Rebesco et al., 2012), where the Bear Island TMF is largest (Vorren & Laberg, 1997).

Between the TMFs canyons, channels and gullies are present, making incisions into the continental slope (Taylor et al., 2003).

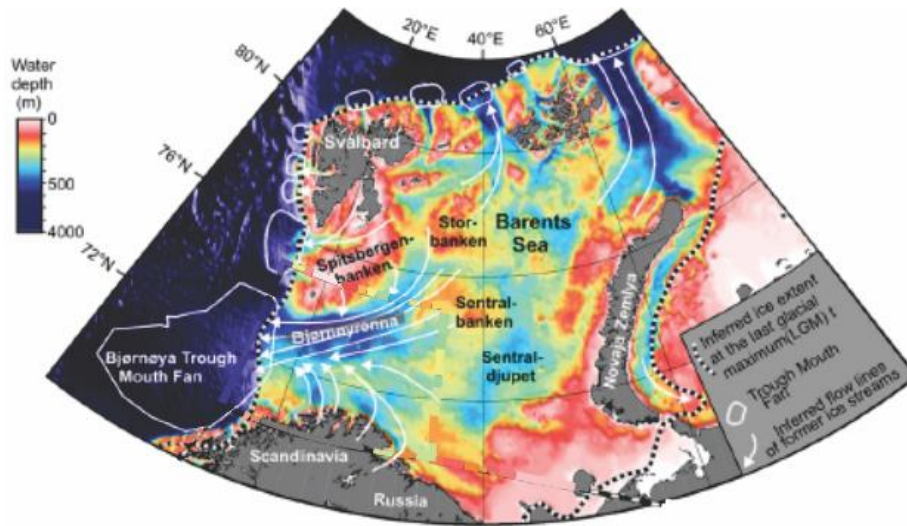


Figure 2.1b Bathymetry of the western Barents Sea (Jacobsson et al., 2000) The line indicates the ice extent during LGM, while the arrows indicates flow lines (Vorren et al., 1990; Landvik et al., 1998)

Deep-marine channels are rare along the continental margin, where the two most predominant ones are the INBIS channel and the Lofoten Basin Channel. The INBIS channel is located between the Bear Island TMF and Storfjorden TMF (figure 2.1c). It has been identified in water depths of 2360-2520 meters, and has a width of 5-15 km and is 60 km long having an east-west orientation (Vorren et al., 1998). The upper parts of the channel are buried under debris flow deposits originated from the Kveithola Trough, located between the Bear Island Trough and Storfjorden Trough. While the southern and deepest parts of the channel are bordered by debris flows on the Bear Island TMF (Laberg & Vorren, 1995). The northern flank of the channel is built up by a thicker layer of sediments and overbank deposits forming a natural levee with a height between 10-15 meters (Vorren et al., 1998).

At the mouth of the INBIS channel a ~50 km wide fan-like accumulation called the INBIS fan is interpreted. The flanks of the fan has sharp erosive channel incisions between 0.2-1 km wide and 5-10 meters deep which also have natural levees flanking the channel (Vorren et al., 1998). Submarine channels works as important conduits for mass-flows, especially turbidity currents from the continental margin towards the deep sea where the turbidity currents spreads out as a blanket over huge areas on the abyssal plane. The source area of the

sediments routed through the channel is anticipated to be the Kveithola Trough, the northern Bear Island TMF and the southern Storfjorden TMF (Vorren et al., 1998; Sauli et al., 2010).

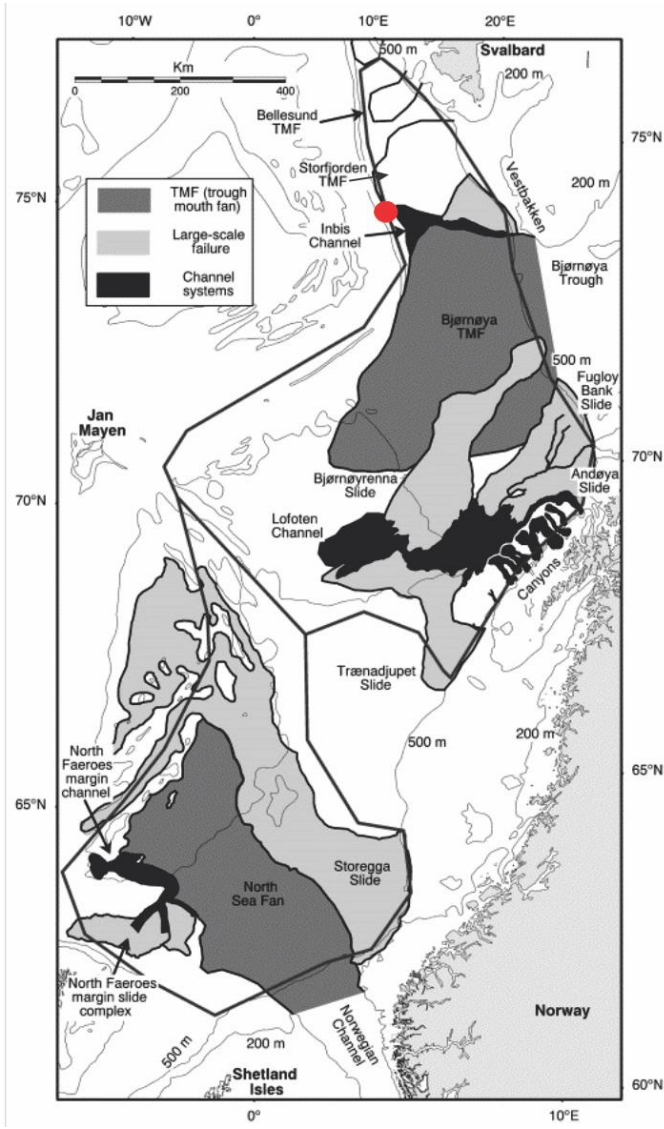


Figure 2.1c: Major sedimentary processes along the Lofoten and Norwegian Basins. Contours are at 200, 500 and 3000 meters water depth. The red dot indicates the approximately location of MD992301. (Modified from (Taylor et al., 2002)).

## 2.2 Marine Isotope stages

Marine isotope stages (MIS), marine oxygen-isotope stages, or oxygen isotope stages are alternating warm and cold periods in earth's paleoclimate based on oxygen isotope data reflecting changes in temperature derived from either ice cores or, as in this study from marine deep sea cores (Lowe & Walker, 1997).

Present is numbered as MIS 1, and by working backwards even number represents colder glacial periods with a higher oxygen-18 ( $^{18}\text{O}$ ), while odd-numbered stages with lower  $^{18}\text{O}$  values represents interglacials. The material used to collect data for sampling these values are called proxies, and may be pollen, foraminifera etc. Over 100 stages have been identified going back approximately 6 million years, where some of the stages are divided into sub-stages ex. MIS 5a and MIS 5b, where a, c, e are warmer periods and b, d and f represents colder intervals.

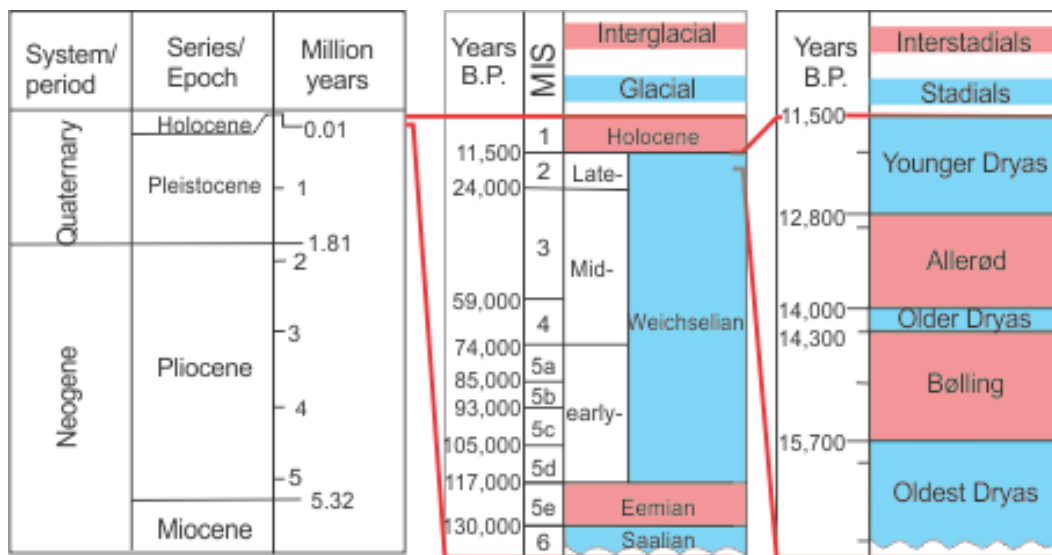


Figure 2.2a: to the left the division of the different systems/periods during the last 6 Ma years are shown, in the middle the interglacial and glacial periods with the given marine isotope stages for the last 140,000 years B.P. and to the right the subdivision into stadials and interstadials during the last ice age (modified from Lowe and Walker (1997)).

### 2.3 Oceanography and paleoceanography

The present oceanography along the Norwegian continental margin and the western Barents Sea is under the influence of three main water masses, the North Atlantic Surface Water, the Norwegian Coastal Current and the Arctic Surface Water (figure 2.3a). The inflow of warm and saline North Atlantic Surface Water (NAW) (>35 ‰) regulates the climate in the region, releasing heat into the atmosphere (Blindheim, 1990). Offshore Norway, at the Barents Sea Margin, the flow branches into two, one that can be followed into the southern Barents Sea and one continues northward following the Barents Sea slope north of Svalbard and into the Arctic Ocean under the pack-ice cover (Henrich et al., 1989; Hansen & Osterhus, 2000; Rudels & Friedrich, 2000; Slubowska-Woldengen et al., 2008).

Through the Fram Strait there is inflow of cold polar surface water (salinity <34‰ and temperatures <0°C (Swift, 1986)) and sea ice as the East Greenland Current (EGC). This current occupies a broad area along the eastern margin of Greenland and can be followed through the Denmark Strait (Henrich et al., 1989). In the area between the NAW and EGC, in the center of the Greenland-Iceland Sea, the formation of Arctic Surface Water (ASW) is initiated. The water mass has a variable temperature and lower salinity than the NAW, and defines the Oceanic Polar Front in the Norwegian-Greenland Sea (Henrich et al., 1989).

A lower salinity water (<35 ‰) with variable temperature flows northward along the coast of Norway as the Norwegian Coastal Current (NCC). The NCC is formed when the Atlantic water experiences a higher degree of input of continental drainage, freshening the saline Atlantic Water masses. The light coastal water spreads out in a wedge-form above the heavier underlying water. Mixing of the North Atlantic Surface Water and coastal current will reduce the density difference between the two adjacent water masses, creating a thermohaline structure preventing sea ice formation during winter (Sætre & Ljøen, 1972).

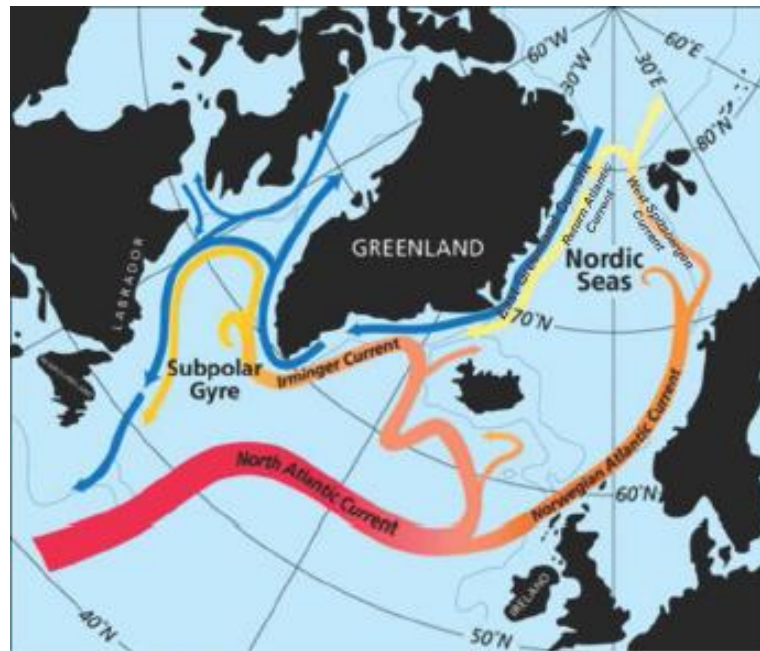


Figure 2.3a: Ocean circulation in the North Atlantic and Nordic Seas (adapted from (Watts, 2010))

The Norwegian Coastal Current (NCC) is not marked on the map, but is located between the Norwegian coast and the Norwegian Atlantic Current (NAC)

### 2.3.1 Deep water formation

In the high northern latitudes between Svalbard and Jan Mayen the Arctic Surface Water locally becomes so dense due to surface cooling that there is formation of deep water in the Norwegian-Greenland Sea. This cold, dense water sinks and fills the abyss of the Norwegian-Greenland Sea. The convention is thought to be one of the main driving forces in the global overturning cell in the world's oceans (Aagaard & Coachman, 1968). It is hence recognized that the magnitude and consistency of the North Atlantic Current (NAC) that transports warm, saline water into the Greenland-Iceland-Norwegian Sea through the Faeroe-Shetland channel (figure 2.3.1a), is important to the thermohaline balance and circulation patterns at high latitudes. Hence any changes in the North Atlantic are therefore likely to affect the thermohaline circulation and the climate in the region (Simonsen & Haugan, 1996). During winter, a regional overturning cell with dense surface water and less dense deep water in the Greenland-Iceland Sea may result in deep or intermediate convection and hence contribute to deep-water formation in the Norwegian-Greenland Sea (Johannessen, 1986; Swift, 1986).

The newly formed deep water leaves the Norwegian-Greenland Sea through the Denmark Strait and over sills between Iceland and Shetland, contributing to North Atlantic Deep Water (NADW) (Worthington, 1970). The sediments on the sea bottom reflects the circulation

pattern in the region (Kellogg, 1975), where coastal areas of Norway and Greenland are dominated by terrigenous clays and sands winnowed of the fine fraction by bottom current activity. While most of the sediments deposited on the shelf consist of relict Pleistocene material deposited by ice rafting or till (Vorren et al., 1984).

During cold glacial periods a weakening of the NAC, forces the watermass to become a subsurface water mass below the polar surface water masses (Rasmussen et al., 2007; Slubowska-Woldengen et al., 2008). The decrease in heat input initiates ice formation resulting in a southward shift in the convection and a southward expansion of the Arctic Ice. While an increase in the NAC leads to an increase in heat transportation to the northern latitudes and a decrease in ice cover (Aagaard & Coachman, 1968).

Due to the large income of Atlantic Water and cooling, the Barents Sea represent a heat and salt “sink” in the northern region. The heat loss and brine formation are causing an increase in density of the Atlantic Waters in the Barents Sea, and to the formation of deep water. The newly formed modified Atlantic Water enters the Arctic Ocean through an opening between Novaya Zemlya and Franz Josef Land, and enters the Kara Sea. While the outflow of the dense, cold bottom water back into the Norwegian-Greenland Sea takes place in the northern parts of the Bear Iceland Trough (Blindheim, 1989).

### 2.3.2 Paleoceanography

Paleoceanographic reconstructions done by Hebbeln et al., (1998) propose three different circulation modes in the Norwegian - Greenland Sea:

- 1) Interglacial circulation (like present) with a broad inflow of Atlantic waters.
- 2) Weak interglacial mode with only a narrow inflow.
- 3) Glacial mode with an isolated cold circulation cell in the Nordic Seas without influence of Atlantic water making a perennial sea ice cover.

The glacial mode covered most of the last 180 ka, with exception of Marine Isotope Stage (MIS) substages 5e, 5c, and 5a, 3 and 1 (Kellogg, 1980; Svendsen et al., 2004).

Further evidence were later collected, pointing on extensive periods with seasonally ice free waters in the Norwegian – Greenland Sea (Henrich et al., 1989; Gard & Backman, 1990; Hebbeln & Wefer, 1991; Hebbeln et al., 1994; Henrich et al., 1995; Hebbeln & Wefer, 1997; Hebbeln et al., 1998). A continuous meridional current system importing waters from the Atlantic Ocean and Arctic Ocean to the Nordic Seas were found, making up Arctic Water

masses (mix of Atlantic and Polar Waters), where the formation indicates a seasonally ice free conditions (figure 2.3.2a).

During MIS 6 and 2 under severe onshore glaciations some evidence of Arctic surface waters are found in cores from the central western Norwegian – Greenland Sea (figure 2.3.2a: b-c, f-i) . The Arctic Waters are in this periods fed by cool temperate Atlantic Waters, entering through the southeastern Norwegian – Greenland Sea submerged beneath glacial derived meltwater plumes (figure 2.3.2a: e-f).

Based on the previous paleoceanographic reconstruction in the Norwegian sea, an interpretation of a smaller ice sheet in Fennoscandia during Late Weichselian (MIS 2) than in Middle Weichselian (MIS 4 and 3.3) or Saalian (MIS 6) ice sheets are proposed (Hebbeln et al., 1998).

In MIS 5e a low carbonate and coccoliths accumulation indicated colder conditions, even though the substages are comparable to the warmer MIS 5a and Holocene (Kellogg, 1980). The possible explanation for this are interpreted to be a strong westward advection of Atlantic waters from the main inflow in the eastern Nordic Seas (Larsen et al., 1995). The migration is most likely due to intensification of the central gyres between Iceland and Greenland, leaving the entering Atlantic Water circulating between 66 - 76°N during MIS 5e by comparing the global pattern, MIS 5e was the warmest stage recorded the last 180 ka (CLIMAP, 1976, 1984) in the Nordic Seas. During Northward advection of the warm Atlantic waters transportation of subpolar plankton and iceberg from the North Atlantic and from the North Sea was transported as far north as 80°N. During these events, the open water provided huge amounts of moisture in the area. Combined with a cold environment, a growth of the ice sheets were initiated (Hebbeln et al., 1998), followed by an increase in the input of ice rafted debris (IRD) (Henrich events), reflecting a growth of the ice sheet.

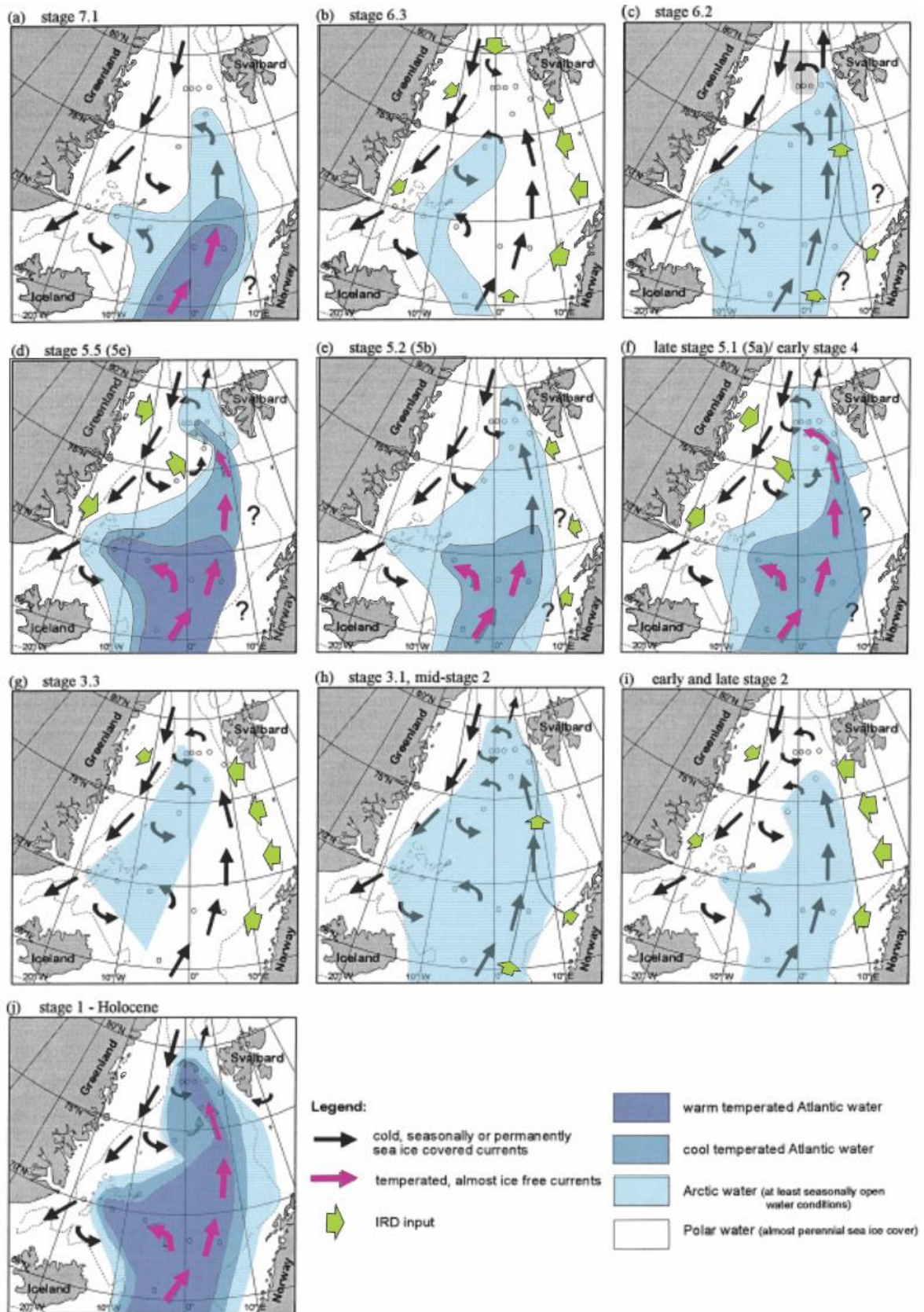


Figure 2.3.2a: Paleocceanographic reconstruction for the Nordic seas for selected time slices. The till masses indicates the water mass distribution during the different marine isotope stages. (Modified from Hebbeln et al., (1998).

In summary: In the last 180,000 years the western Barents Sea margin repeatedly experienced influx of warm Atlantic Water. The period of influx were characterized by an increased production of biogenic carbonate production and sub-polar water species, indicating seasonally open water. This periods seems to be synchronous in the North Atlantic and Arctic Ocean the last 60,000 years. In periods of year-around sea-ice cover and sluggish circulation the income of Atlantic water was reduced or absent. From the IRD content within cores the retrieved fluxes of meltwater can be correlated to the main glacial history in western Scandinavia and in the southwestern Barents Sea (Mangerud, 1991; Landvik et al., 1998). During deglaciation high productivity terminated, indicating a reduction in the polar North Atlantic forced by salinity. In general, advection of Atlantic Water partly correlate to the build-up and maximum phases of glaciation and partly to deglaciations. Deglaciation is hence initiated by the combination of heat supplied by Atlantic Water and insolation maximum (Hald et al., 2001) (figure 2.3.2b).

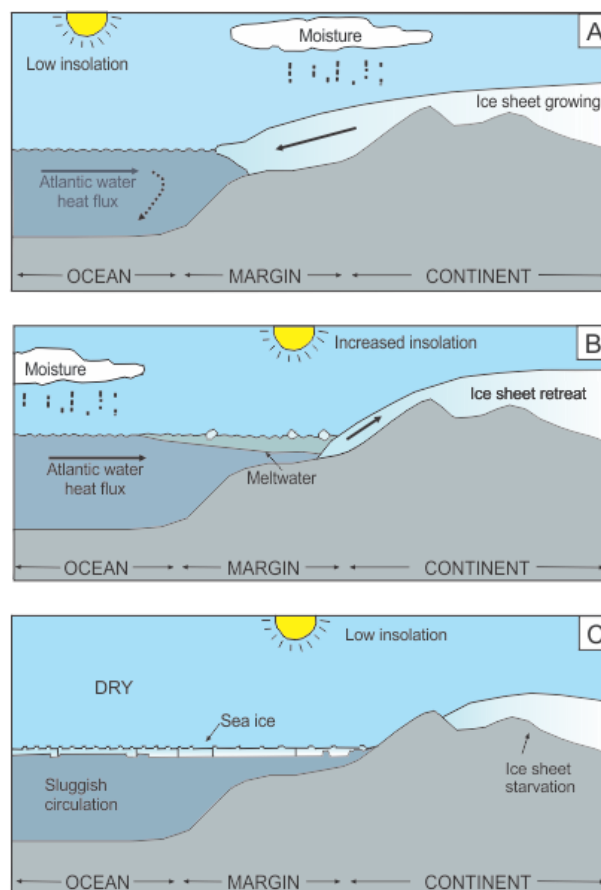


Figure 2.3.2b: Figure explaining the main oceanographic shifts and related glacial history from land via the continental margin to the deep ocean during the last interglacial-glacial cycle. A) Ice-sheet build up and thermohaline convection, B) major deglaciation phases with meltwater draining from the retreating (calving) ice sheet and reduced thermohaline convection, C) Cold phases with extensive sea-ice cover and reduces thermohaline convection. (Modified from Hald et al (2001))

## 2.4 Pre-glacial tectonic and stratigraphic evolution of the Barents Sea continental margin

Prior to the formation of the Norwegian-Greenland Sea in early Cenozoicum the sea area outside Norway was a part of an epicontinental sea between Fennoscandia, Svalbard and Greenland. In early Cenozoicum the seafloor was affected by extension, followed by seafloor spreading and the formation of the Norwegian-Greenland Sea from ca. 55 Ma BP (Gudlaugsson et al., 1998; Faleide et al., 2008).

In the start of the Oligocene there was a reorientation of the tectonic plates, making the movement of the Greenland-plate shift to a more westward direction, leading to seafloor spreading and the formation of new ocean crust along the mid-ocean ridge west of Svalbard. When older crust was cooled the increase in density makes the crust sink leading to deeper basin and deposition of thick sediment packages of the eroded material from the eastern (Barents Sea/Svalbard) isostatic rebounded parts (Faleide et al., 1996; Faleide et al., 2008).

The opening of the Norwegian-Greenland Sea made the Barents Sea drift away from Greenland due to the formation of two transform faults along the western margin, the Hornsund and Senja fault zones (Faleide et al., 2008). Movements along these zones lead to the formation of a transpressionzone, the West-Spitsbergen Fold Belt of western Svalbard. Magmatic activity was initiated between the two plates due to thinning, called the Vestbakken Volcanic Province. The eruptive activity was coeval with normal faulting and deposition of massive Eocene volcanic strata in the southwestern Barents Sea (Faleide et al., 2008).

## 2.5 Glaciation history

### 2.5.1 The driving forces for the glacial fluctuations at the Barents Sea

Glacial fluctuations are the result of an interplay between climate, insolation, precipitation, ocean currents and other processes. Where the glaciers grows due to accumulations (mainly precipitation) and/or if ablation (melting and calving) decreases. A colder climate has a lower moisture, hence the annual precipitation in the area becomes limited. This has for longer periods been considered the main attribute restricting ice sheet growth in the Arctic region (Boulton, 1979). In long periods during Weichselian, the cold climate lead to precipitation as snow even during summer (Mangerud & Svendsen, 1992). As the equilibrium line is submerged below the sea, the snow covered the land surface. Regression of the sea due to heavy glaciations participated in exposing shallower parts of the Barents Sea shelf for further

ice accumulation (Denton & Hughes, 1981).

The source of moist and waves in the area is reconstructed by (Dokken & Hald, 1996; Hald et al., 2001), which states that significant proportions of the Nordic Seas were seasonally ice free during MIS 4 and MIS 2, and may hence have contributed with moist to the region.

The main driving force, forcing fluctuation between glacial-interglacial periods are changes in the orbital configuration (Milankovitch theory) (Lowe & Walker, 1997) and the major glacial advances follows the obliquity cycles (Mangerud et al., 1992; Mangerud et al., 1996).

Glaciers expanded in periods of low tilt of the earth axis. By comparing the Milankovitch cycles and previous glaciations: glacial maximum were delayed behind minimum tilt, and the deglaciation was initiated just before maximum tilt. However, the climatic response has several errors, with feedback loops and delay mechanisms, the expansion of the ice hence is assumed to be in periods with low summer insolation and the aerial dominance of ablation/accumulation in the area (Mangerud & Svendsen, 1992).

### 2.5.2 Glaciation prior to the Weichselian

High latitudes are affected by repeated episodes of glacial activity, effecting the nature and rates of all sedimentary processes (Taylor et al., 2000). An increase in glacial activity leads to large contributions of glacial meltwater, influencing the ice stream motion, lubrication and also affects the behavior of mass wasting processes (Eyles, 2006). The glaciated continental margin of the Barents Sea have been prograding to its present position, and has a variable relief with both depositional and erosional structures. In glacial periods the Barents Sea was covered with ice bulldozing and deposit huge amounts of glacial material on the outer continental shelf and the upper part of the continental slope. Due to the rapid depositional rate these deposits are highly unstable, and the glacial derived material may result in excess pore pressure within the sediments underlying the glacial package (Laberg & Vorren, 1995; Elverhøi et al., 1997; Elverhøi et al., 2002).

Based on analyzed ice rafting debris (IRD) the oldest indications of glaciations in the northern hemisphere are interpreted to have been on Greenland during middle- to late Miocene (Thiede et al., 1998). In the Barents Sea glacial activity was restrained until ~2.7 Ma (Knies et al., 2002). At this period the presence of IRD within cores indicated the appearance of the larger, regional ice cover in the area for the first time, the Barents Sea Ice Sheet (Landvik et al.,

1998). Prior to this, the ice cover in the region was restrained to continental areas only (Solheim et al., 1998).

At ~2.6 - 2.3 Ma there was a marked increase in length and frequency of the glaciations, corresponding to stadial-interstadial cycles (Faleide et al., 1996; Butt et al., 2000). In this period fluvial and glaciofluvial erosional processes dominated the region (Laberg et al., 2012). By interpreting the deposited sediments from this time interval, clear indications of a warm, tempered and dynamic ice were found by Laberg et al., (2010). Although the ice sheet did not extend all the way out to the continental shelf edge during this period, huge amounts of erosional products were deposited along the continental margin (Butt et al., 2000; Laberg et al., 2010). By interpreting the seismic stratigraphy and IRD deposits from various cores, it has been inferred that the ice sheet reached the shelf break for the first time around 1.6 Ma (Shipboard Scientific Party, 1996).

In late Pliocene/early Pleistocene a net erosion of the Barents Sea continental shelf of 170-230 meters are estimated, leaving an erosional rate of 0.15-0.2 mm/yr (Rasmussen & Fjeldskaar, 1996). On the Bear Island TMF the estimated sedimentation rate is assumed to be 16-22 cm/kyr (Laberg et al., 2012), giving a total volume of  $\sim 235 \times 10^3$  (Vorren et al., 1991) or  $99 \times 10^3$  (Faleide et al., 1996) sediments with an assumed source area of 567,000 km<sup>2</sup> (Vorren et al., 1991).

At the end of early Pleistocene (1.5-0.7 Ma) the climate turned colder, resulting in the extent of a larger ice cover over the Barents Sea continental margin (Andreassen et al., 2007). Due to the onset of a larger ice cover, the net erosion increased to 220-420 meters, at a rate of 0.4-0.5 mm/yr (Laberg et al., 2012). The total amount of erosional material is hence assumed to be  $242 \times 10^3$  km<sup>2</sup> (Vorren et al., 1991) or  $191 \times 10^3$  km<sup>3</sup> (Faleide et al., 1996), deposited along the shelf and upper slope resulting in several mass wasting events and the formation of erosional channels (Piper et al., 1999).

One of the largest ice covers recorded from the Barents Sea was initiated during middle Pleistocene (240,000 – 130,000 cal yr BP.), the Saalian glaciation (Mangerud et al., 1998) (figure 2.5.2a). Ice advance started in this area at 180,000 cal yr BP and reached the maximum expansion at ~155,000 cal yr BP (Lambeck et al., 2006). The maximum expansion was followed by retreat and readvance during the Saalian, which ended ~130,000 cal yr BP. The net erosion in this period is estimated to 440-530 meters, with an rate of 0.6-0.8 mm/yr

(Laberg et al., 2012). An estimated amount of  $87 \times 10^3 \text{ km}^3$  (Vorren et al., 1991) or  $106 \times 10^3 \text{ km}^3$  (Faleide et al., 1996) of sediment was deposited within this period.

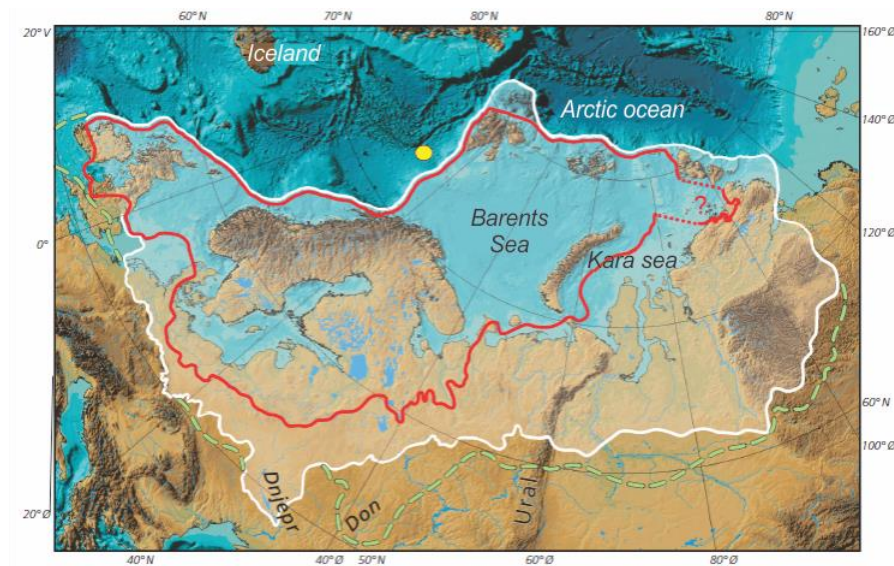


Figure 2.5.2a: Extent of the last two major glaciations of the Scandinavian Continental Ice and The Barents Sea ice Sheet. White line shows extent during Saale ~130.000 years ago. In red is the maximal extent of the ice during Weichsel, with green is the outermost line where the ice didn't reach in Saalian. The yellow dot indicates the approximately location of core MD992301. (Modified from (Svendsen et al., 2004))

### 2.5.3 The last Ice Age – the Weichselian glaciation (117-11.5 ka)

During the last 117 ka. three glacial maximum of the Eurasian ice cover has been suggested:

- 1) Early Weichselian (117,000-74,000 cal yr BP: MIS 5d), 2) Mid-Weichselian (74,000-24,000 cal yr BP: MIS 4), and 3) Late-Weichselian (24,000 -11,500 cal yr BP: MIS 2)
- (Mangerud et al., 1998; Mangerud, 2004; Svendsen et al., 2004) (figure 2.5.3a).

The early Weichselian at ~117,000 – 74,000 cal yr BP was dominated by an eastern ice sheet in the Kara Sea with a smaller ice cover in Scandinavia. This period hence defines glacial maximum in the east (Svendsen et al., 2004).

In Mid-Weichsel there were two prominent advances of the ice sheet (Larsen et al., 2006). The first one, occurred from 74,000 – 59,000 cal yr BP. In this period the Barents Sea Ice Sheet was connected to the Scandinavian Ice Sheet. The second advance has been dated to 55,000 - 45,000 cal yr BP.

During Last Glacial Maximum (24,000 – 11,500 cal yr BP) the ice reached its full extent over Scandinavia and the Barents Sea (Siegert et al., 2001) (figure 2.5.2.3a). It is suggested that the

ice sheet reached the shelf break two times during this period (Laberg & Vorren, 1995). The first maximum was at ~22,000 cal. yr. BP (calibrated years before present) and the second after ~19,000 cal. yr. BP (Vorren & Laberg, 1996).

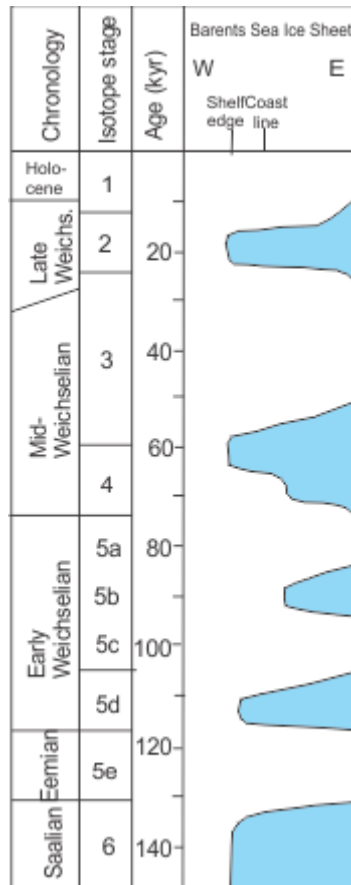


Figure 2.5.3a: Time-distance diagram showing the growth and decay of the Barents Sea Ice Sheet the last ~150,000 kyr. (modified from (Mangerud et al., 1998))

#### 2.5.4 Deglaciation of the Barents Sea

The glacial geomorphology indicates spatial and temporal variations in the ice dynamics, where there are evidences of both active ice streaming and frozen-bed conditions at both maximal glacial extent and during phases of deglaciation (Winsborrow et al., 2010).

The deglaciation of the Barents Sea has been subdivided into 5 stages which represent the last glacial maximum and the following deglaciation (Winsborrow et al., 2010) (figure 2.5.4a).

1) Stage one represents the Late Weichselian glacial maximum. In this period the ice sheet covered the entire Barents Sea Shelf, and the Bear Island ice stream was one of the main draining conduit in the area (Andreassen & Winsborrow, 2009; Winsborrow et al., 2010) (figure 2.5.4a: a).

2) The first phase of the deglaciation began at ~17,500 cal. yr. BP (Vorren & Laberg, 1996) with significant retreat of the ice margin in the western Barents Sea followed by a re-advance within the Bear Island Ice Stream (figure 2.5.4a: b). The ice stream were fed by land derived tributaries (Winsborrow et al., 2010).

3) During stage three there was a change in the ice dynamics of the ice sheet. The center of the maximum ice volume shifted to a more eastern position (figure 2.5.4a: c), making most of Tromsøflaket and the Bear Island Trough ice free (Winsborrow et al., 2010), while the Djuprenna Through Ice Stream and the Nordkappbanken-east that were fed by ice flowing north from the Kola Peninsula remained active and had a readvance (Winsborrow et al., 2010). This stage is dated to ~16,000 cal. yr. BP (Winsborrow et al., 2010).

4) Stage four was dated to ~15,000 cal. yr. BP (Winsborrow et al., 2010) based on dates indicating glaciomarine conditions by 14,900 cal. yr. BP north of the Kola Peninsula (Polyak et al., 1995). In this stage the southern Barents Sea was ice free and the new ice margin was now located in the outer-fjord areas in northern Norway (figure 2.5.4a: d).

5) A significant westward ice retreat on the Kola Peninsula, while the ice margin continued southwards in northern Norway was dominating in the fifth step of the glaciation (Winsborrow et al., 2010). This stage has been compared with the Tromsø-Lyngen moraine and esitimated to an age of ~12,500 cal. yr. BP (Vorren & Plassen, 2002) (Figure 2.5.4a: e).

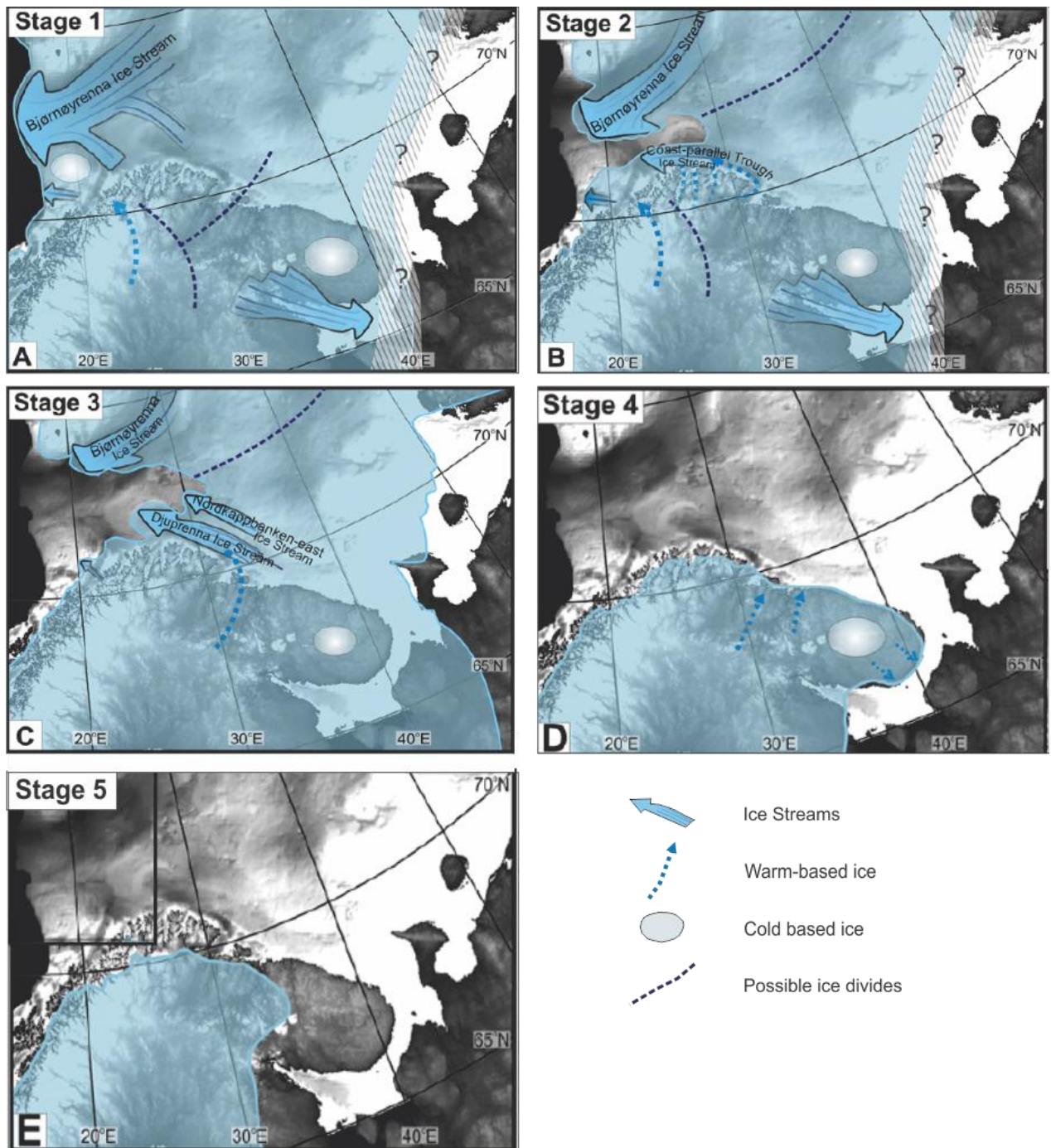


Figure 2.5.4a: Illustration over the stepwise deglaciation of the Barents Sea Ice Cover. (Modified from Winsborrow et al., 2010)

## 2.6 Deep sea sedimentary Processes and depositional environment

In the following subchapter the sedimentary processes and depositional environment in the deep sea will be described.

### 2.6.1 Deep sea sedimentary processes and depositional environment

Depositional environment or sedimentary environment describes the combination of physical, chemical and biological processes within a specific area. Deep sea processes includes processes along the continental slope: mass-wasting events, suspension fall out and glaciomarine sedimentation (figure 2.6.1a).

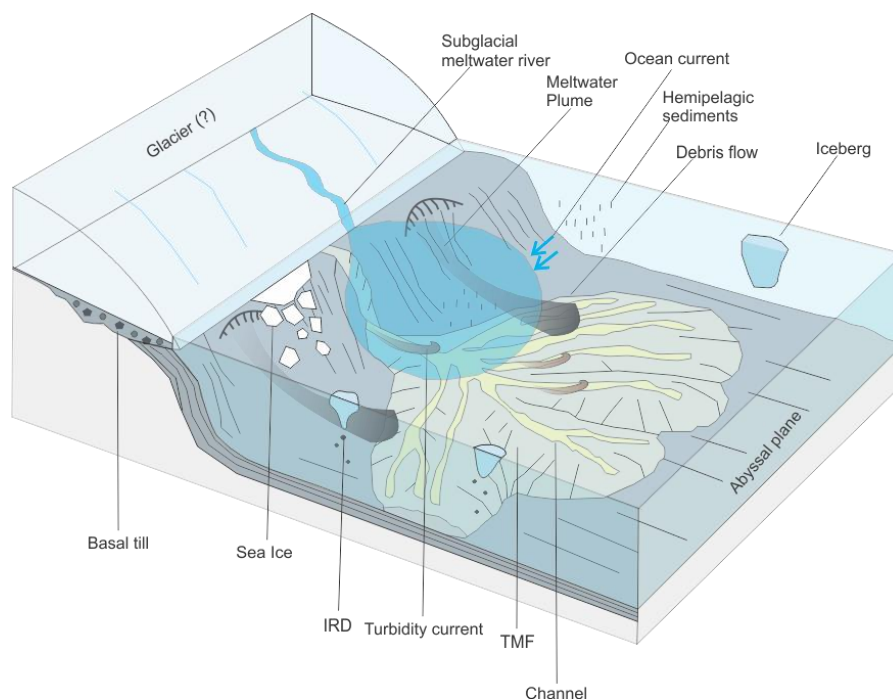


*Figure 2.6.1a: Principal illustration over the main sedimentary processes found in a deep sea environment.*

Due to extensive glaciation of the Norwegian continental margin most of the sediments deposited in the sedimentary basins are of glacial origin. The glacial derived material is primary deposited along the continental shelf break before it is transported further and redeposited as mass transport deposits. On the Barents Sea slope, a number of debris flows containing glacial material have been identified (Laberg & Vorren, 1996a). In addition, some sandy turbidites, interrupted by glaciomarine sediments containing IRD (Svindland & Vorren, 2002).

## 2.6.2 Controlling factors on deep-water systems

### 2.6.2.1 Sediment staging areas

Sediment staging areas or source area are defined as the shelf and/or upper slope location where mass flows may originate. The sediment found in the stage area is delivered by fluvial, aeolian, and longshore drift in low latitudes. While at high latitude, as the Norwegian continental margin most of the sediments were probably derived from an ice sheet at or near the shelf break during full glacial conditions. In this study the Barents Sea ice sheet is believed to be the main contributor (Vorren et al., 1998; Svindland & Vorren, 2002).

### 2.6.2.2 Canyons and slope channels

Following the release of sediments onto the outer shelf, canyons and slope channels acts as conduits for sediments from the shelf edge towards the deep sea (Gales et al., 2013; Amundsen et al., 2015). Canyons and channels are erosive features made by four main processes 1) as a consequence of hyperpycnal subglacial meltwater at or near the shelf break (Pedrosa et al., 2011), 2) by erosion from mass-flows (Piper et al., 1999), 3) by cold bottom currents derived from a nearby ice cap during glaciations (Pedrosa et al., 2011), or 4) formed during interglacials by cold water from the shelf (Vorren et al., 1989).

Based on mode of confinement and levee formation channels and canyons are separated. A canyon fully confine a flow and hence don't have any levee formations, while a slope channel only partially confine the flows, and provide levees. If a flow is fully confined further erosion into the substrate is more easily achieved (Nichols, 2009). Low-latitude canyons are typically river-fed during low sea-level stand, while high-latitude canyons has their main sediment input away from large-river system mostly and derives reworked glacial material (Vorren et al., 1998; Laberg et al., 2007) .

## 2.6.3 Sediment transportation

### 2.6.3.1 Gravity

Gravity is the main driving force for downslope sediment movement, both in sub arid and subaqueous settings. Under the influence of gravity unstable sediments will be able to travel to an area of higher stability, depositing material both on the continental slope, continental rise, and abyssal plane (Nichols, 2009).

### 2.6.3.2 Density

Density differences play an important role in sediment transportation (Nichols, 2009). When it comes to water, heavier water masses (lower temperature and increased salinity) will move along the bottom downslope, while lighter water masses will end up in a plume on the top of the water. The density of water is also influenced by the load of sediment, where a higher load will increase the density and hence increase the acceleration rate downslope (e.g. turbidity currents). If a hypopycnal plume (less dense) i.e. glacial meltwater plumes contains sediments they will fall out of suspension due to a rapid decrease in acceleration as the plume enters still water, and settle on the bottom (Mulder & Alexander, 2001).

### 2.6.3.3 Ice

Icebergs and sea ice incorporate huge amounts of sediment, both from scouring the underlying bedrock, redeposition of sediments, rock fall and by aeolian activity. These processes are mostly active during glacial periods where sediments are deposited as IRD along the continental margin and deep sea. Due to the distal location and high-latitude position of the studied core, iceberg and/or sea ice transportation and deposition is thought to be an important transportation method of the sediments and clasts seen within MD992301.

## 2.6.4 Re-sedimentation processes

Various re-sedimentary processes are active in the marine setting. The mode of re-sedimentation changes in importance between glacial and interglacial periods. The deep marine environment where MD992301 is retrieved, is complex with respect to the sedimentary processes involved. The processes listed in the following subchapters are the main processes found along a high-latitude continental slope.

### 2.6.4.1 Slides:

A slide is a down-slope movement of material that occurs along a sliding plane (surface of rupture), representing a zone of weakness. The material remains mostly undisturbed as it moves downslope, containing much of its original bedding (figure 2.6.4.1a) (Lutgens & Tarbuck, 2009). A slide often evolves into a slump in a marine setting and is hence unusual to find deposits which reassemble a slide.

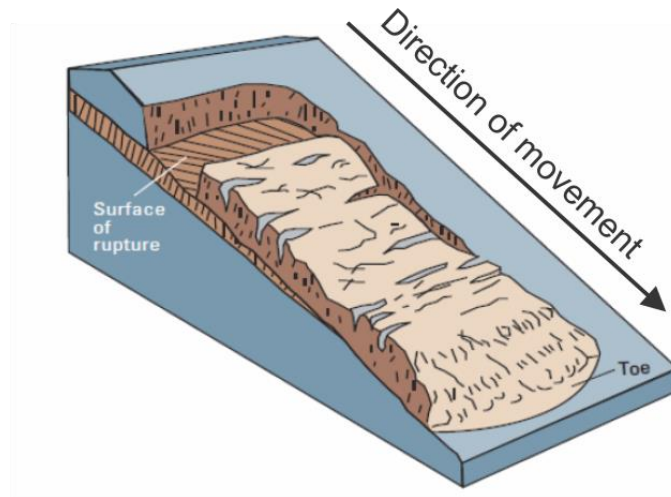


Figure 2.6.4.1a: Figure showing the principle of slides (adapted from (Highland & Bobrowsky, 2008)).

#### 2.6.4.2 Slumps:

A slump often develops from a slide, as the material is more stirred and travels as a mass with a laminar flow behavior (figure 2.6.4.2a). Slumping is initiated by failure along weaker layers and comprises a large category of variously deformed sediments. These deposits are often describes a chaotic, unbedded units extending form meters to tens of meters in thickness (Lutgens & Tarbuck, 2009). The depositional rate is hence assumed to be rapid. The transport distance can vary from a few meters to hundreds of kilometers, and may be identified as a debris flow. While some slumps may have a remarkably increase in turbulence and evolve into a turbidity current (Collinson et al., 2006; Nichols, 2009; Shanmugam, 2012a).

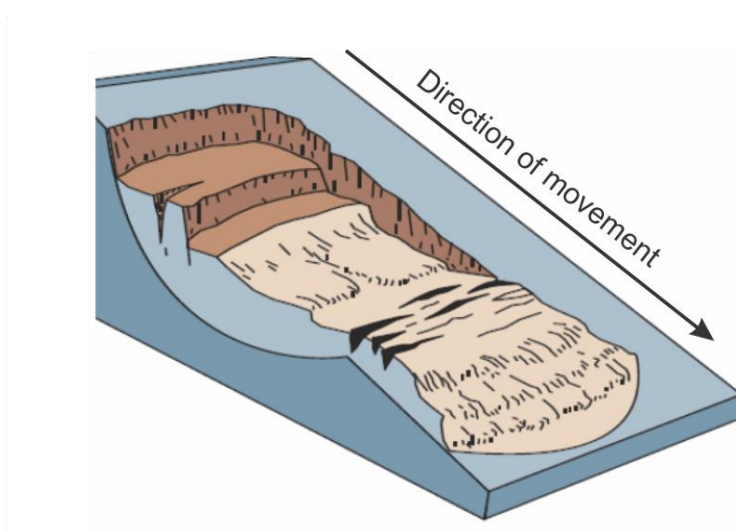


Figure 2.6.4.2a: A figure showing the principle of slumps (adapted from Highland and Bobrowsky (2008)).

### 2.6.4.3 Debris flows:

When there is a high concentration of sediments of any size extending the water proportion making it more viscous it can develop into a debris flow (figure 2.6.4.3a). The high density of the mixture makes it move under the effect of gravity towards a lower relief. The fluid dynamics of a debris flow is laminar, where all the particles moves parallel to each other. Due to the linear flow, the sediments remain unsorted when deposited. The flow diminish as it freezes due to a high internal friction. It may therefore be only smaller changes in the thickness and lithology of the deposits from its proximal to distal areas (Nichols 2009). The volume of a debris flow can extend 10s of km<sup>3</sup> and deposit sediments all the way from a few mm to 10s m in thickness. During movement, both the top and bottom of the flow may incorporate water, making it more diluted and develop into a turbidity current, with a turbulent flow pattern described below (Piper et al., 1999; Nichols, 2009). In a high-latitude marine environment debris flows (glacigenic debris flows) are often deposited as lobes with a positive relief. They are often present on the surface of submarine fans on glaciated continental margins e.g. the Bear Island TMF and Storfjorden TMF.

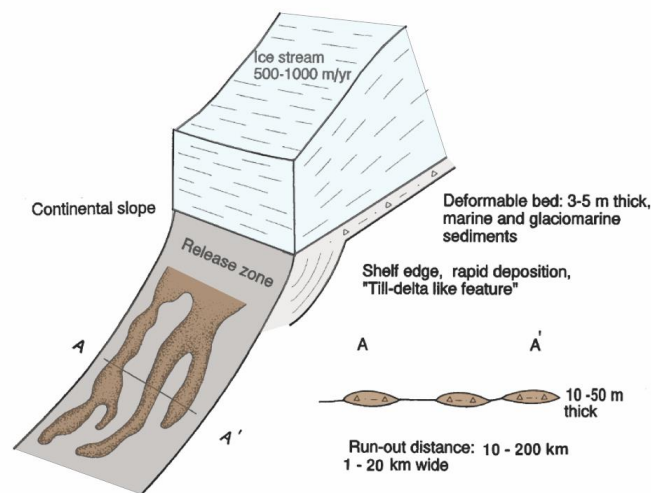


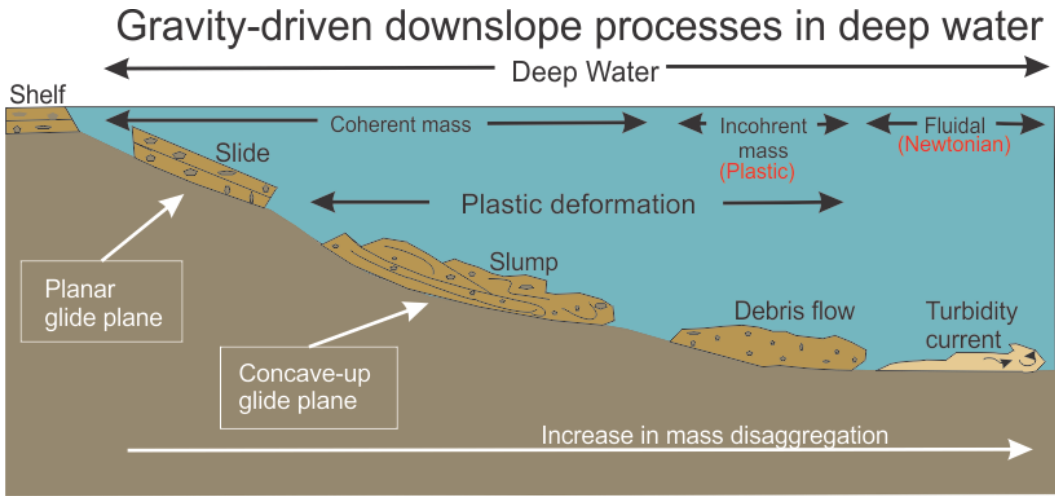
Figure 2.6.4.3a: Model illustrating the sediment dynamics beneath and in front of an ice stream and the geometry of the debris lobes on the high-latitude fans (modified from (Elverhøi et al., 1997)).

### 2.6.4.4 Turbidity currents:

Turbidity currents are a gravity flow where the density differences to the surrounding makes the current flow. The material within a turbidity current is kept in suspension due to turbulence (Leeder, 2011), leading to a mass significantly lower density than debris flows described in chapter 2.6.4.3. These turbidity currents can transport clast in any size from clay

to pebbles, while the turbulence makes the material sorted, with larger and heavier material on the bottom, and smaller and lighter material towards the top. The volume of a turbidity current may be up to 10s of km<sup>3</sup> and deposit huge amounts of sediments from mm to 10s of meters in thickness. The current diminishes when the depositional rate exceeds the erosional rate, making the current decrease in size (Collinson et al., 2006; Nichols, 2009).

A turbidity current may origin in several ways: 1) By the transformation of slide, slumps or debris flows (as described above) (figure 2.6.4.4a), 2) from a river outflow where the plume has a hyperpycnal flow with a higher density than the surrounding water mass, 3) from ignitive flows in submarine canyons, or 4) due to storm surges causing turbidity currents on the shelf and from input of meltwater from ice sheets (Kneller & Buckee, 2000; Meiburg & Kneller, 2010; Leeder, 2011). The transition from a subaqueous debris flow to a turbidity current involves dilution of the debris flow, reducing the flows density from 2.0 g/cm<sup>3</sup> in a debris flow to 1.1 g/cm<sup>3</sup> in a turbidity current (Hampton, 1972), where the amount of mixing and size of the turbidity current is dependent on the strength of the debris flow.



Sediment concentration: 100% of volume	25-100%	1-23%
Water concentration: 0% of volume	0-75%	77-99%
Mechanical behavior. Elastic and plastic		Viscous Fluid
Sandy mass-transport deposits Sand concentration: >20% of volume		Turbidite

Figure 2.6.4.4a: Modell showing gravity-driven downslope processes in deep water (modified from Shanmugam 2012a)

Turbidity currents that travel down slope are subdivided into three: head, body and tail (Nichols, 2009) (figure 2.6.4.4b). The head contains the coarsest material and erodes the ground as it moves down, forcing material up in suspension which mixes with the surrounding fluids. This newly suspended material gets incorporated in the body or tail of the flow. Due to the diluting of the flow with incorporation of water the density differences with the surroundings decrease. This causes the velocity to diminish and the sediments fall out of suspension, mainly in the body and tail (Kneller & Buckee, 2000; Nichols, 2009; Leeder, 2011).

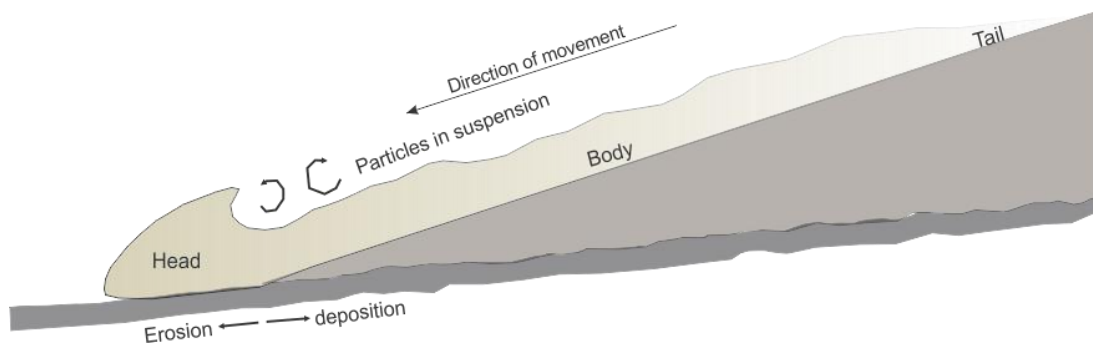


Figure 2.6.4.4b. Principal figure showing the subdivisions of a turbidity current: Head, Body and Tail.

Sediments deposited by a turbidity current are called turbidites that have distinct characteristics (especially in low- and medium-grained deposits) called the “Bouma Sequence” (figure 2.6.4.4c). The sequence subdivides the deposits into 5 subdivisions ( $T_a$ - $T_e$ ) (Bouma, 1962; Walker & Phil, 1965; Nichols, 2009; Leeder, 2011). The characteristics of the subdivisions are listed below.

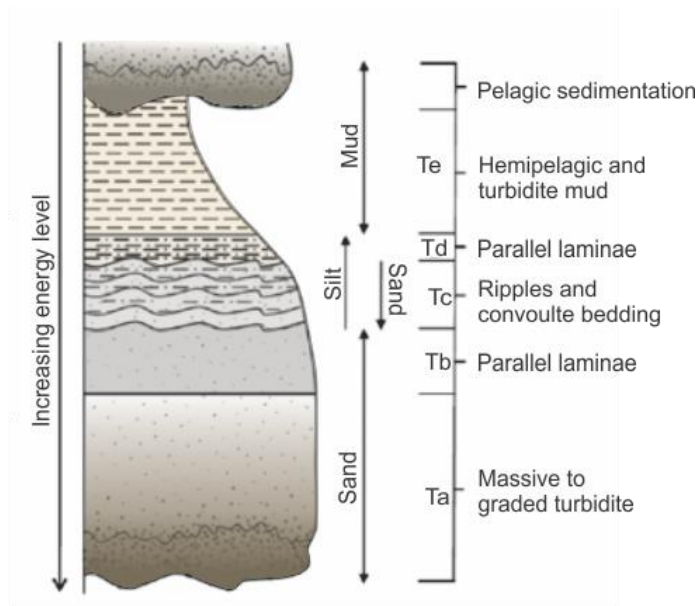


Figure 2.6.4.4c: The figure shows an ideal Bouma sequence, ranging from Ta at the bottom and Te on the top.  
(Modified from Bouma (1962) and Walker (1965)).

T<sub>a</sub> – The A layer is the lowermost part of the turbidite and comprises massive to normally graded, structure less, fine- to coarse grained sand. Due to a rapid deposition from the body of the flow, the base of this layer is often eroded into the bed below.

T<sub>b</sub> – This part of the Bouma Sequence involved planar-laminated sand, which often tends to be finer and more sorted than the division below. The lamination found in the B sequence represents an initial waning flow, possibly due to pulses of erosion separated by deposition in an overall upper-flow regime.

T<sub>c</sub> – This layer consists of ripple-laminated medium- to very fine sand. This indicates rapid deposition from a waning flow having a more moderate flow velocity (lower flow regime: tail part).

T<sub>d</sub> – This sequence involves parallel laminated silt and interlaminated silts and mud, which is thought to be deposited by the final stage of a waning flow, possibly including pulses of erosion separated by deposition. The lamination in this part is often less defined than in the B sequence.

$T_e$  – The uppermost sequence of the deposit contains homogenous, structure less hemipelagic silt and clays. This part of the Bouma sequence is thought to be the final deposits from suspension fall out as the flow diminishes.

The total sequence is rarely found, and hence often only parts of the sequence is found in core material. Bouma (1962) hence named turbidites that don't have top and/or bottom sequences.

A) Base-cuttet sequences: missing either one ( $T_a$ ), Two ( $T_a-T_b$ ), three ( $T_a-T_c$ ) or four ( $T_a-T_d$ ) intervals of a complete Bouma-sequence.

B) Truncated sequences: missing either one ( $T_e$ ), two ( $T_d-T_e$ ), three  $T_c-T_e$ ) or four ( $T_b-T_e$ ) intervals of a complete Bouma sequence.

C) Truncated, base-cuttet sequences: missing both bottom and top interval(s). This means that only  $T_b$ ,  $T_b-T_c$ ,  $T_c-T_d$  and  $T_d$  can exist.

#### 2.6.4.5 Ice rafted debris

Ice-rafted debris (IRD) are lithified grains/clasts (>2mm) or sediment pellets/aggregates transported by icebergs and/or sea ice and deposited into an aqueous environment. In this process the ice acts as a raft, providing buoyancy to any debris carried within or on the surface of the ice float. The process is initiated by calving of icebergs containing sediments and are transported out into the ocean. The deposition of the sediment has three main processes (figure 2.6.4.5a): 1) Overturning of iceberg, dumping the sediment into the water columns, 2) Outwash and 3) Dropping of material as the iceberg melts (Vorren et al., 1983; Dowdeswell & Dowdeswell, 1989). Grounded icebergs (deep-keeled icebergs) may lead to re-suspension and re-deposition, as it ploughs and/or bring material up in suspension again from the seabed (Vorren et al., 1983).

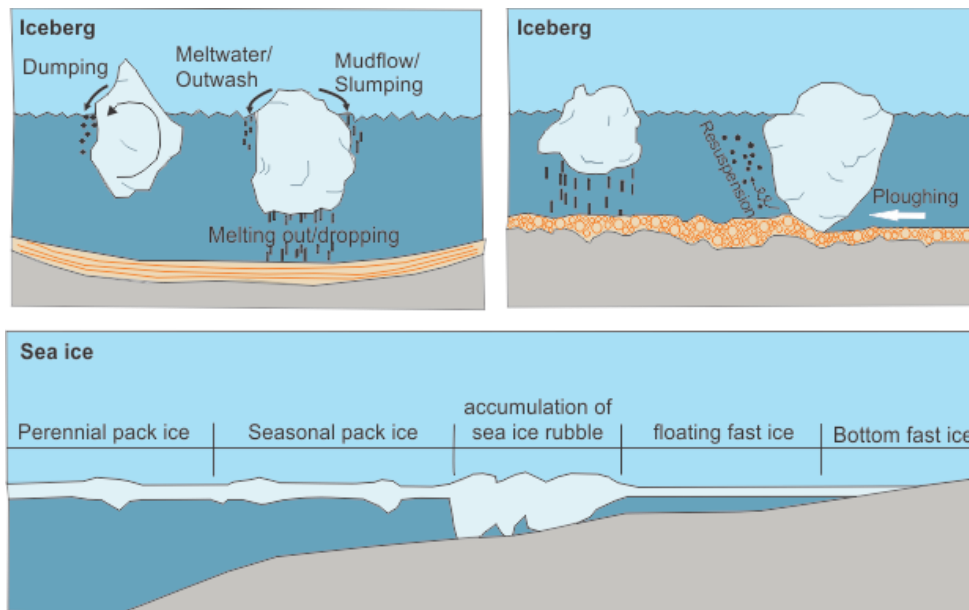


Figure 2.6.4.5a: Types of deposition from iceberg and sea ice rafting (modified from Vorren et al., 1983)

The rate of calving by glaciers are controlled by the sea-ice conditions when glaciers terminates. In the winter season sea-ice may form in the front of the glacier, leaving the calved icebergs trapped, and releases them when the sea-ice breaks up and are released into the ocean (Dowdeswell & Dowdeswell, 1989). Sea-ice incorporates sediment by 1) sea-ice freezing onto land (shorefast ice), 2) when suspended material freezes into the sea-ice, or 3) with formation of anchor ice (Polyak et al., 2010).

#### 2.6.4.6 Sediment pellets

Sediment pellets are aggregates of sediment with a diameter between 1 to 5 cm (Henrich et al., 1989; Goldschmidt et al., 1992). These aggregates are previously found and described by coring the Arctic and Norwegian-Greenland Sea seafloor. The name “sediment pellets” were given by Clark et al., (1980) and Goldstein (1983) to better describe this facies.

The sediment within the pellets are usually fine-grained with more than 90% of the material below 63  $\mu\text{m}$  (Pfirman et al., 1989; Berner & Wefer, 1990; Pfirman et al., 1990).

The origin of these pellets are not clearly understood and several origins are suggested. Clark et al. (1980) and Minicucci & Clark (1983) suggested a glacial origin, while Goldstein (1983) prefers a sea ice origin for the silt rich sediment pellets. Observed frozen sediment pellets as IRD in Alaska (Minicucci & Clark, 1983) and accumulation of sediment and aggregates between the ice crystals in glaciers and sea ice (Polarstern Shipboard Scientific Party, 1988).

#### 2.6.4.6.1 Sediment incorporation in ice

The entrapment of sediment into the sea ice happens along the shelves in the ocean basin margins, while the sediments incorporated to icebergs are derived from further inland locations and on the shelf during more extensive glacial periods.

To be able to reach the deep sea the sediments must remain within the ice, and later be contained during the transport and deposition. By examination, possible incorporation processes of sediment and the general characteristics makes it possible to establish a likelihood of sediments deposited from either sea ice or icebergs (Goldschmidt et al., 1992).

#### Glacier

1) When a glacier moves over a bed, it incorporates sediments into the ice subglacially. Sediments of any size gets incorporated as freeze and thaw action are entrained and released at the bottom of the glacier (Hodel et al., 1988). The mineralogy of the sediment is a reflection of the bedrock or basal till the ice flows over. Due to the constant grinding of ice and the flow of basal meltwater the grains are strongly rounded (Boulton, 1978; Dowdeswell et al., 1985; Dowdeswell, 1989; Dowdeswell & Dowdeswell, 1989). 2) Supraglacial sediment falls down onto the ice from nunataks and glaciated valley walls. The shape of the grains are hence angular. The minerology reflects the bedrock outcrop. Since this part of the glacier is less active, the grains remains angular and are deposited further out (Boulton, 1978; Dowdeswell et al., 1985; Dowdeswell & Dowdeswell, 1989). 3) There may also be entrapment of sediments from the seafloor into an iceberg if the keel drags along the shallow marine bottom (figure 2.6.4.6a). This incorporation method is not considered important deep marine deposition (Goldstein, 1983; Goldschmidt et al., 1992; Henrich et al., 1995).

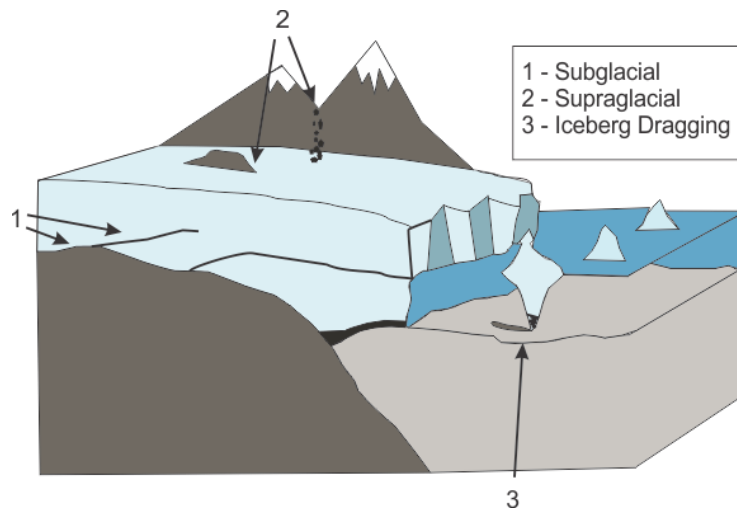


Figure 2.6.4.6a: Schematic, scale less illustration of the process involved in the incorporation of sediment into glaciers/icebergs (modified from Goldschmidt et al., 1992).

### Sea Ice

1) Aeolian action can deposit sediments onto the ice surface, where strong winds can blow sand and coarser material to the ice (Stefansson, 1921). The finer material is blown for longer distances. Wind may also lead to redistribution of material of the Arctic ice pack (Pfirman et al., 1989). 2) Storm waves and strong tidal currents may generate turbulence during ice formation and hence re-suspend sediments from the shallow marine area, leading to incorporation of sediments into the newly forms `slush ice` (Barnes et al., 1982; Reimnitz et al., 1987). Resuspension may also occur after the ice cover was formed (Gilbert, 1990). This process predominately incorporates finer material into the ice. 3) Keels of ice floe can drag along the bottom, picking up both fine and coarser sediments from the seafloor. 4) In water shallower than 0.3 m sea ice may incorporate sea floor sediments by coming in contact or freezing to the bottom. The larger the tidal range the larger the more sediments may be retained, and floated up during flood tide (Knight & Dalrymple, 1976). 5) Rockfalls deliver larger clasts of sediment onto the ice primary during spring. Rockfall is most accelerate during ice melting in the mountain. Due to the melting of sea ice in the same time as the ice in the mountain it is unlikely that sediments deposited by rock fall onto the ice are transported significant distances. Another possible trigger for rock fall are seismic activity. 6) Rivers have the ability to carry sediments onto or under the ice surface during spring (figure 2.6.4.6b). The River ice can also get sediment incorporated if it freezes to the riverbed. This type of sediments will be well sorted. The huge amount of sediment during spring and the melting of ice, exclude longer travel distances of river ice.

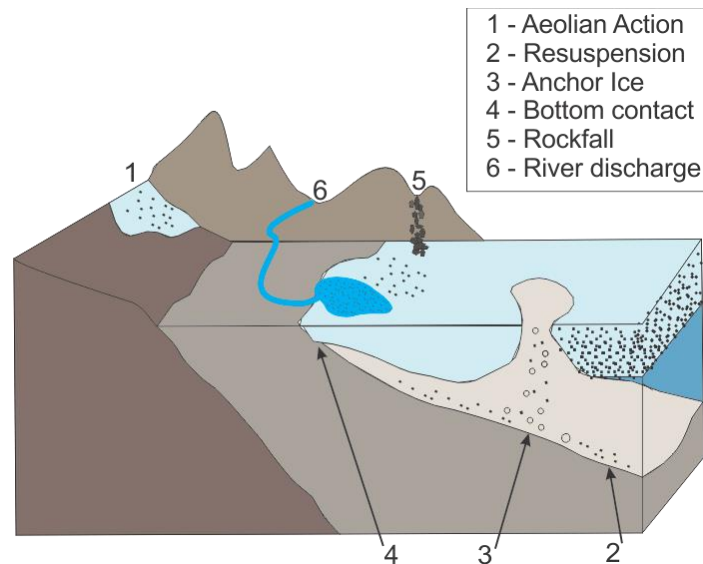


Figure 2.6.4.6b: Schematic illustration of the process involved in the incorporation of sediment into sea ice (Modified from Goldschmidt et al., 1992).

Sediment-laden sea ice has a high possibility of being transported further out into the ocean, and predominately carries fine-grained sediments. If the pellets are rafted by sea ice, they may form when sediment-laden sea ice were subjected to surface melting, leading to concentration of sediments on the ice surface, and meltwater may sort the sediments into regions with higher concentrations of sediments (figure 2.6.4.6c).

Due to a darker color the albedo of the sediments are decreased leading to absorption of solar radiation and an increased heat, leaving the surrounding ice to melt forming a cryoconite hole (Goldschmidt et al., 1992). Several freeze and thaw cycles then forms the aggregates into pellets (figure 2.6.4.6c). By continues melting the ice-raft may turn unstable and tilt the ice floe, dumping the newly formed pellets into the ocean and geological record.

The pellets derived from icebergs will form in the same way, but will have a wider variety of clast shape and size due to calving from a different area than deposition and will hence lead to a wide variability of mineralogy of the pellets. The icebergs drifts with the wind and hence takes longer to melt than the sea ice. The impact of the wind and ocean currents also make pellets formed by sea ice spread out into a larger geographic area (Goldschmidt et al., 1992; Henrich et al., 1995).

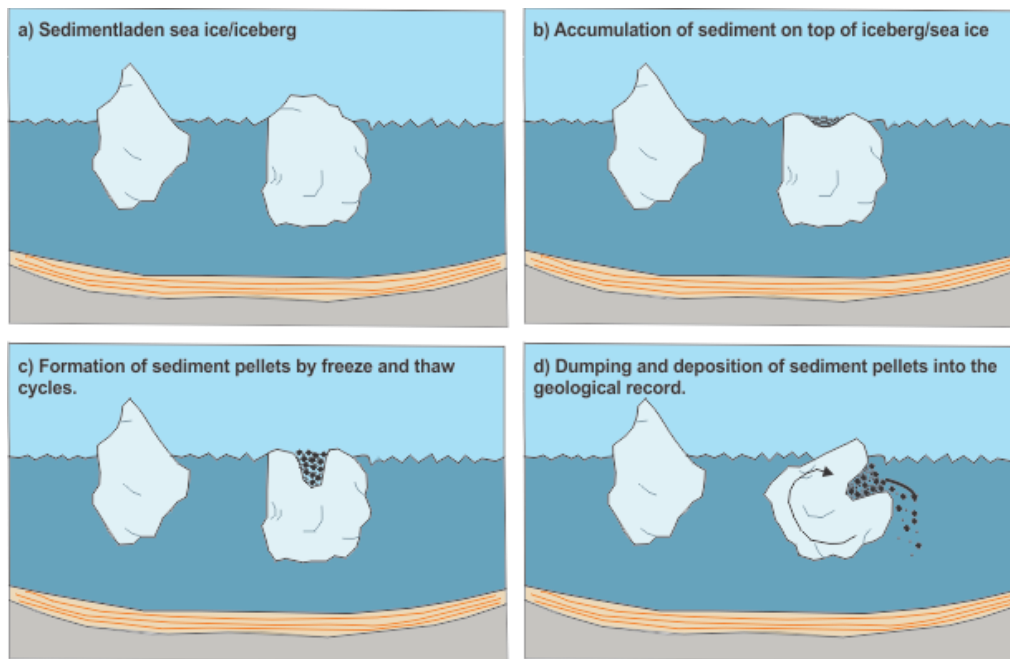


Figure 2.6.4.6c: Principal sketch explaining the formation of sediment pellets within an iceberg/ sea ice.

### 2.6.5 Processes during a glacial regime

During full glacial periods large amounts of sediments are deposited on the outer shelf and upper slope of the western Barents Sea. Due to this the Barents Sea continental margin prograded in a westward direction (Vorren et al., 1989), which was repeatedly truncated, indicating erosion from grounded ice and re-deposition further westward. Indicating that the ice must have reached the shelf in several re-advances. Due to failure of the large sediment accumulations, a number of mass wasting events are inferred to have occurred, resulting in the generation of glacial debris flows, which is assumed to have formed the glacial debris lobes on the Bear Island TMF (figure 2.6.5). During glacial periods there was a larger income of basal meltwater plumes and calving icebergs, depositing IRD on the continental slope and the deep-sea basin (Vorren et al., 1989; Laberg & Vorren, 1995).

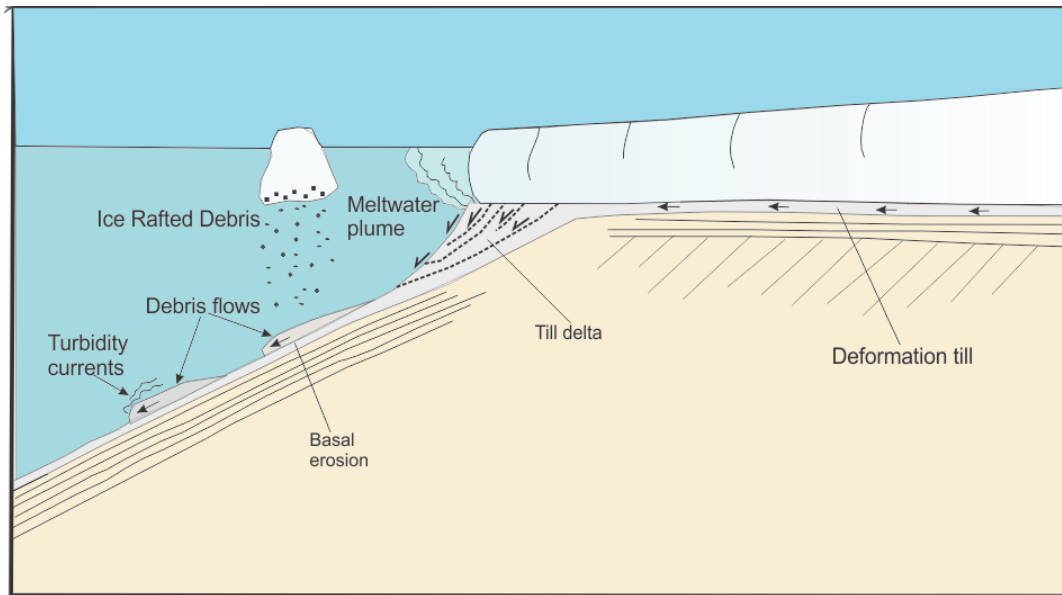


Figure 2.6.5: Schematic model showing the main sedimentary processes on the shelf break and upper slope during the presence of the ice sheet at the shelf break (modified from (Laberg & Vorren, 1995).

### 2.6.6 Processes during interglacials

In interglacial periods the main contribute of material has a hemipelagic origin. This material is derived by proximal continental areas, and in mostly transported into the sea by aeolian activity and ocean currents (Nichols, 2009). There is only a very small proportion of material deposited to the continental margin and deep sea. This is due to the over-deepened ice-free fjords that acted and acts as sediment traps for the land derived erosional products.

On the continental shelf and upper slope, sediments are redistributed by ocean currents. The relative warm Atlantic Water of the Norwegian Current flows north over the outer shelf and upper slope causing winnowing of sea floor sediments down to a water depth of 700-800 meter. This process forms sand and gravel lag deposits on the shelf (Vorren et al., 1983).

During winter the formation of cold, dense water on the shelf may cause downslope gully-forming currents eroding into the slope succession (Vorren et al., 1998).

### 3. Material and methods

In the following subchapters the material and methods used to retrieve information from the core are described in further detail.

### 3.1 Swath Bathymetry

The swath bathymetry data used in this study was collected using the Kongsberg Maritime Smirad EM 300 system of RV *Helmer Hanssen*. A hull-mounted system with an operational frequency ~30 kHz. The swath bathymetry sonar system is a high-resolution imaging system emitting a “fan” of sound beams onto the seafloor providing a detailed scan of the seabed, where the beams are pointing sideways to the acquisition direction in a specific angle to the vertical (Denbigh, 1989). By applying this method, it gathers information about morphology, submarine structures, slopes, water depth and the type and distribution of sediments. The width of the area able to be scanned is dependent on the water depth, as the resolution decreases at greater depths.

The bathymetry data of the present study shows areas with different artefacts and artificial “holes” and “bumps”. Also, in some areas the dataset are missing. This is due to rough water conditions during the data acquisition. Acoustic interference is the main sources of error while collecting the data (Denbigh, 1989).

### 3.2 Laboratory work – Sediment cores

The laboratory work was carried out at the Department of Geology at the University of Tromsø, The Arctic University of Norway, from August 2015 to Mars 2016.

The studied core, MD992301 (table 3.2a) has a length of 11.56 meters and are divided into 8 sections numbered I to VIII (table 3.2b). The calypso core was taken by a giant piston corer in 1999 during the Leg 3/4 of the IMAGES V cruise by RV *Marion Dufresne*, and has since been preserved at 4°C at the core repository of the Department. The core sections were examined and analyzed in the laboratory using X-ray images, pictures of the split core surface, XRF logging results, magnetic susceptibility measurements, water content, grain size analysis and picking of foraminifera for dating. This to determinate the lithology, sedimentary structures, physical properties and geochemical composition of the cored sediments. In the following subchapters a more detailed description of methods used in the laboratory will be presented.

Sampling station	Date	Time GMT	Location	Latitude (N) Longitude (E)	Water Depth (m)	Penetration (m)	Recovery (m)
Site 42	19.08.99	23.59	Bear Island Trough Mouth Fan	74°45.13 N 010°00.82 E	2518 m	11 m	11.56 m

Table 3.2a: Informal table about MD 992301.

Core section (MD992301)	Depth interval
<b>I</b>	0-145 cm
<b>II</b>	145-295 cm
<b>III</b>	295-445 cm
<b>IV</b>	445-595 cm
<b>V</b>	595-745 cm
<b>VI</b>	745-895 cm
<b>VII</b>	895-1045 cm
<b>VIII</b>	1045-1156 cm

Table 3.2b: The subdivisions of MD992301 and their respective depth intervals.

### 3.2.1. X-ray photography

X-ray photography is a non-destructive method of imaging sediment core samples with the use of electromagnetic radiation. The X-rays are generated when a high voltage direct current is applied to a cathode causing electrons to flow through a vacuum tube and collide with an anode (Fujifilm, 2014). When the incoming electron from the cathode collides with an inner-shell electron in the anode, an X-ray is emitted as a result of an electron from the outer shell goes into the vacant inner shell and emitting the excess energy (Schad, 2008)

The quality of the radiographs are controlled by several factors such as contrast, sharpness and density of the material. The magnification and distortion in the photographs depends on geometrical the arrangements relative to the X-ray tube and/or the detector, difference in the thickness through the core sections, or the angle of the X-ray beam relative to the core and detector (Fujifilm, 2014).

The X-ray images of MD992301 were taken of half core sections using the GEOTEK MSCL-XCT X-ray core imaging system (figure 3.2.1) at the University of Tromsø. The values used during imaging to get optimal exposure were 120 kV and 225  $\mu$ A, and an image was taken every 20 mm. Analogue X-rays taken in 1999 have also been available for the present study.

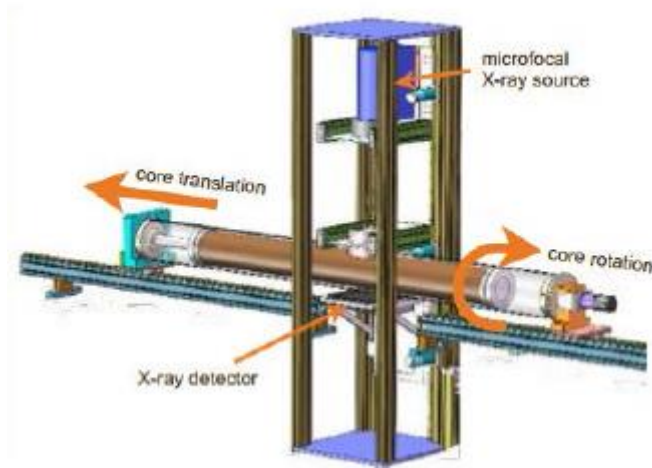


Figure 3.2.1: 3D model of the GEOTEK MSCL-XCT X-ray core imaging system (GEOTEK, 2014b)

### 3.2.2 XRF-scan

X-ray fluorescence (XRF) core scanning is another non-destructive method used for analyzing geochemical elements on core surfaces (Marum, 2013b). The Avaatch XRF core scanner uses X-rays from a radioactive source of Radium (Ra), to excite and detect the geochemical components ranging from Mg to U in the periodic table. The values measured is given in counts per second (cps).

When X-rays collides with a material, secondary fluorescent X-rays are generated and measured for analysis of the geochemical composition of solids, liquid and powder (Beckhoff et al., 2006; Forwick, 2013a ). To be able to detect lighter elements, a He-atmosphere is used. This atmosphere is applied to reduce the friction of the secondary radiation caused by the presence of oxygen. By using element ratios misinterpretations are avoided (Forwick, 2013a).

The parameters of the instrument can be adjusted and processed in order to provide the best suited settings for selected elements. The measurements of the various elements were done in several runs, changing the current (I), tube voltage (U) and filters applied. To measure light elements such as Mg to Co 10 kV were applied, for the interval of Ni to Mo 20 kV were used, up to heavy U 50 kV is used (Forwick 2013a).

Prior to the measurements, the core was cleaned and adjusted too room temperature, and the core tube had to be adjusted so the apparatus were able to hit the sediments. The preparation was done to be sure of reliable results, demanding a homogenous dry and flat surfaced core. To avoid contamination of the sediment and apparatus, a 4µm ultralean film was applied. Excess oxygen trapped between the film and the sediments was removed using a roller.

To do the measurements a prism is lowered onto the sediment surface, where the incoming radiation generated hits the surface at ~45 degrees. The detector for outgoing radiation is hence also installed in a 45° angle (Richter et al., 2006). During measurements the system is flushed with helium to prevent partial or complete absorption of radiation by the surrounding air (figure 3.2.2). The voltage values used for measuring the geochemical elements in the core were 10 kV and 30kV with measurement interval of 10 mm.

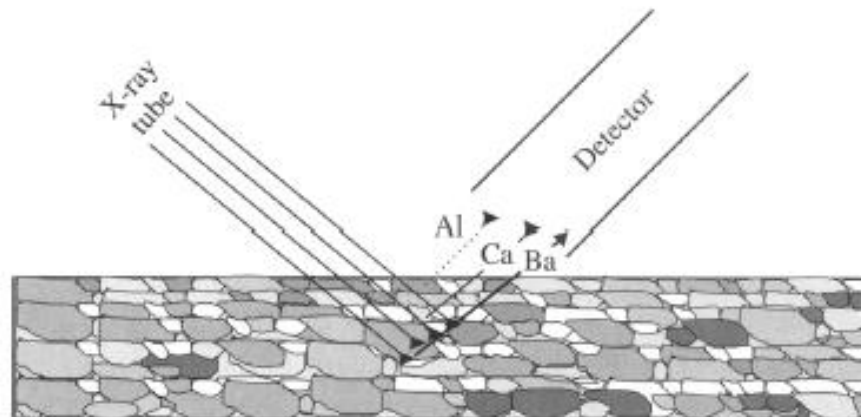


Figure 3.2.2: Principal sketch showing the principle of XRF logging on split cores (Richter et al., 2006)

Comparison of XRF measurements done on wet sediments relative to dry sediment samples show that the intensity is largely reduced in light elements like Al and Si, whereas heavier elements remains relatively unaffected (Tjallingii et al., 2007; Weltje & Tjallingii, 2008; Hennekam & de Lange, 2012). Due to this the ideal measurements should be taken at homogenous material with a dry and flat surface. By calculating ratios of each element instead of single element intensities, more reliable results are gathered (e.g. Fe/Ca or the sum of several elements e.g. Ti/sum) (Weltje & Tjallingii, 2008). This method can minimize the artifacts produced by physical factors. The “sum” refers to all element counted exceeding 10 000 cps during the 10 kV run, and 3000 during the 30 kV run..

The geochemical composition of sediments and sedimentary rocks are strongly influenced by several factors, including: source area composition, climate, mode of sediment transport and depositional environment. It hence provides a wide range of information about sedimentary source, mode and direction of sedimentary transport, paleoclimate, ocean circulation, organic production, seafloor and sediment oxygenation and post-depositional changes. It also provides valuable information about physical and biological processes present under the deposition and post-depositional chemical reactions. This provides a complex composition of the sediment

that gives valuable paleoceanographic and paleoclimate information (Calvert & Pedersen, 2007).

Examples of such correlations are many, for instance Zirconium (Zr) and Titanium (Ti), which are heavy minerals and hence often correlates to the base of turbidites. Clay minerals are often enriched with Potassium (K) and may correspond to turbidite muds. Indicators of terrigenous supply are e.g. Aluminum (Al), Iron (Fe), Titanium (Ti) and Zirconium (Zr) while Silicon (Si) both is indicator of terrigenous material and productivity (Croudace et al., 2006; Bertrand et al., 2012). Higher levels of Calcium (Ca) indicates increased amount of carbonate within the sediment, and combined with Iron (Ca/Fe) it may indicate biogenic carbonate:detrail clay ratios that indicates an increased amount of foraminifera in the sample (Rothwell et al., 2006).

### 3.2.3 Multi Sensor Core Logging (MSCL)

To measure the physical parameters of the core, the GEOTEK Multi Sensor Core Logger (MSCL) was used (figure 3.2.3). This apparatus provides continuous centimeter-scale measurements of marine sediments. Due to a split core, the only parameters able to be measured at the Department lab were magnetic susceptibility and temperature. Temperature may have an influence on the physical parameter of magnetic susceptibility (Marum, 2013a). Due to this the sections were stored in the laboratory overnight prior to the measuring to avoid unwanted influence. The room temperature was measured by a thermometer placed on the apparatus, and all of the sections was hence assumed to have the same temperature, the temperature of the room which was about 20.1°C.

Continuous records of physical parameters provide the basis for stratigraphy and correlation between several logs. The multisensory core logger used at the department lab provides continuously and simultaneously measurements of several physical parameters (magnetic susceptibility, gamma density, natural gamma radiation, p-wave velocity and electrical resistivity).

All of the different physical parameters of the apparatus were calibrated before use.

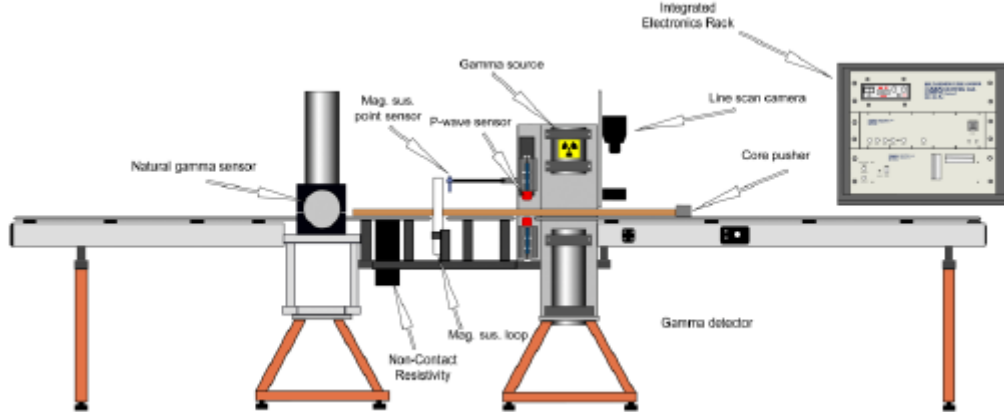


Figure 3.2.3: Principle sketch showing the Multi-Sensor Core logger setup (GEOTEK, 2000). The MSCL used at UiT has all instruments measuring horizontally (vertical placement is shown in the sketch).

### 3.2.4 Magnetic susceptibility

Magnetic susceptibility is defined as “the degree of a magnetization of a material in an applied magnetic field” (GEOTEK, 2014a). The presence of either paramagnetic, ferromagnetic, ferrimagnetic or antiferromagnetic material will create a positive response which will strengthen the magnetic field. Where ferrimagnetic minerals like magnetite e.g. will create values 3 or 4 times greater than antiferromagnetic minerals like e.g. hematite, If the ferromagnetic concentration is low, paramagnetic (e.g. clay and ferromagnesian silicate minerals) and diamagnetic minerals (e.g. biogenic carbonate and silica) will contribute to the measurement record, with a negative response being indicative of a diamagnetic material in the sample (Stoner et al., 1996). The measurement of this physical parameter is used for correlating changes in the sedimentary environment, as well as inner-core correlation (GEOTEK, 2014a).

### 3.2.5 Water content

The water content is measured relative to dry weight, by measuring the weight of each sample before and after drying in a heating cabinet. The samples were left in the cabinet for 3 days before re-measures to be able to remove as much water as possible.

### 3.2.6 Radiocarbon dating

Radiocarbon dating is a method based on measuring the decay of  $^{14}\text{C}$ . Due to a limited maximum age, this method only provides reliable dating for material younger than 50,000 years.  $^{14}\text{C}$  is formed in the upper atmosphere by a collision between cosmic rays and  $^{14}\text{N}$  atoms, and is hence natural occurring. After oxidation,  $\text{CO}_2$  is created and mixed into the

atmosphere and world's oceans. The CO<sub>2</sub> enters plant material through photosynthesis and becomes a part of calcareous (CaCO<sub>3</sub>) marine organisms by entering the carbon cycle. When an organism dies, the content of the <sup>14</sup>C is no longer in equilibrium with the atmosphere and biosphere. The unstable <sup>14</sup>C will then start to decay, with a half-life of 5730±40 years. When measuring the number of unstable <sup>14</sup>C relative to the stable and non-radioactive <sup>12</sup>C and <sup>13</sup>C information about when the organism died may be calculated (Bowman, 1990; Bowman & Balaam, 1990).

#### 3.2.6.1 Accelerator Mass Spectroscopy (AMS)

The samples were picked (table 3.2.6.1), and sent to the laboratory of Ion Beam Physics, ETH Zurich for preparation and measuring using the Accelerator Mass Spectroscopy (AMS) method. This method is performed by accelerating C-ions from the picked samples containing foraminifera and subjecting them to a magnetic field. Particles with the same velocity, but different mass, will deflect differently towards the applied magnetic field. The heaviest particles will deflect least, and hence makes it possible to identify and measure the amount of <sup>14</sup>C present in each sample (Bowman, 1990; Higham et al., 2015). The Laboratory of Ion Physics uses a new method which is capable to retrieve dating from samples containing less than 100 µg carbonate (0.001 g). The method measures the radiocarbon content of carbonates by measuring the CO<sub>2</sub> produced by acid decomposition applying a gas ion source AMS (Wacker et al., 2013).

Depth	Species	Weight (gram)
33 – 34 cm	Neogloboquadrina pachyderma (sinitral)	0,0019
149 – 150 cm	N. pachyderma (sinitral)	0,0024
199 – 150 cm	N. pachyderma (sinitral)	0,0015
272 – 273 cm	N. pachyderma (sinitral)	0,0014
692 – 693 cm	N. pachyderma (sinitral)	0,0001 (failed, too small sample)
779 – 780 cm	N. pachyderma (sinitral)	0,0010
898-899 cm	N. pachyderma (sinitral)	0,0001 (failed, too small sample)
984 – 985 cm	N. pachyderma (sinitral)	None (failed, no forams)

Table 3.2.6.1 Picked intervals and weight of the foraminiferal samples.

### 3.2.6.2 Calibration and marine reservoir effects

Earth's magnetic field, sunspot activity and the Suess effect causes changes in the production rate of  $^{14}\text{C}$  in the atmosphere. Hence, the concentration of  $^{14}\text{C}$  in the atmosphere and in living organisms varies, resulting in a discrepancy between the radiocarbon age and calendar age (Bowman, 1990). Together with the AMS, the radiocarbon dates are calibrated to calendar years before present (cal. yr. BP).

The  $^{14}\text{C}$  produced in the atmosphere is constantly mixed into the sea surface by an exchange at the ocean-atmosphere interface, and is hence believed to be in equilibrium. However, as water sinks towards the deep sea, and the supply of radioactive  $^{14}\text{C}$  from the atmosphere stops and the decay of the unstable  $^{14}\text{C}$  starts. The radioactive decay will provide a lower activity, and hence an increased apparent age, the “marine reservoir effect” (Mangerud, 1972). In the region the core is retrieved from the marine reservoir age is 440 years (Mangerud & Gulliksen, 1975; Hald et al., 2001). When dating calcareous marine organisms the aging effect of the region has to be accounted and calculated to avoid large regional variations, to do this the CALIB 7.1 software (Stuvier et al., 2016) was used to calibrate the radiocarbon ages from the AMS dating. The program used, MARINE13 calibration curve (Reimer et al., 2013) with a global reservoir correlation of 405 years. To accommodate for the difference between

the curve and the marine reservoir age in the western Barents Sea an additional regional difference ( $\Delta R$ ) were added, which in this study was found to be  $67 \pm 34$  (Mangerud & Gulliksen, 1975)

### 3.2.6.3 Radiocarbon dating and estimation of an age model

The obtained radiocarbon dates were used for estimating an age model for MD992301. By using a linear interpolation and assuming an estimated constant accumulation rate of the sediments between the dated intervals, the boundaries between the units were estimated. However, due to a sparse amount of dates available, uncertainties are to be expected.

## 3.3 Sedimentological description and logging

After analyzing the core sections using the different apparatus as described above, a detailed and systematic description of the lithology was made. After cleaning the surface, the sediments were described including grain size, sedimentary structures, boundaries, color, clast distribution (IRD), bioturbation, appearance of micro- and macrofossils and other general remarks. Color was found using the Munsell Soil Color Chart.

A lithological log was made, summarizing these observations, where a total of 14 units and 6 facies were identified and described (table 4.3a).

## 3.4 Grain size analysis

### 3.4.1 Sampling and preparation

Following the sedimentological description a total of 124 samples was taken and prepared for grain-size analysis. The sediment was sampled in order to have more detailed measurements of the various lithological facies identified. After sub-sampling the core, the sample was stored in cups and placed in the heat cabinet for several days for drying. By doing this it was possible to measure the sediments water content. After this the dried samples were watered by distilled water before they were treated with acetic acid ( $\text{CO}_3\text{COOH}$ ) over night to remove any carbonate in the sample. When the reaction was complete the samples were washed with distilled water twice. Later the samples were treated with hydrogen peroxide ( $\text{H}_2\text{O}_2$ ) to remove any organic material present. The samples were again flushed twice after complete reaction. The final step before the grain size analysis was to add a few drops of calgon (sodium polyphosphate) in each sample, and place them in an ultrasonic bath. This to prevent any flocculation and the formation of aggregates within the sediment. Prior to measuring, the

samples were shaken before they immediately were placed in the apparatus. This according to the standard procedures for the Department lab.

#### 3.4.1.1 Sampling and preparation of the sediment pellets

The samples of the sediment pellets were retrieved from two depths entraining several pellets large enough for sampling. The pellets were put in plastic containers and submerged in distilled water to see if the pellets would dissolve. After this the samples were shaken, to be sure of a complete dissolution.

The sediments entrapped in the pellets were then sieved thorough a filter paper and dried in a heating cabinet. When the solution of the sediment pellets were done, the samples were treated with acid and measured in the apparatus on the Department lab.

#### 3.4.2 Measurements and statistics

The grain-size analysis was conducted using the LS 13 320 Laser Diffraction Particle Size Analyzer. This apparatus only measures particles from 0.04  $\mu\text{m}$  up to 2000  $\mu\text{m}$ . Particles exceeding this size were therefore excluded in the results, and presented as clasts or sand in the lithological log based on appearance. If the samples were too massive, they were diluted before measuring. Classification of grain-sizes and associated terminology used in this study are based on the Udden-Wentworth grain-size for clastic sediments (Udden, 1914; Wentworth, 1922; Nichols, 2009) (Figure 3.4.2a). To determinate the approximate relationship between the different size fractions, Folk's (1954) classification system for sand, silt and clay were used (figure 3.4.2b).

mm	phi	Name	
256	-8	Boulders	
128	-7		
64	-6	Cobbles	
32	-5		Gravel
16	-4		
8	-3	Pebbles	
4	-2		
2	-1	Granules	
1	0	Very coarse sand	
0.5	1	Coarse sand	Sand
0.25	2	Medium sand	
0.125	3	Fine sand	
0.063	4	Very fine sand	
0.031	5	Coarse silt	Mud
0.0156	6	Medium silt	
0.0078	7	Fine silt	
0.0039	8	Very fine silt	
		Clay	

Figure 3.4.2a: An overview of grain-sizes and associated descriptive terminology, based on Udden, (1914) and Wentworth (1922). (Modified from Nichols (2009)).

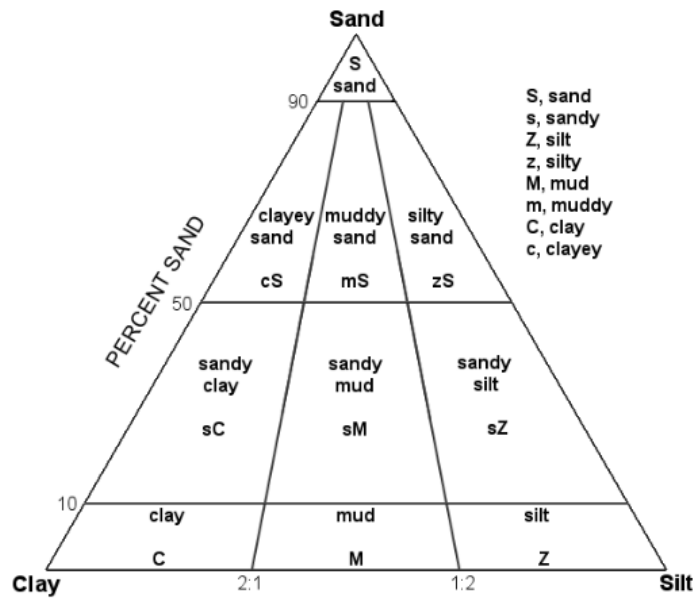


Figure 3.4.2b: Folk's classification system for sediment (Folk, 1954)

## 4. Results

### 4.1 Introduction

Core MD993201 was retrieved from the channel levee of the INBIS channel system between Bear Island Trough Mouth Fan (TMF) and the Storfjorden TMF (figure 4.2.1a). When analyzing the core, the methods presented above were applied as will be further detailed below. From the core description the sedimentary processes involved in the depositional environment will then be discussed.

## 4.2 Swath bathymetry

### 4.2.1 Introduction

A swath bathymetry map was provided in order to identify, describe and interpreted submarine geomorphological landforms in the area around the retrieved core. Where the core will be used for more detailed interpretation of the sedimentary processes and depositional environment present. The bathymetry covers an area of about ~265 km in length and the width of the surveyed area varies from 4 - 28 km. There is a smaller corridor on the northwestern side, around 80 m long and 7 – 10 km wide. The water depth increases gradually from the upper part of the continental slope towards the deep sea where the core is located, from ~<500 - < 2500 meters water depth on the northern Bear Island TMF (figure 4.2.1a, b and c). On part of the northwestern flank of the bathymetry there are noise disturbing the data, making it blurry.

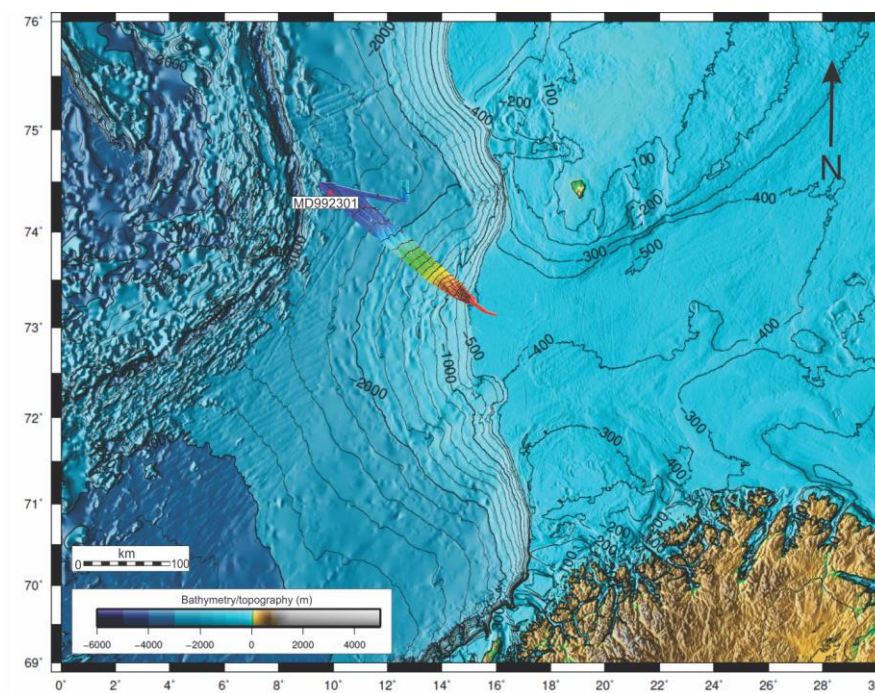


Figure 4.2.1a: Position of the swath bathymetry taken on the northern flank of the Bear Island TMF. The red dot indicates the position of MD992301.

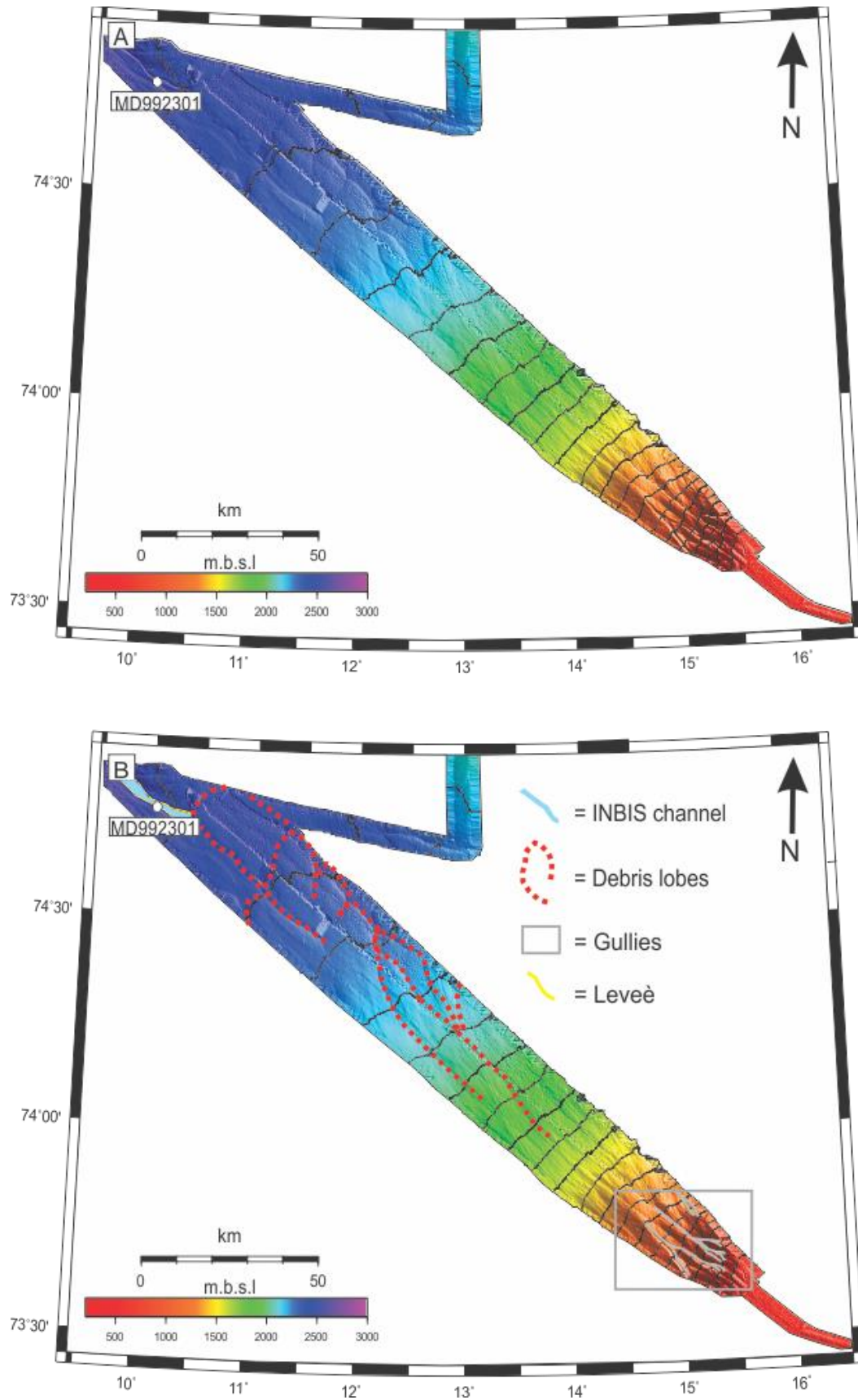


Figure 4.2.1b: A: Swath bathymetry acquired from the northern Bear Island TMF towards the INBIS fan. B: Morphological interpretation. The white dot marks the position of the core.

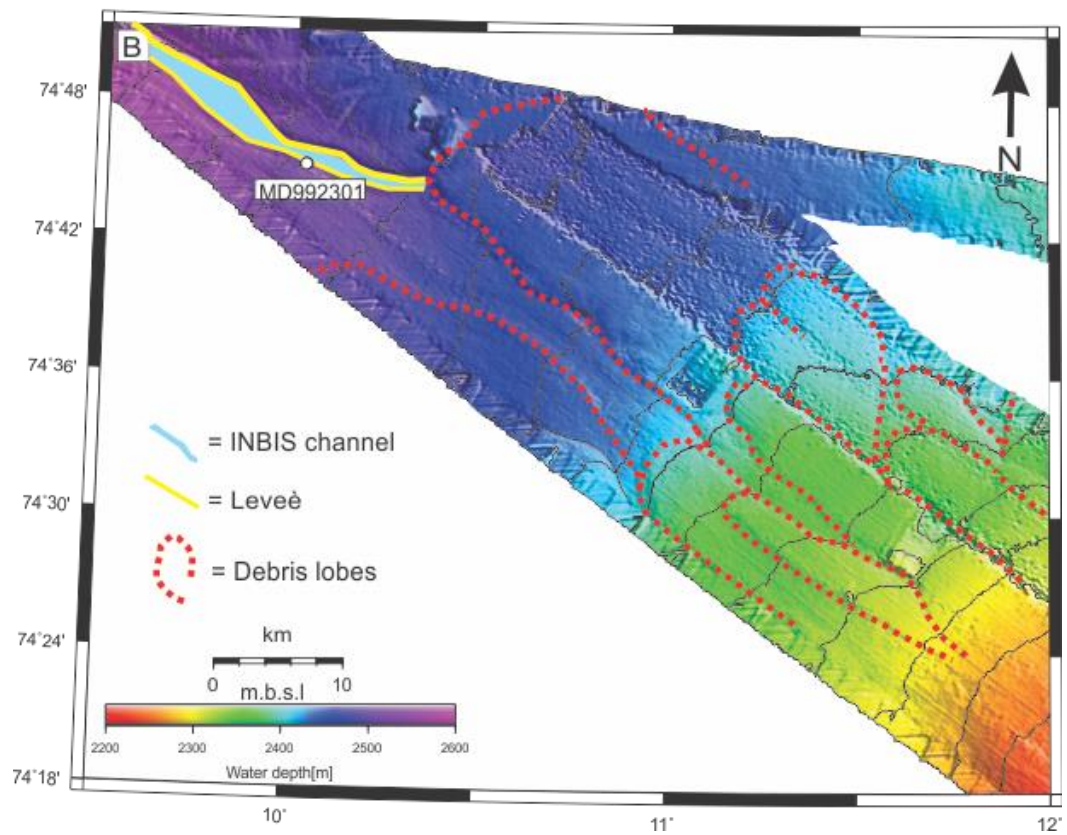
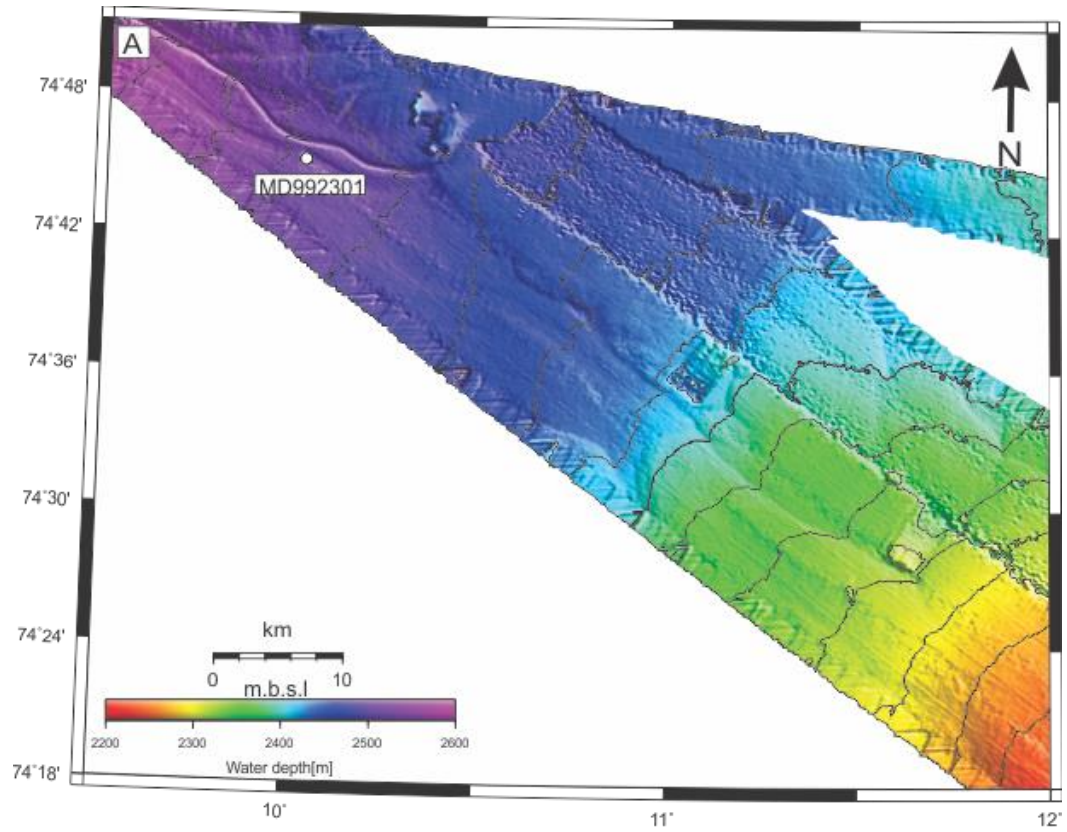


Figure 4.2.1c: A: Bathymetry over the area proximal to the INBIS channel. B: Geomorphological interpretation of the area. The white dot marks the position of the core.

#### 4.2.2 Gullies

In the upper parts of the bathymetry, a network of upper slope gullies are interpreted (figure 4.2.1b). These small submarine channels are interpreted to be up to 150 meters deep and 1 km wide (Vorren et al., 1989). These small channels are formed by four main processes 1) as a consequence of hyperpycnal subglacial meltwater at or near the shelf break (Pedrosa et al., 2011), 2) by erosion from mass-flows initiated from cascading of cold bottom water from the shelf area (Vorren et al., 1989; Piper et al., 1999), 3) by cold bottom currents derived from a nearby ice cap during glaciations (Pedrosa et al., 2011), or 4) formed during interglacials by cold bottom water from the shelf (Vorren et al., 1989).

Pedrosa et al., (2011) has previously identified several gullies on the Storfjorden TMF where they are characterized as smaller channels which are 5-20 km long, at water depths up to 200-1000 meters. Gullies usually have a low sinuosity and are generally <10 meters deep. V-shaped (in cross-section) and show branching on the steepest parts, which is similar of what is seen in the bathymetry. The abrupt change morphology of the gullies seen in figure 5.1 are assumed to be due to the diminished energy of the flows which decreases downslope as a consequence of 1) slope-angle reduction, and hence their ability to erode into the substrate (Pedrosa et al., 2011) and, 2) Density contrast reduction. Similar features are identified by Laberg and Vorren (1995) on the northern flank of the Bear Island TMF, where the interpreted gullies shows levee like features. The presence of levees indicates that the flow were able to erode and transport sediments from the shelf and/or generate density currents on the uppermost parts of the fan, which reached bankfull stage, and spilled on their way downslope (Laberg & Vorren, 1995). Another possible explanation for the levee formation is that density currents may have been initiated in periods of higher sediment supply (Blindheim, 1989). Gullies may evolve into channels, which morphological features disappears downslope, as they gets covered by debris flows deposits (Pedrosa et al., 2011).

The gullies identified east of the cored location is probably formed during the present interglacial, and not related to the origin of the debris flows further west (figure 5.1). The gullies have a restricted infill, this may be due to the transport of cold, dense water downslope on the northern part of the fan (Laberg & Vorren, 1995).

### 4.2.3 Debris lobes

Several large debris flow deposits are previously interpolated east of the cored interval. Laberg and Vorren (1995) have described eight of these large lobes on the Bear Island TMF. In their interpretation they claim that each deposit can be up to 24 km wide and 50 meter thick, and can be followed up to 100 km downslope (figure 4.2.1 b and c).

Large debris flows was initiated when the Barents Sea ice sheet reached the shelf break during fully glaciated conditions. In such settings, as described above, the sedimentation rate is enormous. The high amount of sediment deposited in such a short periodic events makes the sediment unstable and triggers like i.e. earthquakes, oversteepening and excess pore pressure may cause the release of large debris flows. Debris lobes are characterized by a positive bathymetry on the middle fan, and shows a stacked mounded pattern where the subsequent lobes are deposited in bathymetric lows created between older deposits. During LGM, debris flows was on average released every 35-75 years (Laberg & Vorren, 1995).

### 4.2.4 Channels

The INBIS channel adjacent to the core is previously described by Vorren et al., (1998) (figure 4.2.1b and c). The channel is situated at water depths between 2360 - 2520 meters, and the surveyed parts of the channel are ~37 km long and ~2-6 km wide extending from east to west bordered by the Bear Island TMF and Storfjorden TMF (table 4.2.4a). In the bathymetry it is possible to identify a larger debris lobes cutting off the channel in the eastern direction. South of the channel, the channel is bordered by debris flows with origin from the Bear Island TMF (Laberg & Vorren, 1995), and to the north the channel, there is a 10-15 meter natural levee with overbank deposits (Vorren et al., 1998). Current lineation found using side scan sonar, are thought to represent frequently density current activity, leading to overflowing of the channel and deposition in the overbank areas (Vorren et al., 1998).

At the mouth of the channel, which is not scanned in the data set, a fan like accumulation is found called the INBIS fan. The fan is > 50 km wide, with smaller (0.2-1 km wide and 5-10 meters deep) erosive channels flanking the fan (Vorren et al., 1998). The assumed source area for the INBIS channel and overlaying are the Kveithola Trough, the northern Bear Island TMF and southern Storfjorden TMF (Vorren et al., 1998).

<b>INBIS channel</b>	
<b>Position</b>	~74°-75° N and ~10°-15° E
<b>Length (km)</b>	60
<b>Water depth (m)</b>	2360 – 2520
<b>Width (km)</b>	5 – 15
<b>Channel depth (m)</b>	50 – 60
<b>Shape/ orientation/constraining factors/borders</b>	Single channeled: E – W: Boarded by Storfjorden and Bear Island TMF
<b>Sedimentary processes</b>	Turbidity flows
<b>Sediment sources</b>	Turbidity flows and debris flows originating from the Storfjorden and Bear Island TMFs, as well as the interfan area of Kveithola Trough.
<b>Age/period of activity</b>	Mainly during glacials, significantly less during Holocene.
<b>Other features</b>	Upper part buried under debrisflow. 10-15 m- high levee on the northern flank, with mudwaves north of the levee. Thickest sediment package north of the channel > 50 km wide INBIs fan at the mouth.

Table 4.2.4 a: Properties/characteristics of the INBIS channel (Vorren et al., 1998; Forwick. M. et al., 2015).

## 4.3 Core description

### 4.3.1 Lithology

MD992301 is dominated by a sandy silt lithofacies. A total of 5 sandy units are interpreted where all of them shows a normal graded pattern. Between the sandy units thick intervals of mud with random scattered clasts are seen. There are no signs of bioturbation through the core, and only a smaller degree of lamination. The top of the core is disturbed due to friction from the penetrating core cylinder, therefore, some of the layers have a convex shape.

### 4.3.2 Grain-size analysis

From the particle size analysis, the volume of clay, sand and silt were measured and then plotted against core depth (figure 4.4b). There is a dominance of the silty fraction throughout the core (from 12 - 78 %, on average 50.3%), except for the intervals of sandy layers and lenses. In table 4.3.2a the minimum, maximum and average values of the different fractions are presented.

Grain Size	Minimum value	Maximum value	Average value
Clay (%)	0.03	61.5	17
Silt (%)	11.7	78.3	50.3
Sand (%)	0	86.3	32.7

Table 4.3.2a: The minimum, maximum and average values of clay, silt and sand through the entire core. Values are found by using the “maximum”, “minimum” and “average” calculations in excel.

### 4.3.3 Physical properties

The physical properties measured for the core are water content (%) and magnetic susceptibility ( $10^{-8}$  SI(m<sup>3</sup>/kg)). The results of these measurements are represented as plots relative to core depth (figure 4.4b) while the maximum, minimum and average values are listed in table 4.3.3a. From figure 4.4b, it is possible to correlate lower values in both magnetic susceptibility and water content to the sandy layers, while the mud have a relative uniform value throughout the core.

The magnetic susceptibility plot has a higher frequency zigzag- shape around values with only smaller variations for each unit. When there are changes in lithology (e.g. color or grain

size) at lithological boundaries there are a clear increase/decrease in the measured values. The water content is measured relative to the wet weight of the samples extracted from the core, and hence are somewhat uncertain. This relates to the age of the core (1999), thus the core may have lost the moisture over time. Overall the water content shows a decreasing trend down core due to sediment consolidation and compaction. Some errors were evident for the magnetic susceptibility, at the top and bottom of each core section where the values at the top and bottom of the core showed lower values than what the trend was indicating. These values were hence removed from the plot.

Physical properties	Minimum	Maximum	Average
Magnetic susceptibility ( $10^{-8}$ SI(m <sup>3</sup> /kg)).	2.4	77.2	27.8
Water content (%)	2.0	59.1	19.4

Table 4.3.3a: The minimum, maximum and average values of the physical properties measured in core MD992301.

#### 4.3.4 Element geochemistry

The scanned sediments in all eight sections shows a good response for the following elements: Silicon (Si), Sulfur (S) and Manganese (Mn), while Zirconium (Zr), Potassium (K), Calcium (Ca), rubidium (Rb), Strontium (Sr) and Iron (Fe) shows a more moderate response. The element geochemistry is expressed with selected element/element ratios and elements/sum ratios (chapter 3.1.2: XRF scan). This includes elements as Ca/Fe, Sr/Ca, K/Rb and Zr/Rb found in figure 4.4c and Appendix 1: Table 1.

Changes in element/element ratios are described relative to the general lithological trend through the core.

#### 4.3.5 Radiocarbon dating

The results from the AMS radiocarbon dating and calibrated ages are presents in table 4.3.5. The calibrated ages are based on a mean of the  $1\sigma$  range. Due to the limited amount of material available for dating, some of the samples proved too small to be dated. As a result, only a few radiocarbon dates could be obtained from MD992301.

There is a reversed age between 199 - 200 and 272 – 273 cm, where an older age of the uppermost sample were obtained. We interpreted that the reversal to be due to a distal turbidite environment, where the material obtained in 199-200 cm may contain material

deposited by the interlayered sandy units (Forsberg et al., 2007). The sample from 149-150 is therefore not taken into account in the further discussion. In addition, the sample retrieved from 779 - 780 cm proved too old to obtain reliable dating, and is hence excluded in further discussion.

Lab reference	Core	Sampling depth (cm)	Species	<sup>14</sup> C age BP	Delta R	Cal. Yr BP Calib. 7.1 1 $\sigma$ range	Calib. Yr BP Calib. 7.1 2 $\sigma$ range	Cal. yr. BP Calib. 7.1 1 $\sigma$ mean
67559.1.1	MD992301	33-34	N. pachyderma	5365 $\pm$ 75	67 $\pm$ 34	5572 - 5748	5505 - 5867	5668
67560.1.1	MD992301	149-150	N. pachyderma	15990 $\pm$ 360	67 $\pm$ 34	18371 - 19193	17961 - 19604	18788*
67561.1.1	MD992301	199-200	N. pachyderma	17810 $\pm$ 170	67 $\pm$ 34	20670 - 21156	20485 - 21435	20929**
67562.1.1	MD992301	272-273	N. pachyderma	16450 $\pm$ 160	67 $\pm$ 34	19067 - 19485	18884 - 19666	19278
67563.1.1	MD992301	779-780	N. pachyderma	Failed. >50.000	67 $\pm$ 34	-	-	-

Table 4.3.5: <sup>14</sup>C and calibrated ages of the samples retrieved from MD992301. (\*=uncertain due to small amount of foraminifera, \*\*=reversed age)

#### 4.3.6 Visual description

Due to the age of the core the sediment surface was cleaned carefully before any interpretation was done. The subdivision into lithofacies within MD992301 was interpreted based on visual inspection, color images, X-ray photographs and particle size analysis. Based on these parameters the core are subdivided into 14 units. The log of MD992301 is presented in figure 4.4a and is described relative to depth.

#### 4.3.7 Lithofacies

The lithofacies identified are based on Folk`s (1954) classification system for sand, silt and clay (figure 3.3.2b). This triangle divides the sediment into ten group based on the distribution of each grain size (percent of sand, and the ratio between clay and silt). This ten groups are: sand (S), clayey sand (cS), muddy sand (mS), silty sand (zS), sandy clay (sC), sandy mud (sM), sandy silt (sZ), clay (C), mud (M) and silt (Z). In addition codes for diamicton (D)

sediment pellets (Sp), clasts (c), organic debris (o), upward fining (-uf) and lamination (l) were added. The sandy silt fraction is the dominating lithofacies within the core. Coarser sediment (e.g. silty sand) has a darker brown color and the lowermost two units has a dark-grayish color.

#### 4.4 Lithology of core MD992301

Within core MD992301 14 units were identified, described from bottom and up.

The core comprises lithofacies of sZ (sandy silt), Z (silt), M (homogenous mud), zS (silty sand), D (diamicton), Sp (sediment pellets) and sporadic appearance of clay (c) and lamination (l) (figure 4.4a, b and c and table 4.4a).

Facies	Characteristics
<b>Muddy diamicton (D)</b>	<ul style="list-style-type: none"> <li>- Dark muddy matrix.</li> <li>- Dark, angular/subangular clasts.</li> </ul>
<b>Sediment pellets (mud) (Sp)</b>	<ul style="list-style-type: none"> <li>- Dark, sediment clasts of up to pebble size (looks like dark colored cottage cheese).</li> <li>- Laminated with sand lamina/layers</li> </ul>
<b>Massive graded sand (S)(-uf)</b>	<ul style="list-style-type: none"> <li>- Normal graded sand.</li> <li>- Dark olive brown/olive brown color</li> </ul>
<b>Massive hemipelagic mud (M)</b>	<ul style="list-style-type: none"> <li>- Massive mud without any internal structures.</li> </ul>
<b>Massive mud with clasts (M)(c)</b>	<ul style="list-style-type: none"> <li>- Massive muddy matrix with random distributed clasts.</li> </ul>
<b>Massive laminated mud (M)(l)</b>	<ul style="list-style-type: none"> <li>- Massive mud with internal lamination.</li> </ul>

Table 4.4a: Table with the different facies interpreted within MD992301.

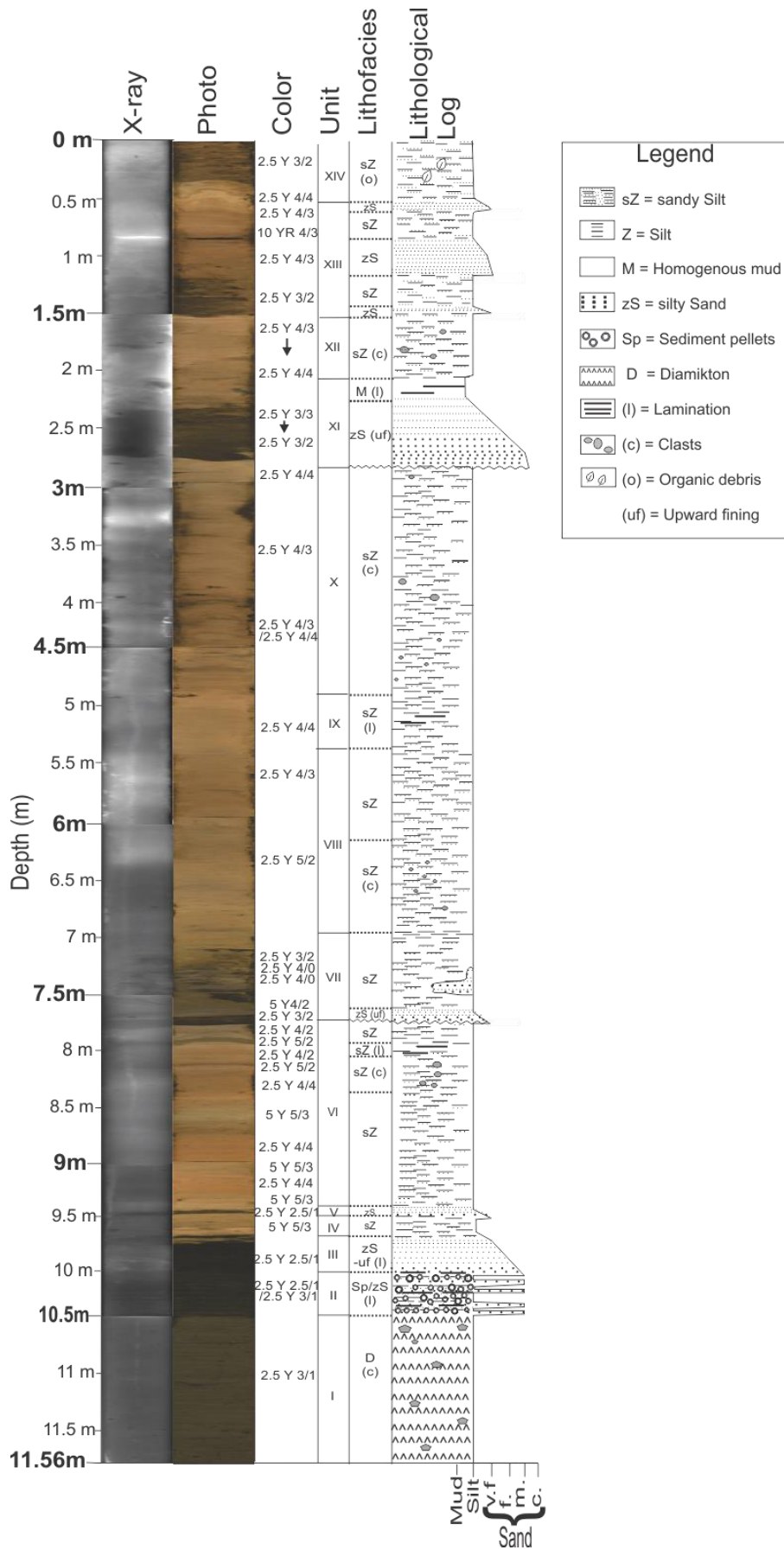


Figure 4.4a: Lithological log for MD992301.

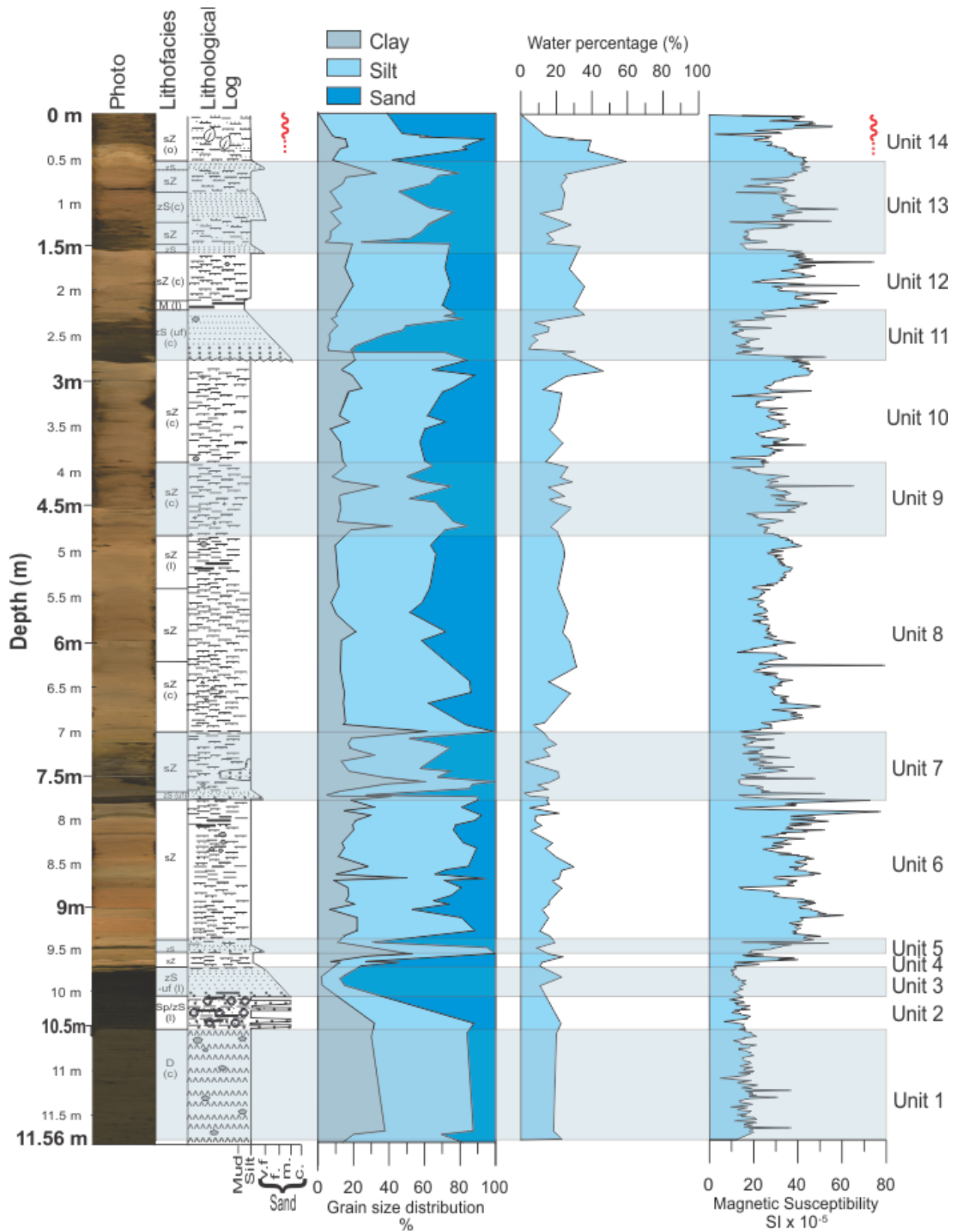


Figure 4.4b: Log showing the grain size distribution, water content and magnetic susceptibility relative to depth with MD992301.

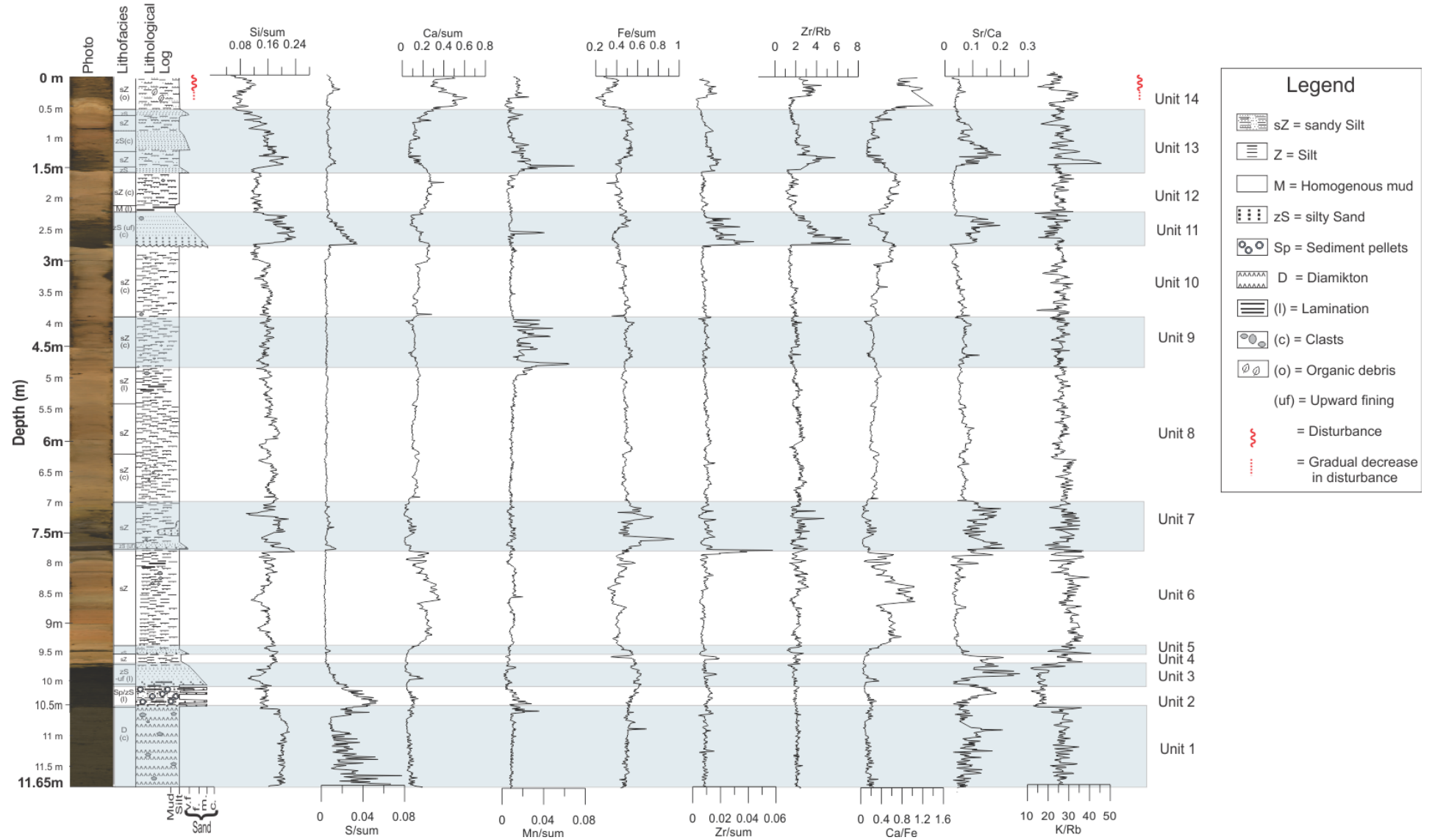


Figure 4.4c: Measured physical properties within MD992301.

#### 4.4.1 Unit 1 (1156- 1031 cm)

##### 4.4.1.1. Lithology and stratigraphy

The lowermost unit within MD992301 contains a compact and massive very dark gray matrix bearing sandy mud and has a high amount of angular clasts. The X-ray images show a larger number of clasts in this unit compared to the others above (figure 4.4a and 4.4.1b). No inner sedimentary structures are seen. The upper boundary is abrupt and the lower boundary is not cores. The grain size distribution shows a dominating fraction in silt and clay with respectively 16 - 37 % clay, 49 – 61 % silt and 12 – 30 % sand (figure 4.4.1a), the largest proportion of clay seen through the core.

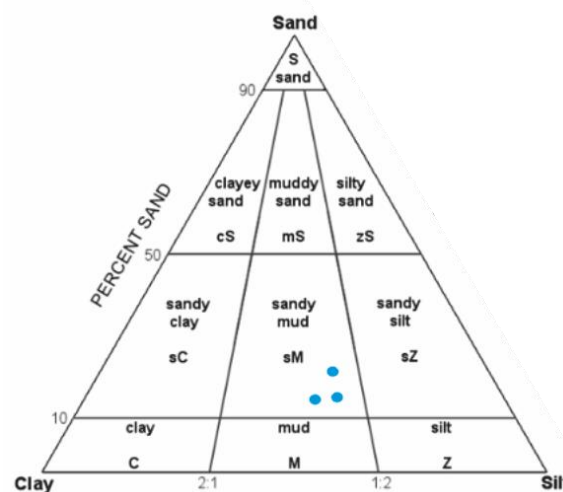


Figure 4.4.1a. Diagram showing the grain size distribution within unit 1 (Folk, 1954).

##### 4.4.1.2. Physical properties

The physical properties measured shows the lowest values for magnetic susceptibility seen through the core, with values showing a zig-zag pattern between 10 and 20 ( $10^{-8}$  SI( $m^3/kg$ )). The water content is more uniform and around 20 % (figure 4.4b).

##### 4.4.1.3. Element geochemistry

Unit 1 contains relatively high amounts of Silicon (Si/sum) and Sulfur (S/sum) (figure 4.4c and appendix: 1 table 1). In the element/element ratios the Strontium/Calcium (Sr/Ca) ratio is relatively high and fluctuating (figure 4.4c and appendix: 1 table 1). The other values do not deviate from the unit above.

#### 4.4.1.4. Interpretation

Based on the results listed above, unit 1 is interpreted to represent the upper part of a high velocity debris flow deposit (figure 4.4.1b). As seen in the available swath bathymetry data (chapter 4.2), several submarine debris flows are located east of the core. Furthermore, the lithology and the physical properties are similar to the results presented by Laberg and Vorren (1995) studying debris flow deposits found to comprise a dark grey diamicton which was poorly sorted and with a high clast content. Debris flows deposited east of the core location shows a content of 20 - 40 % clay, 20 - 40 % silt and 10 - 30 % sand, which has similarities to the clay and sand content seen within MD992301. There is however a change in the content of silt, which has a higher percentage (49 – 61 %) than the debris flows identified by Laberg and Vorren (1995).

The uniform impact of the geochemical properties within the unit, indicates that the material is deposited by a single event of mass-wasting. The increase in Silicon (Si/sum) may represent a terrigenous/productivity indicator (Rothwell et al., 2006), and may therefore be a useful sediment-source indicator. An increase in the ratio between Strontium/Calcium (Sr/Ca) may also work as a provenance indicator as a higher amount of Strontium is an indicator of a more shallow-water sediment origin.

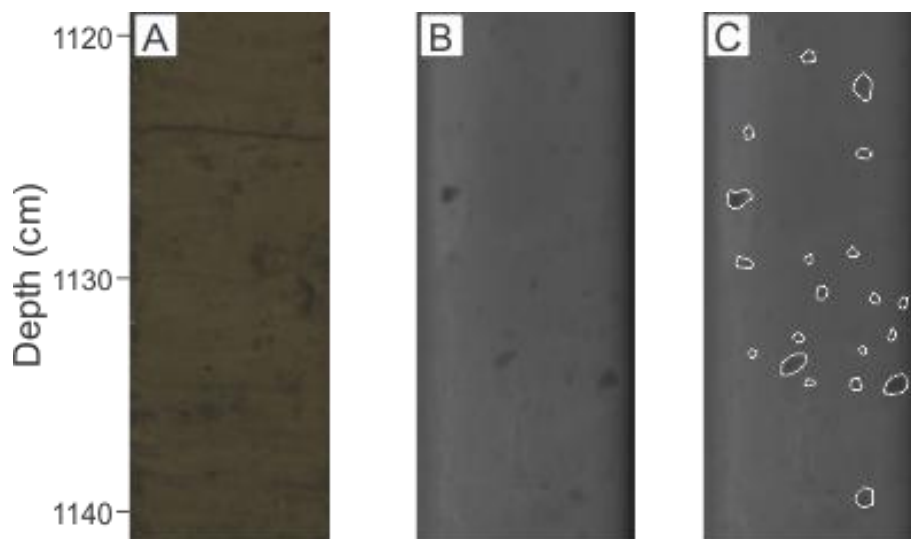


Figure 4.4.1b: Sequence of unit 1 viewed in A) color image, B) and X-ray, C) Interpretation of the unit, white discs indicates the location of scattered clasts.

## 4.4.2 Unit 2 (1031 – 999 cm)

### 4.4.2.1. Lithology and stratigraphy

Unit 2 comprise two facies, a dark colored sediment pellets interlayered with sandy silt lamina/layers. The color is very dark gray for the aggregates and black on the silty sand (figure 4.4a and 4.4.2a). In X-ray the images shows no signs of larger lithified clasts within this interval, but alternations between the lithologies are seen (figure 4.4.2a), where the thinnest laminae is around 0.4 cm thick, and the thickest layer is up to 2.1 cm.

The lower boundary of the unit is sharp and abrupt and the upper boundary is more gradual, and is estimated to be where there are no aggregates present (figure 4.4a).

Within the aggregates there are a dominance of sandy clay with values from 13-13.4 % clay, 40-46 % silt and 42-47 % sand. The interlayered sand is dominated by silty sand with 56 - 83 % sand and 4 - 7 % silt.

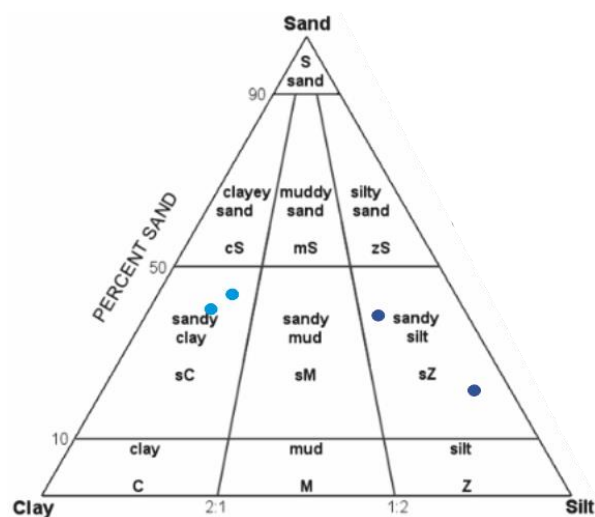


Figure 4.4.2a: Folks diagram showing the lithofacies distribution within unit 2. Light blue indicates the lithofacies in the pellets, and the dark blue the lithofacies within the sandy layers.

### 4.4.2.2. Physical properties

The physical properties measured through unit 2 shows the approximately same magnetic susceptibility values as for unit 1, ranging between 10 - 20 ( $10^{-8}$  SI( $m^3/kg$ )). The water content shows a decreasing down core trend (figure 4.4b).

#### 4.4.2.3. Element geochemistry

The XRF scan shows an enhancement in Manganese (Mn/sum) and Sulfur (S/sum) while a decreasing trend is seen for Silicon (Si/sum), Strontium/Calcium (Sr/Ca) and Potassium/Rubidium (K/Rb) (Figure 4.4c and Appendix 1: table 1).

#### 4.4.2.4. Interpretation

The aggregates look like dark colored “cottage cheese” and feels clayey when they are rolled between fingers. When the aggregates were crushed the sediment content showed to be muddy, and the aggregates are hence interpreted to be sediment pellets.

Sediment pellets are previously described by Goldschmidt et al., (1992), Henrich et al., (1989) and Vorren et al., (1998), from cores retrieved from the Norwegian Sea (Henrich et al., 1989; Goldschmidt et al., 1992; Vorren et al., 1998) and in the Arctic Ocean (Clark et al., 1980; Goldstein, 1983; Minicucci & Clark, 1983).

The origin and mode of deposition of sediment pellets are still discussed. A glacial origin were proposed by Clark et al., (1980) and Minicucci & Clark (1983), while a sea ice origin were suggested from Goldstein (1983). Sediment pellets may also have a fecal origin, but due to the large size, this are considered unlikely (Goldstein, 1983; Goldschmidt et al., 1992).

The sediments found in iceberg are predominantly coarse-grained with a mean around 1000 $\mu\text{m}$  and with no grains less than 250  $\mu\text{m}$ . Sea ice pellets contains finer sediment with no grains larger than 500  $\mu\text{m}$  and a mean between 10-20  $\mu\text{m}$  (Goldschmidt et al., 1992).

The pellets described in MD992301 are hence interpreted to have a sea ice origin, indicating that the cored location must have been overlaid by sea ice at the time of deposition.

The interbedded sand is assumed to originate from a different process (figure 4.2.2b). Two different processes were suggested by Vorren et al., (1998) and Svindland and Vorren (2002): 1) Winnowing (selective removal of finer grains from the sediment in a flow), and 2) that the sand is a part of an ongoing turbidite current interrupted with sediment pellets deposited by sea ice. Due to the erosional base and the enhancement of unit 2, the second suggestion is favored, where the turbidite either has continued to flow through unit 3, or there is two or more separate turbidite sequences. In that case, this indicates that the three lowermost units within MD992301 are deposited during full-scale glaciation. The XRF varies through the unit which shows a change in geochemical content, supporting the interpretation that there is a change in origin and deposition between the facies. The XRF for facies 2 shows an increase in

sulfur, which indicates a larger content of organic material (Croudace et al., 2006).

Unit 2 is interpreted to include sediment pellets formed and dropped by sea ice (Henrich et al., 1989; Goldschmidt et al., 1992). This indicates that it must have been favorable climate for sea ice formation, and the sea surface above the location of the core must have been covered by the sea ice in the period of deposition. Colder climate and formation of dense water moving down slope formed by cooling, may trigger the formation of small slides that transformed into turbidity currents in conformity with the interpretation of Svindland & Vorren (2002) studying similar deposits from the Arctic Ocean.

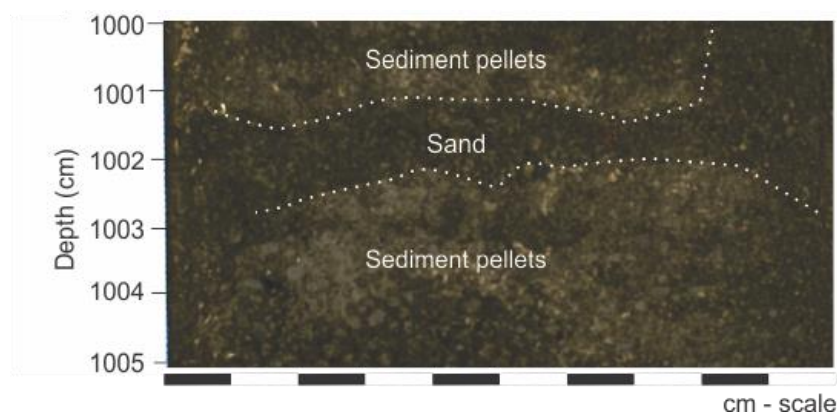


Figure 4.4.2b: Close up picture of the sediment pellets found in unit 2. The picture has manipulated contrasts to be able to see the pellets.

#### 4.4.3 Unit 3 (999 – 961 cm)

##### 4.4.3.1. Lithology and stratigraphy

Unit 3 comprises a 62 cm thick normal graded black silty sand (figure 4.4a). The grain size distribution shows 54 – 86 % sand, and 11 - 33 % silt, and shows a normal grading (fining upward) pattern were found for this unit (table 4.4.3a).

The lower boundary is estimated to be where there is no longer any sediment pellets present, and the upper boundary is gradual as more silt is incorporated. In X-ray images it is possible to see internal structures within the sand similar to subsequences found in a sandy Bouma sequence (figure 4.4.3b). The lowermost sequence is interpreted to be a lower massive unit, Ta (massive/graded turbidite) and the smaller laminae on top of Ta correspond to Tb (parallel laminated sand) and the cross-bedded stratigraphy corresponds to Tc (ripples and convolute bedding). The parallel layer above is interpreted to be Td (parallel laminae) and the massive sequence on top is hemipelagic/turbidite mud, which may correspond to Te.

Depth (cm)	Silt %	Sand %	Average size (µm)	Facies
963.5	33.3	54.2	238.9	zS
967.5	14.8	75.7	294.4	mS
979.5	11.7	86.2	463.3	zS
989.5	12.4	85.0	401.4	zS

Table 4.4.3a: Table showing the grain size distribution through unit 3.

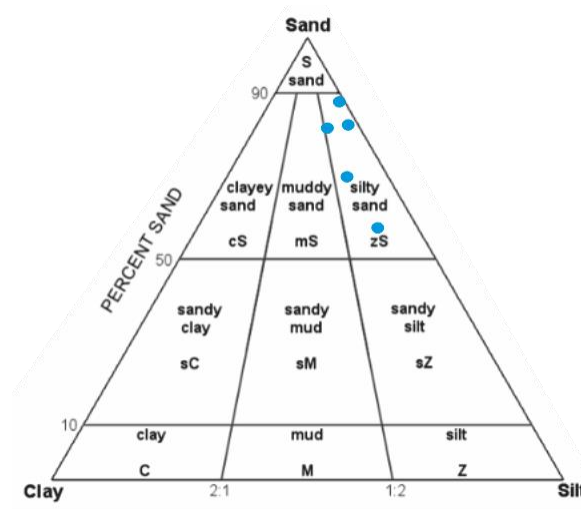


Figure 4.4.3a: Diagram showing the lithofacies distribution of the samples taken within unit 3 (Folk, 1954).

#### 4.4.3.2. Physical properties

As for the units below the magnetic susceptibility has a constant low value between 10 – 20 ( $10^{-8}$  SI( $m^3/kg$ )). The same trend is found in the water content which shifts frequently between 10 – 20 % (figure 4.4b).

#### 4.4.3.3. Element geochemistry

The geochemical elements within unit 3 shows an increase in Iron (Fe/sum) and Strontium/Calcium (Sr/Ca). Other elements which shows a decreasing trend includes Silicon (Si/sum) and Potassium/Rubidium (K/Rb) (figure 4.4c and appendix 1 table 1).

#### 4.4.3.4. Interpretation

Sandy sequences similar to the ones found in the retrieved core interval is previously described by (Laberg & Vorren, 1996a; Polyak & Mikhailov, 1996; Vorren et al., 1998; Piper et al., 1999; Laberg et al., 2010). They have interpreted the sandy sequences to be turbidite

deposits, deposited during full glaciations. In the XRF an increased amount of Sr/Ca in MD992301 is a possible indicator of a shallow water source. While Rubidium often is enhanced in bases of turbidites (Rothwell et al., 2006). Based on the results listed above unit 3 are assumed to be a sandy turbidite sequence.

As described above (chapter 2.6.4.4) the formation of turbidity currents may have several origins: 1) initiated from cascading of cold, dense bottom water, 2) sea ice formation and brine rejection, or 3) as small slides transforming into turbidity currents down slope. Turbidity currents are gravity driven, erosional currents and will incorporate material to the current diminish. When traveling down the channel, the turbidity current is confined between the channel walls. When the current reaches the bankfull stage the turbidity flow spills over the confinement and may be deposited in the overbank area on a levee similar to the location of MD992301 (Vorren et al., 1998). The INBIS channel is hence assumed to have been an important contributor for the sandy sequences found within the core, as the channel may have worked as a conduit for the flow towards the deep sea (Laberg et al., 2010).

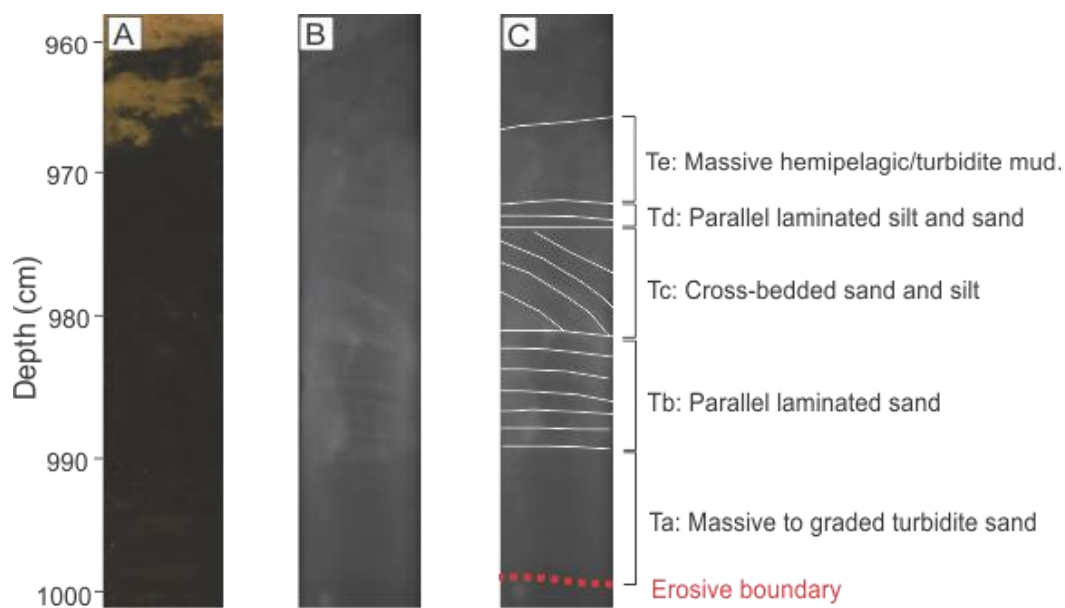


Figure 4.4.3b Turbidite sequence found in unit 3. A) color image, B): X-ray image of the unit, C) interpretation, showing a Bouma sequence.

#### 4.4.4 Unit 4 (961-943 cm)

##### 4.4.4.1 Lithology and Stratigraphy

The lithology within unit 4 includes silt, mud and sandy silt lithofacies with an olive color (figure 4.4a). The lower boundary is gradual, while the upper boundary is sharp and erosive. By conducting a grain size analysis the composition of the unit was retrieved: 27 - 51% clay, 48 - 66% silt and 7 - 16% sand (figure 4.4.4a). In X-ray images it is possible to see a sparse amount of scattered clasts within the mud, but no other internal structures (figure 4.4.4b).

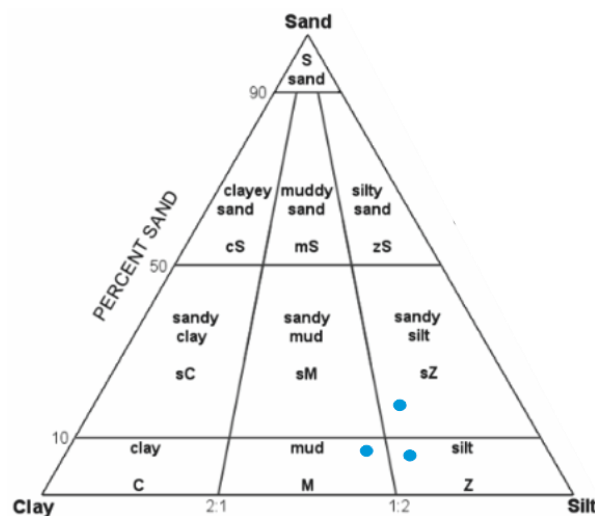


Figure 4.4.4a: Diagram based on folk (1954) showing the lithofacies seen in unit 4.

##### 4.4.4.2 Physical parameters

Both of the physical parameters measured by the MSCL shows an increase. The magnetic susceptibility increases with around 20 ( $10^{-8}$  SI( $m^3/kg$ )) with a distinct peak at ~960 cm. Also the water content shows an increase with around 10% from ~10 – 20%.

##### 4.4.4.3 Element geochemistry

The XRF data through unit 4 showed an increase in Silicon (Si/sum) and in the relationship between Calcium/Iron (Ca/Fe). While the rest remain fairly uniform (Appendix 1: table 1 and figure 4.4c).

##### 4.4.4.4 Interpretation

Based on the massive structure less muddy lithology with a sparse amounts of clasts. The material within unit 4 is assumed to be hemipelagic mud falling directly out of suspension in a

marine environment and settled on the seafloor previously as described by Bowles et al., (2003). The material includes bioclastic material (remains of calcareous organisms and siliceous skeletons) indicated by the increase in Ca/Fe ratio is indicative of the biogenic:detrail clay ratio (Rothwell et al., 2006), Indicating a larger presence of carbonate within the unit, while an increased amount of Silicon can indicate changes in the content of terrigenous material and hence may work as a provenance indicator and may be enriched in quartz grains. The clasts observed within the unit is hence believed to be deposited during the deposition of the units, and not during the hemipelagic deposition.

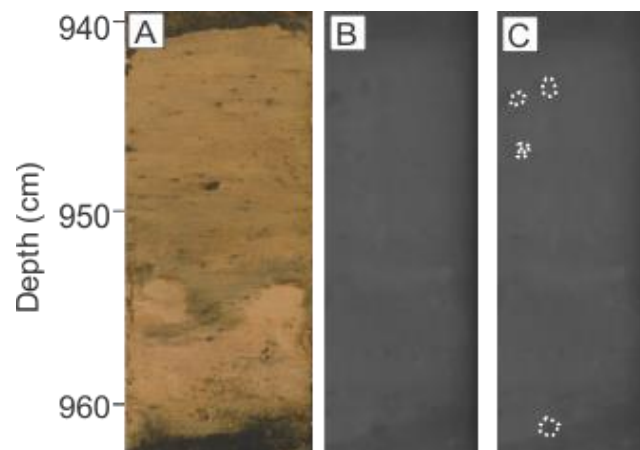


Figure 4.4.4b Section of unit 4. A) Color image, B) X-ray photo and C) interpreted X-ray. The white dotted discs are interpreted as clasts.

#### 4.4.5 Unit 5 (943-937 cm)

##### 4.4.5.1 Lithology and stratigraphy

Unit 5 is a 6 cm thick layer of dark (black) muddy sand (figure 4.4.5a). By analyzing the data retrieved from the grain size analysis the lithofacies are estimated to contain: ~11% clay, 19% silt and 69% sand. Both in X-ray and color images there is a clear erosive boundary at the bottom of the unit, while the upper boundary is more undulating.

No clear internal structures or clasts are seen in the photos or observed directly on the split core surface.

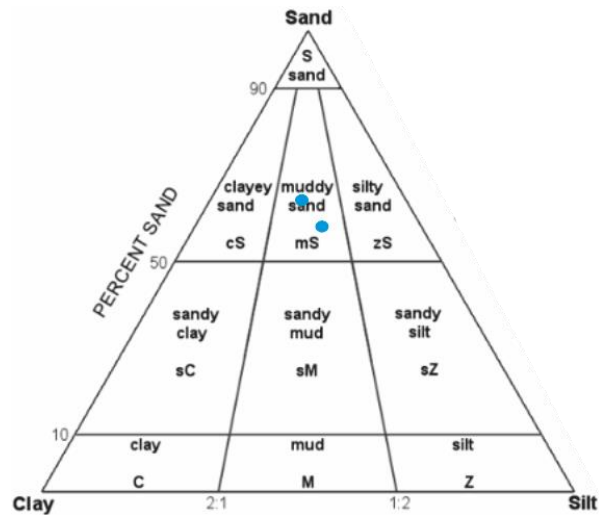


Figure: 4.4.5a: Diagram showing the lithofacies distribution through unit 5 (based on folk (1954)).

#### 4.4.5.2 Physical properties

The physical properties of the unit shows a decrease in both magnetic susceptibility and water content. The magnetic susceptibility decreases from 40 to 20 ( $10^{-8}$  SI( $m^3/kg$ )) and the water content from 20 - 10 %.

#### 4.4.5.3 Element geochemistry

The collected XRF data from unit 5 shows an increase in Zirconium (Zr/sum) and a smaller peak in Sulfur (S/sum). Strontium/Calcium (Sr/Ca) and Calcium/Iron (Ca/Fe) also increases (figure 4.4c and table 1 found in appendix 1).

#### 4.4.5.4 Interpretation

Sandy units within the Bear Island TMF succession have previously been described by Vorren et al., (1998) and Laberg and Vorren (1996a). Due to strong similarities to the sandy unit of unit 3, also this unit is interpreted as a part of a turbidite deposit (figure 4.4.5b). XRF data collected from unit 5 correlated to unit 3 (figure 4.4c), and it is hence a possibility for the same provenance area. As mentioned in the interpretation of unit 3 an increase in Sr/Ca may indicate a shallow water source and Sulfur is known for an increased amount of organic rich minerals, while the incensement in the heavy resistance mineral Zr often is viewed in the base of turbidites (Croudace et al., 2006; Rothwell et al., 2006).

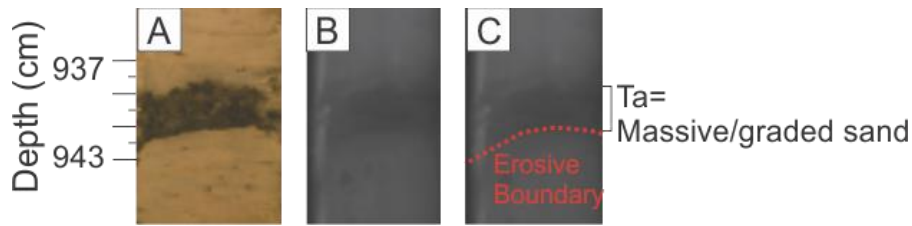


Figure 4.4.5b: Figure comprising unit 5. A) Color image, B) X-ray photo and C) interpretation.

#### 4.4.6 Unit 6 (937 -776 cm)

##### 4.4.6.1. Lithology and stratigraphy

Unit 6 includes layers of sandy silt, with smaller contributions of silt, mud and sandy mud. The sand percentage within the unit is ranging between 8 - 34% and has a silt content of 46 - 74 % (figure 4.4b and 4.4.6a). In X-ray finer lamination (822-792) and a sparse number of random distributed clasts (792-776 cm and 868-822 cm) are observed. Frequent color changes between olive, olive brown, grayish brown and dark grayish brown are seen through the unit, corresponding with the laminae (figure 4.4a). The upper boundary is truncated by the unit on top and the lower boundary is more gradual and unclear.

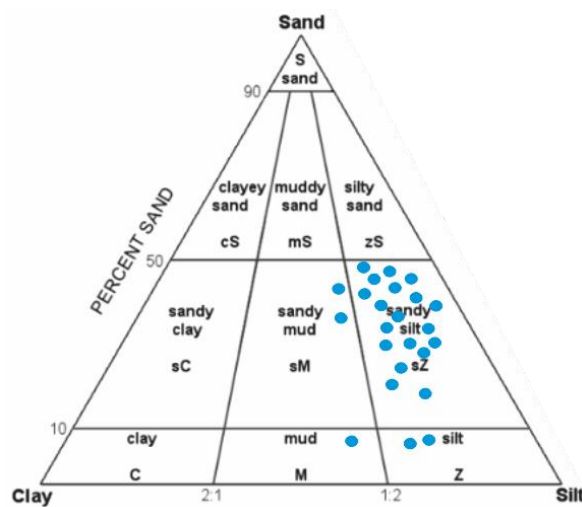


Figure 4.4.6a: Diagram showing the litho facies distribution (Folk, 1954) of the samples taken within unit 6.

##### 4.4.6.2. Physical properties

The physical properties of unit 6 shows an increase in both water content and magnetic susceptibility. The magnetic susceptibility within the unit is fluctuating varying from 15 – 60 ( $10^{-8}$  SI(m<sup>3</sup>/kg)). As a consequence of a more silt rich layer the water content starts to increase with values between approximately 3 - 30 %, where the highest values are found in the center part of the unit (figure 4.4b).

#### 4.4.6.3. Element geochemistry

By using the XRF scan an increased amount of Calcium (Ca/sum) and in the relationship between Calcium/Iron (Ca/Fe) is found (figure 4.4c and d). The other measurements remains uniform.

#### 4.4.6.4. Interpretation

The dominance of a more massive mud with a smaller interval of laminated mud, with occasional dropstones indicates deposition in a glaciomarine environment (Laberg & Vorren, 1995). An abrupt change in color indicates a frequent change in source area (Forwick & Vorren, 2009) as described in unit 4. The mud is most likely deposited by suspension fall-out from turbid sediment-laden glacial meltwater plumes previously described by Pfirman & Solheim (1989), and the clasts observed in X-ray are interpreted to be ice rafted debris (IRD) from icebergs and/or sea ice described in chapter 2.6.4.5 (Vorren et al., 1983; Dowdeswell & Dowdeswell, 1989) (figure 4.4.6b). This depositional characteristics indicate an ice-distal glaciomarine sediment accumulation, which mainly comprises sediment deposited by icebergs and melt-water plumes during withdraw of a glacier (Pfirman & Solheim, 1989; Pfirman et al., 1994).

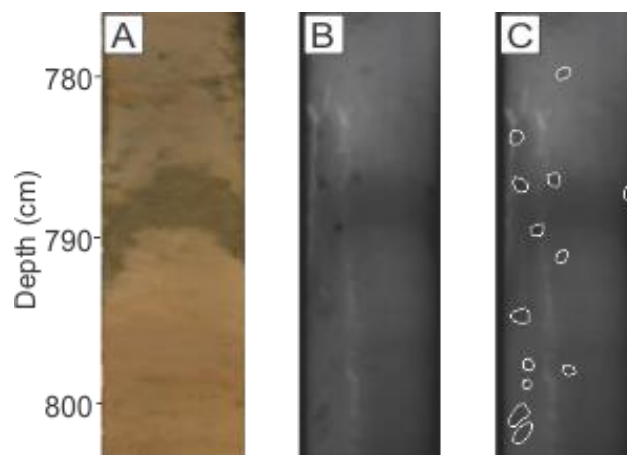


Figure 4.4.6b: A: color image of interval in unit 4, B: X-ray photo, C: Interpretation; white dotted discs indicates clasts/IRD.

#### 4.4.7 Unit 7 (776 – 697 cm)

##### 4.4.7.1. Lithology and stratigraphy

Unit 7 starts with a sandy peak at 776 centimeters and marks the start of an interval of more grayish material (figure 4.4a). The color of the sequence varies between very dark grayish brown at the bottom to a more frequent change between olive gray, very dark gray and very

dark grayish brown in the upper parts. The grain size analysis shows 13 - 74 % sand and 19 - 57% silt within the unit (figure 4.4.7a), where the highest sand values are observed in the sandy peak at the bottom of the unit. This leaves a dominating sandy silt lithofacies changing to silty sand upwards through the unit. Within the sandy peak an upward fining were found using the maximum and average size parameter from the grain size analysis (table 4.4.7a). In X-ray the sand layer appears massive, with a sharp and erosive lower boundary, and a more gradual top ending.

Depth	Silt %	Sand %	Maximum size (µm)	Average size (µm)	Facies
773.5	22	72.6	256.9	85.7	zS
774.5	19	73.9	373.1	104.5	zS

Table 4.4.7a: Table showing the grain size content of sand and silt as well as the average size of the sandy peak in unit 5.

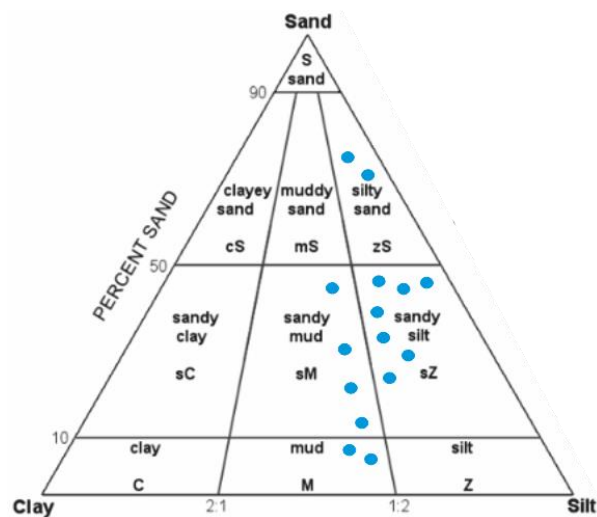


Figure 4.4.7a: Diagram showing the lithofacies distribution through unit 7 (Folk, 1954).

#### 4.4.7.2. Physical properties

The physical properties shows the same trends as the sandier layers below, with a clear decrease in both magnetic susceptibility and water content. This is a trend through the core in intervals where more sand is incorporated. The magnetic susceptibility varies between 10 - 30 ( $10^{-8}$  SI(m<sup>3</sup>/kg)) and the water content shows a fluctuating trend with values below 20 % (figure 4.4b).

#### 4.4.7.3. Element geochemistry

There is a marked change in the XRF data from unit 6 to unit 7, with an increase in Silicon (Si/sum), Iron (Fe/sum) and Zirconium (Zr/sum). In the element: element ratios there are an increase in one parameter: Strontium/Calcium (figure 4.4c and appendix 1: table 1).

#### 4.4.7.4. Interpretation

The unit has a sharp and erosive lower boundary, and a more gradual upper boundary. As in unit 3, the unit contains a darker colored silty sand changing to sandy silt up the core, indicating an upward fining. As the sandier sequences described above, unit 7 also shows a decrease in both water content and magnetic susceptibility (figure 4.4b). The occurrence of random sand lenses above the most sand rich layers are interpreted as deformed layers from synsedimentary deformation (Nichols, 2009) and/or disturbance during coring.

Both below and above the sandy unit there is a massive mud, containing random distributed clasts. Based on this it is possible that the sand was deposited in a period of glaciomarine sedimentation, interrupting the massive glaciomarine mud (figure 4.4.7b).

As previously mentioned Silicon may work as an indicator of productivity or terrigenous material, while the increase in Zirconium often is enhanced in bases of turbidites (Croudace et al., 2006). The increase in relationship between Strontium/Calcium can be related to the appearance of high Sr-aragonite minerals which requires a shallow water source (Rothwell et al., 2006).

Based on the interpretation above unit 7 is interpreted to be a smaller sandy turbidite deposited during a period of glaciomarine sedimentation. The XRF indicates material derived from a shallow shelf or continental areas before it was transported into the deep sea. The INBIS channel may have been active in this period, working as a conduit for turbidity currents towards the deep sea.

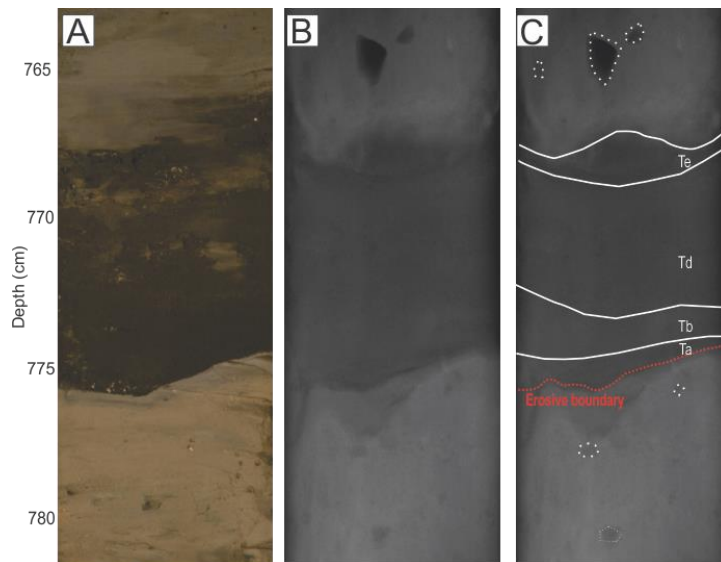


Figure 4.4.7b: Close up by the sandy turbidite sequence in unit 7. A) Color image, B) X-ray photo, C) Interpretation. White line = sequence boundaries, red line= erosive boundary, and white dotted circles = clasts/IRD.

#### 4.4.8 Unit 8 (697-484 cm)

##### 4.4.8.1. Lithology and stratigraphy

Unit 8 is dominated by a massive sandy silt lithofacies (figure 4.4.8a). The grain size distribution shows that the amount of clay varies between 9 – 61 %, silt varies between 30 - 72 % and the amount of sand is between 0 - 48 % giving a sandy silt lithofacies (figure 4.4b). There are frequent color shifts through the unit between different shades of olive gray and grayish brown (figure 4.4a). In X-ray, color images and visual description the boundaries are both classified as gradual. Also this unit contains scattered clasts. The rapid changes in color can be related to the content of silt and clay, where the clay rich layers hold a more grayish color, and the more silt rich layers have a brownish color. However, a larger content or organic material within the layers having a brownish color may also be an explanation, but this is hard to determinate based on the geochemical elements scanned.

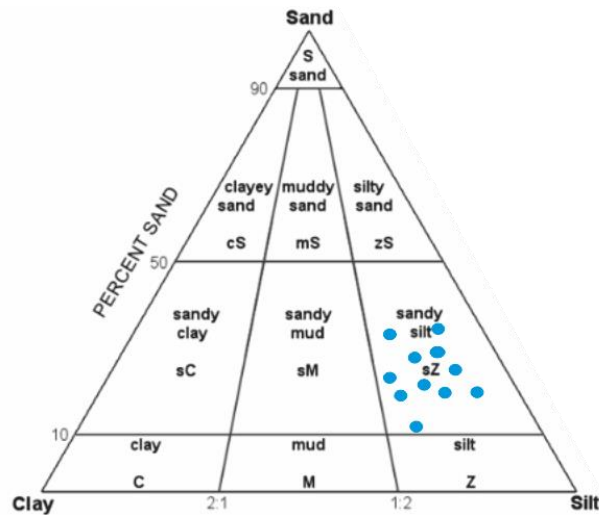


Figure 4.4.8a: Folks (1954) diagram over the lithofacies represented in unit 8.

#### 4.4.8.2. Physical properties

Within unit 8 there is once again an increase in both physical parameters measured as more silt and mud is incorporated into this unit. The magnetic susceptibility increases from around 17 – 40 ( $10^{-8}$  SI( $m^3/kg$ )). with some higher peaks (figure 4.4b). The water percentage increases with around 10 % within this unit.

#### 4.4.8.3. Element geochemistry

There are no clear peaks in the geochemical elements within this unit, but more uniform measures of low, intermediate or high values (figure 4.4c and table 1 in appendix 1). Sulfur (S/sum), Manganese (Mn/sum), and the ratio between calcium/iron (Ca/Fe) have very low values. The intermediate values are found in Silicon (Si/sum), Calcium (Ca/sum) and Iron (Fe/sum).

#### 4.4.8.4. Interpretation

The massive mud containing clasts within unit 8 has the same characteristics as unit 6. It is interpreted to represent mud deposited from meltwater plumes in a glaciomarine environment, and the clasts are hence suggested to be iceberg and/or sea ice deposited IRD (Vorren et al., 1983) (figure 4.4.8b).

There may be possible to correlate the frequent change in color to changes in source area (Forwick & Vorren, 2009), and/or smaller variations in organic carbon content.

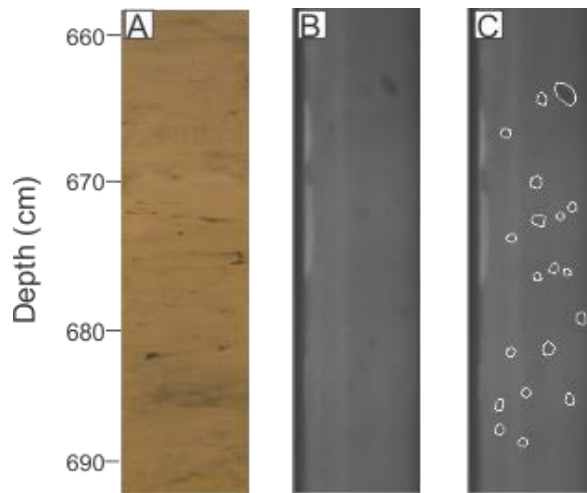


Figure 4.4.8b: Lithology of unit 8. A) photo of sediment surface B) in X-ray, C) interpretation where the white dotted circles indicates clast/IRD.

#### 4.4.9 Unit 9 (484-462 cm)

##### 4.4.9.1. Lithology and stratigraphy

Unit 9 has a sandy silt lithofacies containing 11 - 39% clay, 44 - 65% silt and 15 - 29% sand (figure 4.4.9a). There is a frequent change in color through the unit, changing between different shades of olive brown (figure 4.4a). In the X-ray images it is possible to see a decrease in the content of scattered clasts but no other internal structure or bioturbation. Both of the boundaries are gradual, based on geochemical differences.

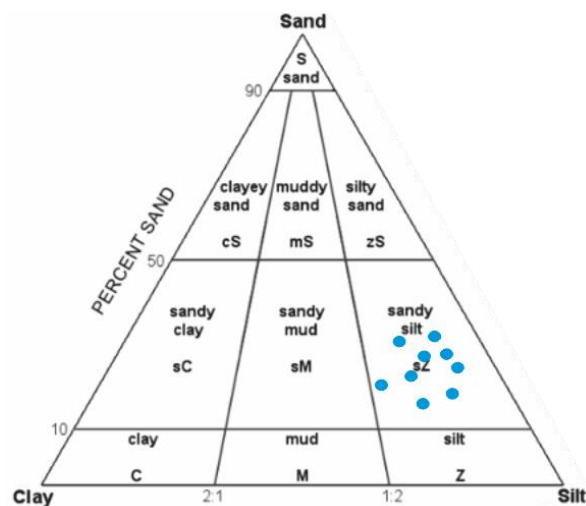


Figure 4.4.9a: Diagram showing the lithofacies distribution in unit 9 based on folks diagram (1954).

#### 4.4.9.2. Physical properties

Unit 9 is fairly similar to unit 8, besides a small increase in magnetic susceptibility from about 35 to 40 ( $10^{-8}$  SI( $m^3/kg$ )). The water content shows a higher frequency zig zag pattern, but entrains the same values as the units around, ranging between 10 – 20 % (figure 4.4b).

#### 4.4.9.3. Element geochemistry

Unit 9 shows an increase in Manganese (Mn/sum) as the only element having an impact in unit 9, increasing from 0.2 – 0.6 cps (counts per second) (figure 4.4c) (appendix 1: table 1).

#### 4.4.9.4. Interpretation

The interpretation of unit 9 is the same as for unit 6 and 8, representing a glaciomarine environment, with a large flux of glacial meltwater indicating a retreat of the ice (figure 4.4.9b).

The increase in manganese and decrease in IRD are thought to reassemble a change in provenance of the sediment. (Vorren et al., 1983).

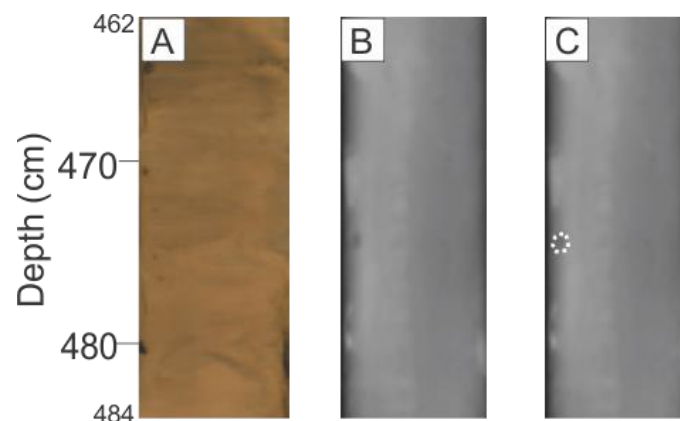


Figure 4.4.9b: Figure showing the interval of unit 9. A) Color image, B) X-ray photo and, C) interpretation.

#### 4.4.10 Unit 10 (462 – 271/268 cm)

##### 4.4.10.1. Lithology and stratigraphy

Unit 10 is fairly similar to unit 8. The unit is dominated by sandy silt with 7 - 34 % clay, 39 - 69% silt and 11 - 50% sand (figure 4.4.10a). The color shifts between different shades of olive brown. In the X-rays no inner structure were identified but several randomly distributed clasts are seen through the unit (figure 4.4a). The lower boundary is gradual while the upper boundary is sharp, truncated and erosive.

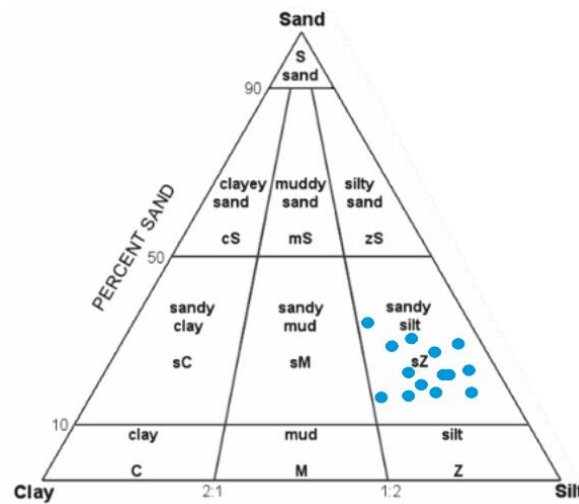


Figure 4.4.10a: Diagram showing the lithofacies distribution of the samples taken within unit 10 (Folk, 1954).

#### 4.4.10.2. Physical properties

Within unit 10 the magnetic susceptibility becomes more constant with values ranging from 35 - 40 ( $10^{-8}$  SI( $m^3/kg$ )), increasing towards the top. The water percentage shows a slight increase from the surrounding units, and has a value around 30 % (figure 4.4b).

#### 4.4.10.3. Element geochemistry

The element geochemistry is similar to what was observed in unit 8, with more constant values of low and moderate measurements (table 4.4b). Zirconium (Zr/sum), Sulfur (S/sum) and Manganese (Mn/sum) have low values. Intermediate values are found in Silicon (Si/sum), Calcium (Ca/sum), Iron (Fe/sum) and Calcium/Iron (Ca/Fe) (figure 4.4c and appendix 1: table 1)

#### 4.4.10.4. Interpretation

Unit 10 also contains a massive mud including random distributed clasts (figure 4.4.10b). As mentioned previously, interpreted to represent a glaciomarine environment where the clasts are IRD deposited by icebergs or sea ice (Vorren et al., 1983).

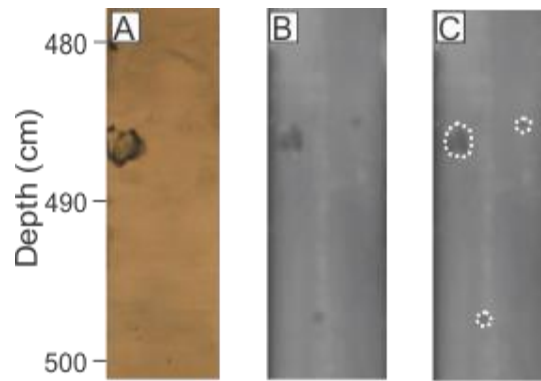


Figure 4.4.10b: Image of a section in unit 10. A: surface image of the cored material, B: X-ray image of the sediment section, and C: Interpretation of the material. While dotted circles= clasts/IRD.

#### 4.4.11 Unit 11 (271/268 – 201 cm)

##### 4.4.11.1. Lithology and stratigraphy

Unit 11 is the uppermost sand rich unit within MD992301. The grain size analysis shows a silty sand lithofacies (figure 4.4.11a) with values ranging from 50 – 81 % sand and 12 – 40 % silt (figure 4.4b). Both in visual description and grain size analysis shows a normal grading pattern with an upward fining sequence based on average and maximum grain sizes within the unit (table 4.4.11a). The boundaries are characterized by a sharp and erosive transition at the bottom and gradual shift on top. The color of the unit is dark olive brown at the top that gradually changes to very dark greyish brown towards the bottom (figure 4.4a).

In the X-ray images shows an inner structure of the sandy unit that may correspond to parts of a Bouma sequence. Above the erosive boundary from ~270 – 258 cm a massive too graded turbidite sand is interpreted to represent Ta, above this the sand becomes more parallel laminated, corresponding Tb. The grain size analysis revealed an increase in silt content from approximately 244 cm down core, while the sediments were still parallel laminated, and are interpreted to represent Td. On the top of the unit, the inner structures fades and there is a more massive hemipelagic/turbidite mud from 244 – 232/228 cm, corresponding to Te.

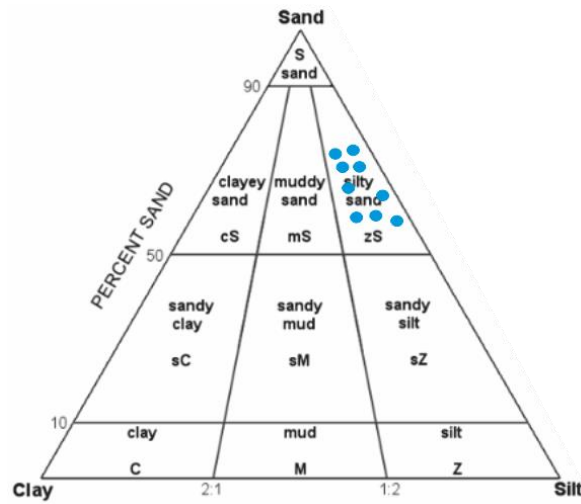


Figure 4.4.11a. Diagram showing the litho facies distribution of the samples taken within unit 9 (Folk, 1954).

Depth (cm)	Silt %	Sand %	Maximum grain size ( $\mu\text{m}$ )	Average size ( $\mu\text{m}$ )	Facies
241.5	38.6	50.4	282	62.5	zS
246.5	40.2	51.9	309.6	62.7	zS
251.5	31.1	63.5	309.6	74	zS
256.5	25	68	339.9	83.5	zS
262.5	16.8	78.1	1254.5	134	zS
269.5	12.4	81.5	1511.8	271.8	zS

Table 4.4.11a: The table show the grain size distribution through unit 9.

#### 4.4.11.2. Physical properties

Similar to the sand rich layers down core there is a large decrease in both magnetic susceptibility and water content within this unit. The magnetic susceptibility falls from ~40 to 10 ( $10^{-8}$  SI( $\text{m}^3/\text{kg}$ )) and the water content drops from 40% to around 3 %. Both graphs has a gradual increase towards the top as more silt gets incorporated (table 4.4.11a and figure 4.4b).

#### 4.4.11.3. Element geochemistry

The XRF data shows an increase in Silicon (Si), Sulfur (S) and Zirconium (Zr). Within the element/element ratios there are an increase in Strontium/Calcium (Sr/Ca) and Zirconium/Rubidium (Zr/Rb) (Appendix 1: table 1 and figure 4.4c).

#### 4.4.11.4. Interpretation

Based on the erosive lower boundary and sandy content with a normal grading pattern seen in table 4.4.11a and figure 4.4.11b the unit is interpreted to be a sandy turbidite. In figure 4.4.11 clasts are seen below and above the unit, indicating that the turbidite sequence is deposited in a glaciomarine environment, interrupting the deposition of clast holding mud probably during full-scale glaciation. As mentioned previously, an increase in the relationship between Sr/Ca indicates a shallow water source as the sediments gets enriched in high-Sr aragonite, while Zr/Rb are enriched in heavy resistant minerals and may be enhanced in turbidite bases (table 4.4b) (Croudace et al., 2006; Rothwell et al., 2006).

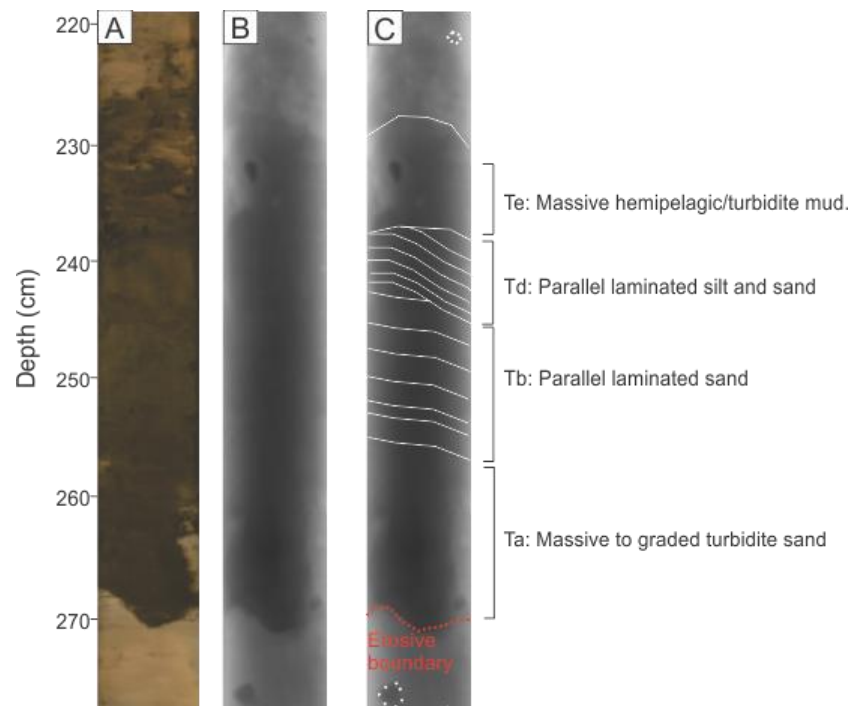


Figure 4.4.11: A) color picture of the core surface, B) X-ray image and C) interpretation of the interval in unit 11. White lines=sequence boundaries, red line= erosive lower boundary and white dotted circles= clasts/IRD.

#### 4.4.12 Unit 12 (201 – 148 cm)

##### 4.4.12.1. Lithology and stratigraphy

This unit is fairly similar to unit 8 and 10, a massive mud containing clasts. The grain size distribution is dominated by a sandy silt lithofacies (figure 4.4.12a) with values ranging between 55 – 74 % silt and 18 – 30 % sand (figure 4.4b). Through the interval there is a shift in color between different shades of olive brown (figure 4.4a). In the X-ray and color photos taken of the unit it is possible to see scattered clasts but no other internal structure. No distinct lower boundary is seen, but the upper boundary is slightly erosive and truncated.

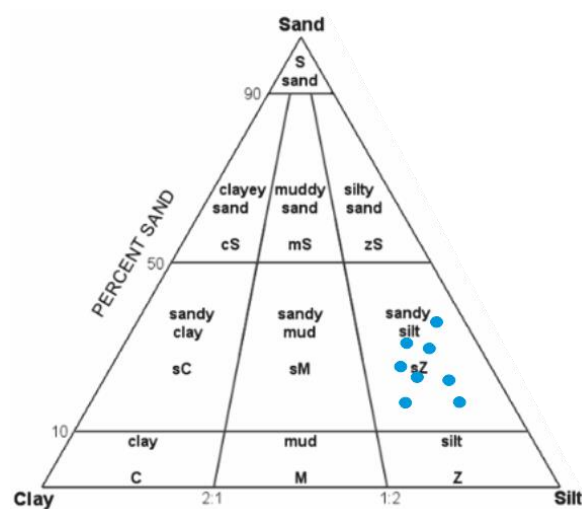


Figure 4.4.12a. Diagram showing the lithofacies distribution within unit 12 based on Folk's classification from 1954.

##### 4.4.12.2. Physical properties

The physical properties of the unit show clear similarities to previous described units, with a high magnetic susceptibility and water content. The water percentage changes between 27 – 36 %, and the magnetic susceptibility shows a high frequency zig-zag pattern with values between 19 - 72 ( $10^{-8}$  SI(m<sup>3</sup>/kg)) (figure 4.4b).

##### 4.4.12.3. Element geochemistry

Like some of the other units mentioned above unit 12 has no distinct peaks in the XRF measurements. There are uniform intermediate and low values. The low values resemble Sulfur (S/sum), Manganese (Mn/sum) and Zirconium (Zr/sum). The intermediate elements are Iron (Fe/sum) and Silicon (Si/sum) (Appendix 1: table 1 and figure 4.4c).

#### 4.4.12.4. Interpretation

The massive mud with random distributed clasts are interpreted to be deposited in a glaciomarine environment (figure 4.4.12b). Clasts seen in the X-ray photos are thought to be ice rafted debris, transported by either icebergs or sea ice (Vorren et al., 1983), while the lenses containing fractions of sand are indicated as deformed layers from synsedimentary deformation (Nichols, 2009). A more uniform color through the interpreted interval may indicate a more stable source area than the ones previous units described.

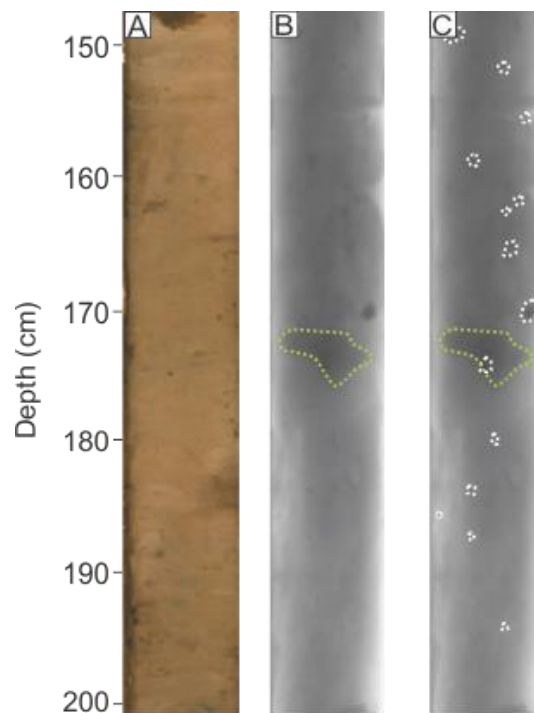


Figure 4.4.12b: The figure shows a color image of unit 12 (A), x-ray photo (B), and an interpretation (C). The white dotted circles indicated IRD/clasts and the green dotted figure indicates area with synsedimentary deformation.

#### 4.4.13 Unit 13 (148 - 52 cm)

##### 4.4.13.1. Lithology and stratigraphy

Unit 13 is dominated by frequent shifts between smaller pulses fine silty sand interlayered with sandy silt and mud (figure 4.4.13a). There is a total of 3 smaller sandier layers observed within the unit based on a slight color change and the grain size variation (table 4.4.13a).

Within the sandy sequences the clay content varies between 4.2 – 8.4 % clay, 20.8-38.3 % silt and 54.5 – 75.1 % sand. In the interlayered sandy silt the grain size distribution changes to 6.6-20 % clay, 44.6 – 74.2 % silt and 17.9 – 48.3 % sand (figure 4.4b).

The boundaries within the unit is slight erosive on the bottom and more gradual on top. The internal boundaries shows that the sandy pulses have an erosive lower boundary and a gradual

top boundary. The color within this unit changes rapidly between brown, very dark grayish brown and the sandier layers have an olive brown color (figure 4.4a).

The X-ray pictures no longer show any clasts, but turns slight darker within the intervals of the sandy layers, but neither of the facies show signs of inner structures.

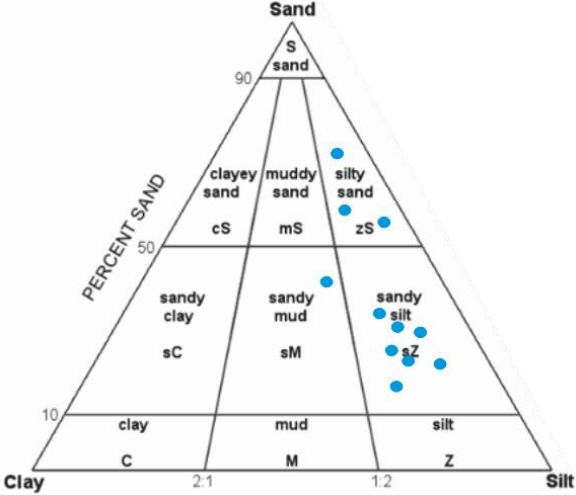


Figure 4.4.13a: Diagram showing the lithofacies distribution through unit 13 (based on Folk 1954).

Depth (cm)	Clay %	Silt %	Sand %	Average size	Facies	Pulse nr.
53.5	8.4	33.8	57.8	95.8	zS	Layer 3
68.5 - 80.5	14.1 - 33.1	46.3 - 51.5	20.6 - 37	38.1 - 87.2	sZ	-
89.5	7.2	38.3	54.5	81.1	zS	Layer 2
107.5-142.5	6.6-13.4	44.6 - 69	23.7 - 48.3	46.2 - 85.1	sZ	-
146.5	4.2	20.8	75	96.7	zS	Layer 1

Table 4.4.13a: Table showing the pulses of sand through unit 13. The samples between the sandy layers is merged together.

#### 4.4.13.2. Physical properties

Like in the sandier intervals below, the sandy peaks show a decrease in both water content and magnetic susceptibility, with higher values in the interlayered silt and mud. The magnetic susceptibility has values ranging from  $9 - (10^{-8} \text{ SI(m}^3/\text{kg}))$ . The water percentage varies between 11 to 59 %, increasing in the transition zone to unit 12.

#### 4.4.13.3. Element geochemistry

This unit has lower peak amplitudes than the sandier layers below, but still shows similar impact from the same elements: Zirconium (Zr/sum), Iron (Fe/sum), Manganese (Mn/sum) and Sulfur (S/sum). In the element: element ratios there is an increase in the relationship between Sr/Ca (Appendix 1: table 1 and figure 4.4c).

#### 4.4.13.4. Interpretation

Based on the grain size distribution and the visual description of the core unit 13 is found to include three pulses of sand interlayered with sandy mud and sandy silt (figure 4.4.13b). These frequent changes may be due to an unstable depositional environment shifting between mass-transport and hemipelagic suspension fall out. Mud interbedded with smaller sandy sequences are previously described on the northern levee of the INBIS channel by Vorren et al., (1998), interpreted to been deposited during Holocene. The depositional environment may have a hemipelagic origin interrupted by smaller pulses of fine grained sand. One possible explanation for the finer grained sandy pulses may by hypopycnal flow of cold dense water entrapping sediments which evolves into smaller sandy turbidity currents down slope. Another explanation may be erosion of sediments on the front of a traveling debris flow. Such flows may be initiated during the retreat of the glacier after LGM or ice free conditions, in a deglaciation phase. Which, due to the lack of clasts within this unit is favored (Elverhøi & Solheim, 1983; Bowles et al., 2003).

The XRF scan shows similarities to the sandier sequences down core, and shows as them an enhancement in the relationship between Sr/Ca, indicating a shallow water source. The increase in Zirconium is often seen in the bases of turbidites (Croudace et al., 2006; Rothwell et al., 2006). No internal structure is seen in the sandy pulses. The unit is interpreted to reassemble a constant shift in depositional environment with smaller sandy turbidities

interlayered with mud and silt during the transition from a glacial to an interglacial environment.

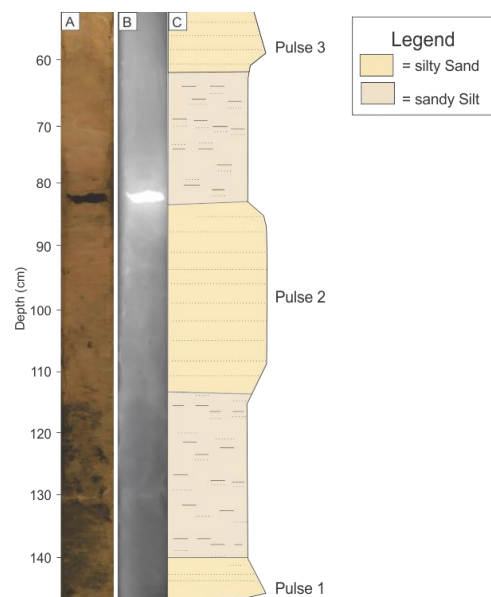


Figure 4.4.13b: Illustration over unit 13 A: color image, B) X-ray photo and C) Principal drawing.

#### 4.4.14 Unit 14 (52 – 0 cm)

##### 4.4.14.1. Lithology and stratigraphy

*The uppermost unit was disturbed during coring. Therefore, the upper part of unit 14 is marked with a red undulating line on the graphs showing the disturbed interval within the core. This area will not be discussed further in detail and below, descriptions “toward the top” is regarding the interval below the disturbed sediments.*

The dominating composition of unit 14 is sandy silt and silt (figure 4.4.14a). The clay content varies from 0 – 17 %, 47 – 78 % silt, and 16 – 45 % sand (figure 4.4b). There is a gradual change in color from very dark grayish brown on the top to olive brown further down core (figure 4.4a). Within this uppermost unit, the sediment contains some organic debris. Viewed in color image, X-ray photos and by visual interpretation the unit shows a chaotic internal structures, where the internal boundaries shows a concave shape due to the impact of the core tube. There are only gradual boundaries within the interval, and no internal structure or clasts.

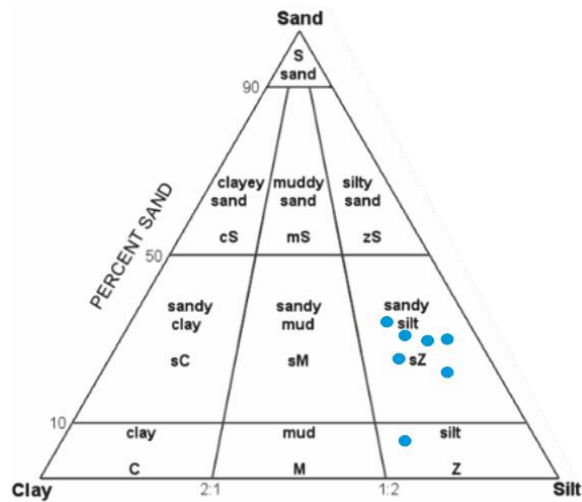


Figure 4.4.14a: The lithofacies distribution through unit 14 based on folks classification system from 1954.

#### 4.4.14.2. Physical properties

There is a decrease in magnetic susceptibility at middle of the unit from 40 – 20 ( $\times 10^{-8}$  SI ( $\text{m}^3/\text{kg}$ )) before it increases again towards the top to a value between 30 - 40 ( $10^{-8}$  SI( $\text{m}^3/\text{kg}$ )). The water content shows a different trend with a steady decrease towards the top of the unit, from around 60 % towards 10 % at the upper end of the core (figure 4.4b).

#### 4.4.14.3 Element geochemistry

The XRF data shows an increase in Calcium (Ca/sum), Calcium/Iron (Ca/Fe) and Potassium/Rubidium (K/Rb) (figure 4.4c). While the relationship between Zirconium/Rubidium (Zr/Rb) decreases (Appendix 1: table 1 and figure 4.4c).

#### 4.4.14.4. Interpretation

Based on the massive muddy lithology without any structures or clasts, the unit is assumed to be hemipelagic mud falling directly out of suspension in a marine environment and settled on the seafloor previously as described by Bowles et al., (2003) (figure 4.4.14b). The material includes bioclastic material (remains of calcareous organisms and siliceous skeletons) and organic debris. By picking the samples for foraminifera it showed that the sample contained more warm-water species than the samples extracted further down.

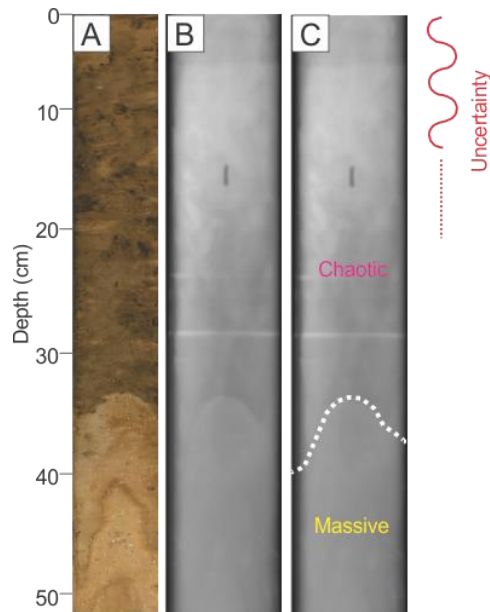


Figure 4.4.14b: Figure showing the lithology within unit 14. A) Color image, B) X-ray image and, C) Interpretation.

#### 4.5 Chronology and sedimentation rate through MD992301

MD992301 is suggested to contain material from ~166,000 to the Present. Within this timeframe a total of 14 different lithological units have been deposited as described above. Eight samples were collected from MD992301 for radiocarbon dating, where only 5 of them contained enough material for final preparation and radiocarbon dating. All five of the samples contained diverse planktonic foraminifera, where the uppermost dated interval from 32-33 cm contained a high diversity of warm water species. The deepest interval from 779-780 were dated to >50,000  $^{14}\text{C}$  and is hence excluded from this study. The samples were extracted from above and below sandy turbidites there are a possibility that some of the material was resuspended, and hence contributed to the reversed age at one level. We suggest that this was the case for the material extracted from between 199 – 200 cm core depth, and this dating is thus removed from the final plot.

The results from the  $^{14}\text{C}$  dating resulted in few dated levels making it difficult to do reliable assessment of the sediment accumulation rates. From the samples extracted from the upper 273 cm of the core an assumed linear sedimentation rate could be estimated. However, some more samples needs to be dated to get more reliable assessment of the sediment accumulation rate

The deepest interval where we were able to obtain reliable dating was located at 271 – 272 cm. An age of 19,278 cal yr BP was found here, while 18,788 was measured from 148-149 cm. The uppermost dated interval from 32-33 cal yr BP provided an age of 5668 cal yr BP (table 4.3.5). The following sedimentation rates have been estimated based on the <sup>14</sup>C dating's assuming a linear sedimentation rate and that the top of the core represents the present seafloor when the core was retrieved in 1999: In the uppermost interval (0-52 cm) the sedimentation rate is assumed to be 5.5 cm/kyr. The accumulation rate slightly increases from 51 - 201 cm, with an assumed rate of 8.8 cm/kyr. The lowermost interval able to be dated from 201 - 271 showed an increase in the sedimentation rate to 251 cm/kyr. This gives an estimated average linear sedimentation rate of 20.2 cm/kyr.

Based on an extrapolation of the 5.5 cm/kyr and 8.8 cm/kyr sedimentation rates (the 251 cm/kyr was considered representative for the last glacial maximum but too high for the present LGM deposits), the sediments from the base of the core to 271 cm core depth were considered deposited approximately from 166,000 – 19,278 cal yr BP, i.e. during the Saalian glaciation throughout Early and Mid-Weichselian. The material deposited from 271 – 149 represents Late Weichselian deposits, while 149-33 cm includes the Last Glacial Maximum, the last deglaciation and early Holocene. The interval from 33 – 0 cm was deposited during late Holocene.

## 4.6 Summary

In table 4.4.15a below a short summary of the presented results.

Facies	Unit(s)	Characteristics	Abnormalities
<b>Muddy debris flow diamicton</b>	Unit: 1	<ul style="list-style-type: none"> <li>- Dark muddy matrix.</li> <li>- Dark, angular and flat clasts.</li> <li>- Deposited by an ancient debris flow.</li> </ul>	
<b>Sediment pellets (mud)</b>	Unit: 2	<ul style="list-style-type: none"> <li>- Dark, hard clasts (pebbles) of sediment (looks like dark colored cottage cheese).</li> <li>- Laminated with sand.</li> <li>- Deposited by sea ice.</li> </ul>	
<b>Massive/graded sand</b>	Unit: 3, 5, 7, 11 and 13	<ul style="list-style-type: none"> <li>- Normal graded sand.</li> <li>- Dark olive brown /olive brown color (Munsell)</li> <li>- Deposited by turbidity currents.</li> </ul>	<ul style="list-style-type: none"> <li>- Unit 7 and 11 show an increase in Silicon, while 3 and 5 show a decrease.</li> <li>- Increase in Zirconium in every sand layers despite unit 3.</li> <li>- Unit 3 + 5 are similar and 7+11 + 13 are similar.</li> </ul>
<b>Homogenous, massive hemipelagic mud</b>	Unit 4 and 14	<ul style="list-style-type: none"> <li>- Massive mud without any internal structures.</li> <li>- Deposited by suspension fall-out.</li> </ul>	<ul style="list-style-type: none"> <li>- 4 contains some clasts interpreted to be deposited from the units below and above, rather than form icebergs during the period of deposition.</li> </ul>
<b>Massive glaciomarine mud with clasts</b>	Unit: 6, 8, 9,10 and 12	<ul style="list-style-type: none"> <li>- Massive muddy matrix with random distributed clasts.</li> <li>- Deposited by suspension fall-out from glaciomarine melt-out plumes.</li> <li>- IRD deposited by rafting from sea ice and/or icebergs.</li> </ul>	
<b>Massive laminated mud with clasts</b>	Unit: 6	<ul style="list-style-type: none"> <li>- Massive mud with internal lamination.</li> </ul>	

Figure 4.4.15a: Table summarizing the results through the different units within MD992301.



## 5. Discussion

In this chapter, the results presented will be further discussed in order to reconstruct the sedimentary processes, and paleoenvironment in the study area throughout the cored interval. The sedimentation rate and age correlation will be addressed first, and compared to previous sedimentation rates and age estimates from the same region.

Based on changes in lithology and mode of deposition, the core is divided into two parts: part 1 comprising units 1 - 3, containing mass-transported material of assumed to be deposited from the Saalian glaciation towards the transition to the Eemian interglacial. And part 2 comprising units 4 - 14, containing glaciomarine material assumed to be deposited during the Eemian interglacial, the Weichselian glaciation and Holocene.

## 5.1 Age model and sedimentation rates

Estimations of sediment ages and sediment rates are important tools in the correlation between different cores, and in the work of identifying stadials and interstadials within the core. In the following subchapters the sedimentation rates through MD992301 are going to be described in further detail to be able to provide a tentative age model for the whole core. The results is then going to be compared to cores previously described by Hald et al., (2001) and Laberg and Vorren (1995).

### 5.1.1 Sedimentation rate MD992301

To estimate the sedimentation rate within the core a linear and constant accumulation rate was assumed between the intervals dated, causing some uncertainties of the age model. Another error relates to possible intervals of erosion (for instance beneath sandy turbidites), which the age model don't take in to consideration assuming a constant sedimentation, as well as stretching of the different core sections during sampling, and uncertainties regarding the dating methods. The accumulation rate between the radiocarbon dating taken through MD992301 is given in centimeters per thousand years (cm/cal kyr BP). The linear sedimentation rates established from the core is listed in table 5.1.1.1 and shown on figure 5.1.1.

Due to the lack of datable material downcore from 271 cm core depth, an estimated linear age model based on the linear assumptions between 0 – 149 cm dated to be 0 – 5668 cal yr BP (A1), and 149 – 272 cm calibrated to 5668 – 18,778 cal yr BP (A2) are used and extrapolated down the core.

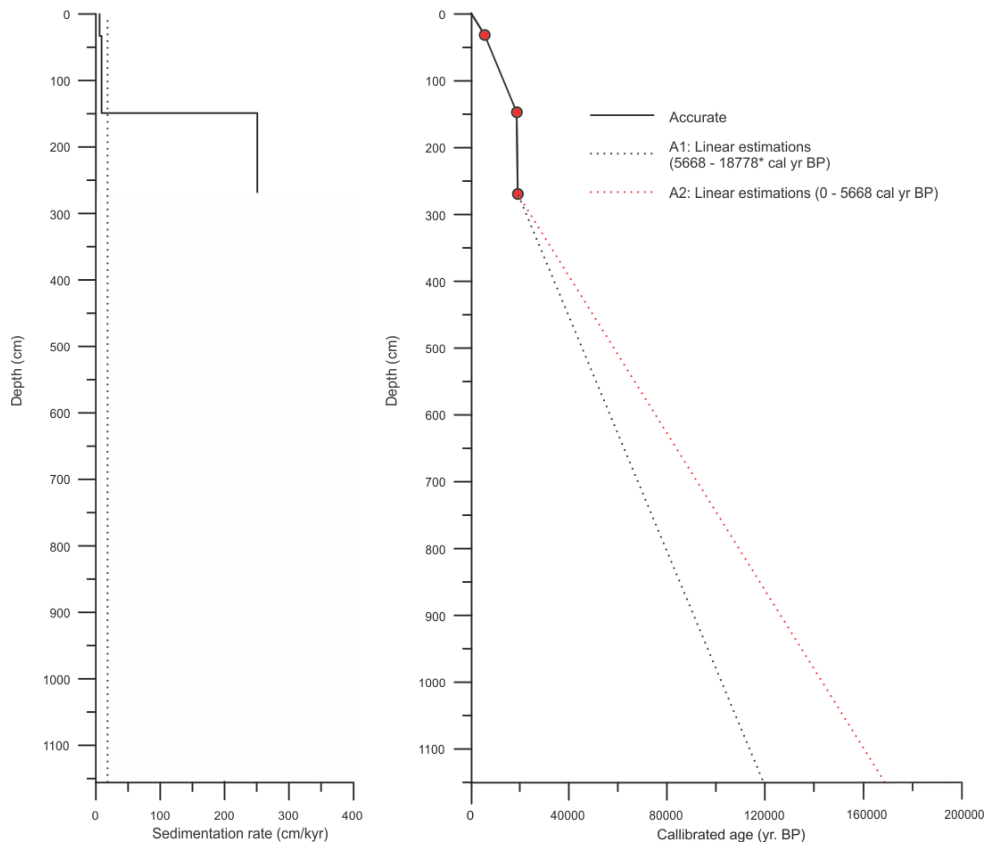


Figure 5.1.1: Sedimentation rates and age model of MD992301 based on calibrated years BP.

#### 5.1.1.1 Part 1:

In part 1, from 1156 – 961 cm no exact dating could be obtained as this interval is assumed to comprise sediments of an age beyond the limitations of the  $^{14}\text{C}$  method. Sedimentation rates and age of the deposited sediment within this interval is hence estimated based on a linear accumulation of the dated material. Which in this interval is assumed to be between ~98,000 – ~166,000 cal. yr. BP from extrapolation of the trends between 0 – 5668 and 5668 – 18778, respectively (A1 - A2) (figure 5.1.1.1 and table 5.1.1.1).

However, due to variation in the depositional regime the sedimentation rate is thought to change between the units within this part of the core. Estimating a higher depositional rate for the sandy turbidite in unit 3, and lower accumulation rate in the sediment pellets and debris flow. From the tentative chronology above, the sediments within part 1 of MD992301 is assumed to be related to the Saalian glaciation.

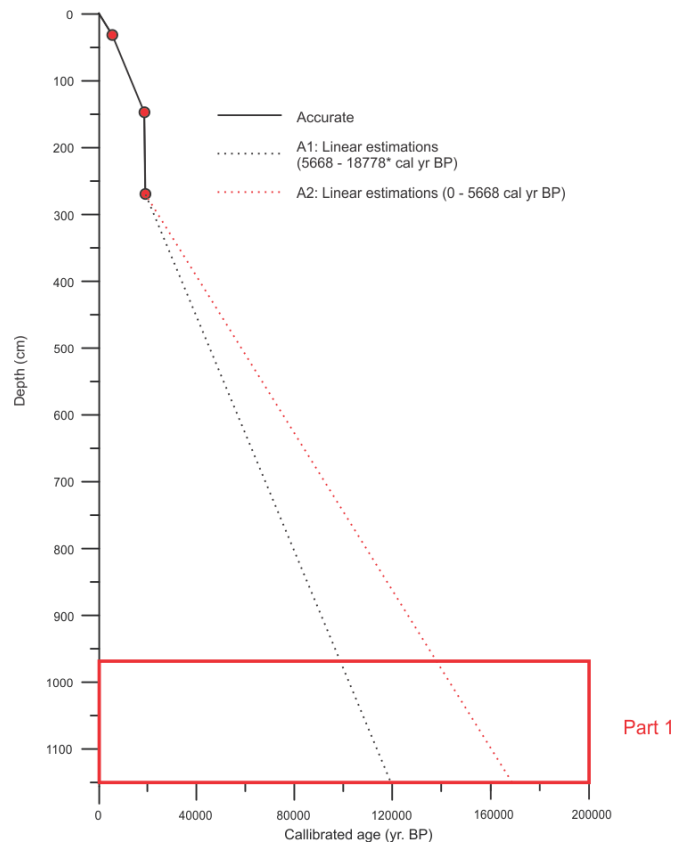


Figure 5.1.1.1: Sedimentation rates and age model of MD992301 based on calibrated years BP. The red box indicates Part 1.

Unit	Interval (cm)	A1: Age (cal. yr. BP)	A2: Age (cal. yr. BP)
<b>Unit 3</b>	999-961	~ 98,000 - ~102,000	~136,000 - ~142,000
<b>Unit 2</b>	1031-999	~102,000 - ~106,000	~142,000 - ~ 150,000
<b>Unit 1</b>	1156-1031	~106,000 - ~120,000	~150,000 - ~166,000

Table 5.1.1.1. Table showing the calibrated ages of the units comprising part 1.

### 5.1.1.2 Part 2

Part 2 comprises units 4 - 14 from 961 – 0 cm depth in the core. Sediments deposited within this interval has an assumed age between 0 – 136,000 cal yr BP (A1 – A2) (figure 5.1.1.2).

This part of the core is dominated by glaciomarine mud, interrupted by sandy turbidites, and the lowermost 18 cm the uppermost 52 cm is interpreted to have a hemipelagic origin.

Some dating could be established and an accurate sedimentation rate and age estimate could be modulated for the upper 273 cm (table 5.1.1.2).

From the tentative model a higher sedimentation rate is found in periods with glacial input, decreasing during interglacials. This indicates a significant drop in sediment input from a glacial to an interglacial environment. The calibrated  $^{14}\text{C}$ -ages obtained gives an average sedimentation rate of 20.2 cm/kyr within the dated interval, with a rate of 5.5 cm/kyr during Holocene, 8.8 cm/kyr during the interglacial periods, and 27.4 cm/kyr during LGM .

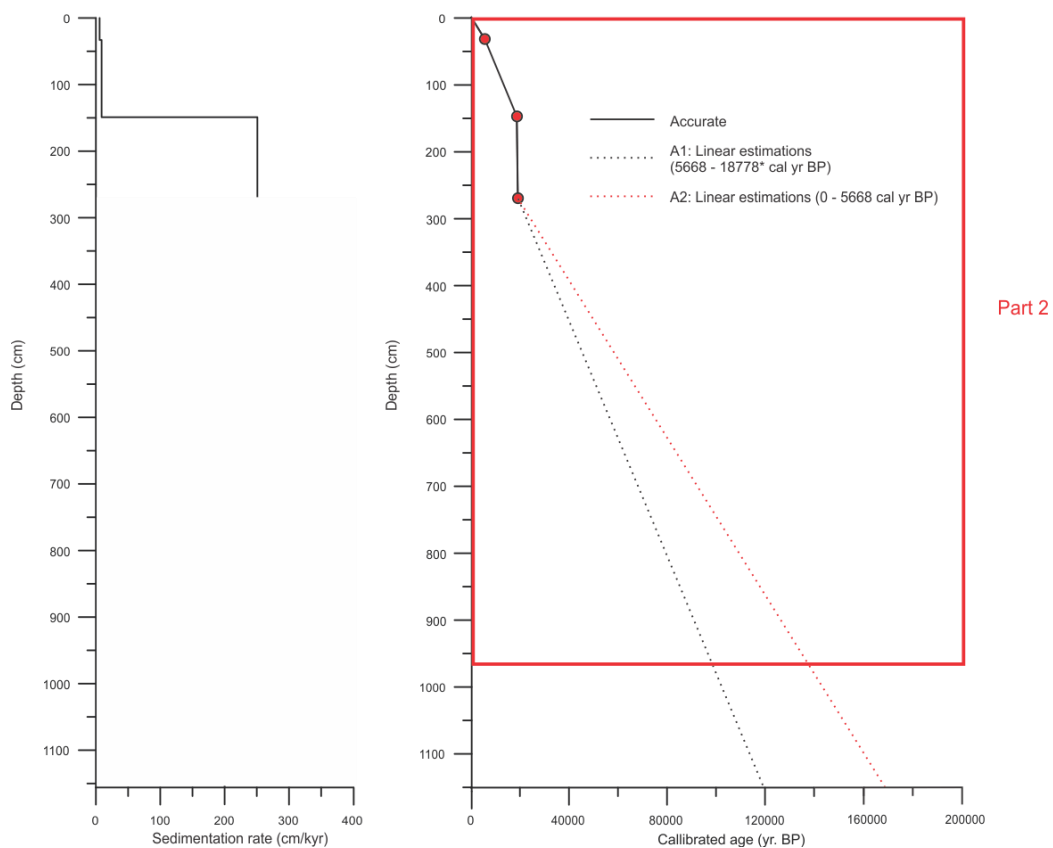


Figure 5.1.1.2: Sedimentation rates and age model of MD992301 based on calibrated years BP. The red box indicates part 2.

Unit	Interval (cm)	Sedimentation rate (cm/kyr)	A1: Age (cal. yr. BP)	A2: Age (cal. yr. BP)
Unit 14	52 - 0	5.5 cm/kyr	0 – ~ 6,000	0 – ~ 6,000
Unit 13	148 - 52	8.8 cm/kyr	~ 6,000 – 18,788*	~ 6,000 – 18,788*
Unit 12	201 - 148	8.8 cm/kyr	18,788* - ~19,278	18,788* - ~19,278
Unit 11	271 - 201	-	~19,278 – 19,278	~19,278 – 19,278
Unit 10	462 - 271	-	19,278 – ~ 42,000	19,278 - ~ 54,000
Unit 9	484 - 462	-	~42,000 - ~44,000	~54,000 - ~ 56,000
Unit 8	697 - 484	-	~ 44,000 - ~68,000	~56,000 - ~ 92,000
Unit 7	776 - 697	-	~68,000 - ~ 78,000	~92,000 - ~ 106,000
Unit 6	937 - 776	-	~78,000 - ~ 94,000	~106,000 - ~ 132,000
Unit 5	943 - 937	-	~94,000 - ~ 96,000	~132,000 - ~ 134,000
Unit 4	961 - 943	-	~ 96,000 - ~ 98,000	~ 134,000 - ~136,000

Table 5.1.1.2. Table showing the sedimentation rate and the given calibrated age of the units comprising part 2. (\* = uncertain due to small amount of datable material)

### 5.1.2 Sedimentation rate compared to other areas

The average linear sedimentation rate found in the upper 273 cm of the core can be compared to rates found in adjacent location on the Bear Island TMF. Previous work by Hald et al., (2001) has described the core M23385 (74°44.35'N 10°52.19'E), quite close to MD992301. They have estimated a Holocene sedimentation rate ~5 cm/kyr, while Laberg and Vorren (1995) proposed a rate of 15 cm/kyr for the proximal, debris flow dominated parts of the eastern Bear Island TMF. During interglacials with input of glacial marine mud the sedimentation rate is estimated to be ~7-10 cm/kyr (Hald et al., 2001), while Laberg and Vorren (1995) suggests an average of 13 cm/kyr from early Weichselian to Present (MIS 5d – 1). Due to an increased frequency of debris flows during glacials, the rate escalates to 124 cm/kyr during late Weichselian (MIS 2) (Laberg & Vorren, 1995). Both of the previous studies hence suggested a lower sedimentation rate during the interglacials, shifting to higher sediment input in glacial periods.

### 5.1.3 Summary

In summary, it is evident that the sedimentation rates in a glaciomarine environments vary greatly. The estimated average sedimentation rate the last ~20,000 years is estimated to be 20.2 cm/kyr, and 27.52 cm/kyr during Last Glacial Maximum (MIS 2). The rates can be compared to rates from other parts of the Bear Island TMF.

Three rates were established from the dated material. The uppermost 52 cm assumed to be deposited during Holocene has a sedimentation rate of 5.5 cm/kyr. In the interval from 52 – 201 cm the sedimentation rate is 8.8 cm/kyr. By extrapolating the rates calculated between 0-5668 cal yr BP and 5668 – 18,788 cal yr BP downcore, an estimated age model is presented. Based on this estimates, part 1 is assumed to contain material deposited from the Saalian glaciation towards the transition to the Eemian interglacial (136,000 – 166,000 cal yr BP), and part 1 is considered to contain material deposited during the Eemian interglacial, the Weichselian glaciation and Holocene (0 – 136,000 cal yr BP).

Hald et al., (2001) have previously dated the interval from MIS 5e to Present, and estimated a sedimentation rate ranging between 7-10 during the interglacial and 5 cm/kyr during Holocene. By comparing the rates found in their study to MD992301, the rates can be compared (5.5 cm/kyr during Holocene and 8.8 cm/kyr during interglacials). Due to strong similarities to the sedimentation rates suggested by Hald et al., (2001) it is possible to assume that the suggested age model for MD992301 is representative for the different units through the core. Based on the tentative age model, the age of the different units could be estimated due to few dated samples. Part 1 of the core is anticipated to be between ~136,000 – ~166,000 cal yr BP corresponding to the Saalian glaciation towards the Eemian interglacial. While part 2 is assumed to contain material from 0 – 136,000 cal yr BP deposited from the Eemian interglacial towards Present.

## 5.2 Paleoenvironment during deposition of MD992301 (0 - ~166,000 cal yr BP)

To make the further interpretation of the paleoenvironment the subdivision into two parts is kept based on lithology, physical elements and geochemical values. The division of the cores is set past and post deposition of hemipelagic and glaciomarine mud, in the transition from the Saalian glaciation to the Eemian interglaciation. In the following subchapters the paleoenvironment during deposition of the two different parts are going to be addressed separately, starting with the oldest deposits within part 1 (figure 5.2a).

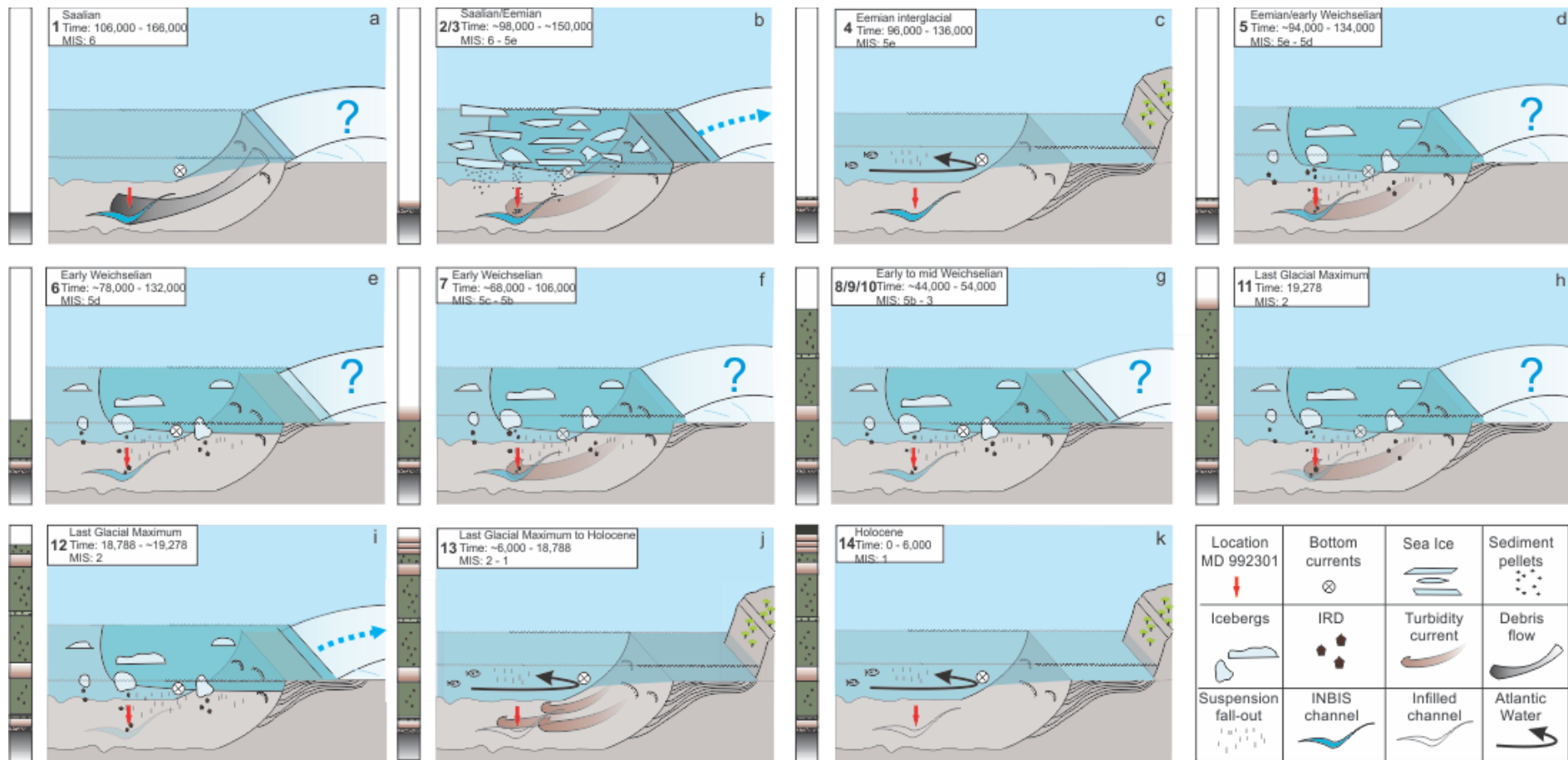


Figure 5.2a: Schematic overview of the main sedimentary processes and paleoenvironment in the southwestern Barents Sea from the Saalian glaciation to present. The sediment core from this study are indicated.

### 5.2.1 Part 1

Part 1 is thought to represent sediments deposited between ~136,000 - ~166,000 cal yr BP. The interval are dominated by various mass-flow deposits and sediment pellets. In the following subchapters the paleoenvironment of the three units comprising part 1 are going to be discussed.

#### 5.2.1.1 Massive, muddy debris flow diamicton (unit 1)

A massive diamicton is found at the base of the core. It is estimated to have been deposited somewhere between ~106,000 –166,000 cal. yr. BP (A1 – A2) assuming a linear age model, corresponding to the Saalian glaciation or of early Weichselian age. During periods of full-scale glaciations in the Barents Sea, glacial sediments were temporary deposited on the upper slope, where the rapid deposition lead to an unstable, oversteepened accumulation with buildup of excess pore pressure. When triggered large debris flows started moving downslope as described in chapter 2.6.4.3 and 4.2.3 (Laberg & Vorren, 1995, 1996a; Piper et al., 1999). The magnetic susceptibility of the sediments within unit 1 shows a near constant value, typical for sediments mixed during deposition of mass flows (Jessen et al., 2010).

The XRF data shows an increase in Silicon (Si/sum), Sulfur (S/sum) and in the relationship between Strontium/Calcium (Sr/Ca) indicating a higher content of organic debris, as Sulfur often is enriched in organic material. The increase in Silicon indicates a terrigenous origin, while an enhancement in Strontium indicates a shallow marine environment (Croudace et al., 2006; Rothwell et al., 2006). Unit 1 is thus assumed to have a terrigenous/shallow marine origin enriched in organic material, deposited by glaciers on the outer continental shelf and redeposited as a debris flow. The genesis of the flow is anticipated to have originated from either the Bear Island TMF, Storfjorden TMF of the Kveithola Trough at the upper continental slope/outer continental shelf. Each of the lobes represents a local, almost instantaneous depositional event (Solheim et al., 1998).

Previous studies states that the area has experienced several episodes of debris flow deposition (Sættem et al., 1992; Poole et al., 1994; Vorren & Laberg, 1996; Vorren et al., 1998; Jessen et al., 2010), describing them as “dark diamicton facies” and “massive dark grey diamicton”. Some of these debris lobes are identified in the swath bathymetry as described in chapter 4.2 (figure 4.2.1b and 4.2.1c). The identified lobes are assumed to been deposited during Late Weichselian (LGM) and shows a partial infill of the eastern parts of the INBIS

channel. There are also clear similarities with the unit found within MD992301 and glacial diamicton described by Laberg and Vorren (1995), based on the water content (between 19 – 30 % with an increase to 30 – 35% up the unit). Due to such similar characteristics unit 1 is interpreted as an ancient glacial debris flow deposited during full-extent of the Saalian Ice Sheet ~106,000 – 166,000 cal yr BP ago (figure 5.2a: a).

#### 5.2.1.2 Laminated sediment pellets (unit 2)

Laminated sediment pellets are found in the interval between 1031 - 999 cm. By using the linear age model for MD992301 the assumed age of the deposits is estimated to be between ~102,000 - 150,000 cal. yr. BP (A1 – A2) (table 5.1.1.1). This time period corresponds to the Saalian period or Early Weichselian.

Sediment pellets are previously described by Goldschmidt et al., (1992) and Henrich et al., (1989) from the Arctic Ocean and the Norwegian-Greenland Sea. The pellets formation are described in detail in chapter 2.6.4.6, where the sediment aggregates are formed into pellets by several freeze/thaw cycles in cryconite holes within sediment laden sea ice/icebergs (figure 2.6.4.6). The presence of sediment pellets within the core hence indicates a period when sea ice and/or iceberg contributed as an important sedimentary process.

The XRF data within the unit indicates an increase in Sulfur, Manganese and Strontium/Calcium. As described above, an increase in these parameters indicates shallow marine/terrigenous deposit enriched in organic material. The interlayered sand is assumed to be related to a different process. Two possible explanations of the sand are proposed by Svindland and Vorren (2002) and Vorren et al., (1998): 1) Winnowing (selective removal of finer grains from the sediment in a flow (Nichols, 2009)), and 2) the sand is a part of an ongoing turbidite current interrupted with sediment pellets deposited by sea ice/icebergs. However, due to the decrease in the strength of the ocean current during glaciations, similarities in the properties measured and the lower erosional boundary, we assume that the sand within unit 3 most likely has a turbidity origin.

Previous work by Knies and Vogt (2003) has interpreted a larger contribution of meltwater in the transition between MIS 5/6 (Saalian to Eemian) at approximately 130,000 years ago (Mangerud et al., 1996). The increased flux of the fresh meltwater is thought to reassemble the collapse of the large Saalian Ice Sheet where the contribution of meltwater promoted freshening of the Norwegian Sea surface. This may have initiated an increased sea ice

formation (Knies & Vogt, 2003). Unit 2 is hence thought to be deposited in a time during large input of freshening meltwater, contributing to the formation of sea ice. Such conditions may have been present already in a later stage of the Saalian glaciation in the transition to the Eemian interglacial (figure 5.2a: b)

#### 5.2.1.3 Sandy turbidite (unit 3)

From ~98,000 - ~142,000 cal. yr. BP (A1-A2) (assuming a linear age model), unit 3 is interpreted to be a sandy turbidite. The age model provides an age estimate between Saalian (MIS 6) to Early Weichselian (MIS 5d) for this period. Within this interval the Barents Sea is suggested to have experienced full-scale glaciation, depositing enormous amounts of material on the outer shelf in the region, before the material was redeposited as a sandy turbidite in the cored location. The turbidite is thought to originate from cold bottom water and brine rejection, or from transformation of mass-wasting events e.g. parts of debris flows.

The XRF data shows an increase in Sulfur and Strontium/Calcium, indicating an origin from shallow marine deposits with relatively high organic content (Rothwell et al., 2006).

The unit is believed to have originated from either the northern Bear Island TMF, the southern Storfjorden TMF, or the Kveithola Trough. Due to similar characteristics as seen in unit 2, the sandy turbidite is assumed to be deposited in the end of the Saalian glaciation during full-scale glaciation (figure 5.2a: b).

#### 5.2.1.4 Summary part 1

The depositional environment for part 1 is interpreted to represent a glacial environment, with the Barents Sea Ice Sheet extending all the way out to the outer shelf. In this period sea ice conditions characterized the Norwegian Sea (figure 5.2a: b). Due to the lack of datings from this part of the core, it is hard to tell exactly which glaciation the deposits represents. However, based on our results and the tentative age model compared to previous works in the area, a Saalian age is favored.

Reconstructions based on sediment cores including studies of IRD by Svendsen et al., (2004), show that the Saalian ice sheet was the largest ice sheet in Northern Eurasia the last 200,000 years BP, which is supported by Knies et al., (2000; 2002) who suggested maximum extent during marine isotope stages 6 and 4.

When the large Saalian ice sheet started to retreat, huge amounts of glacial meltwater was released into the ocean, promoting a freshening of the ocean surface water (Knies & Vogt, 2003). The freshening initiated the formation of an extensive sea ice cover, unit 2 thought to be the depositional environment during deposition of unit 2. However, it is also possible that they have a fecal origin or have been deposited from icebergs (Goldschmidt et al., 1992). Sediment pellets previously described from the Nansen Basin and Norwegian Sea are however interpreted to be deposited by the overturning of icebergs (Goldschmidt et al., 1992). The pellets described in this region is composed by grains of a larger size, and the pellets has a lower degree of rounding than seen in the pellets extracted from the studied core. Due to a larger content of finer grained material within Md992301, the high biogenic content and the roundness of the clasts, the sediment pellets found within the core is assumed to have a sea ice origin. Based on the estimated age model presented in chapter 5.1.1 an assumed age of 102,000 - 150,000 cal yr BP (A1 – A2) is proposed.

The uppermost unit in part 1, unit 3, comprises a sandy turbidite. As previously mentioned, turbidites are thought to be initiated when the ice reached the shelf break, which in this case may be the Saalian ice sheet (MIS 6) or Early Weichselian (MIS 5d) when it was once again a re-advance of the Barents Sea Ice Sheet. However, due to the interlayering with the sediment pellets, a Saalian age of the deposits are favored.

## 5.2.2 Part 2

In the following subchapters the paleoenvironment during deposition of the different units comprising part 2 are going to be presented, starting with the oldest deposits within part 2.

### 5.2.2.1 Homogenous massive hemipelagic mud (unit 4 and 14)

The depositional environment of the homogenous massive mud is interpreted as hemipelagic mud. It contains little to no IRD, indicating that the deposition from ice rafts is negligible compared to the input of suspended material from hemipelagic settling. This depositional environment is favorable in interglacial periods (Nichols, 2009) in an open water environment (figure 5.2a: c and k).

The XRF data shows no clear changes in the geochemical elements besides a small increase in Silicon and Strontium/Calcium in unit 4 and an increase in Calcium, Strontium/Calcium and Zirconium/Rubidium (note the disturbance, as mentioned in chapter 4.4.14).

The increase in Strontium/Calcium requires a shallow-water source, and Zirconium/Rubidium is often enhanced in turbidites, but are assumed to be enhanced due to disturbance and mixing on the core top.

#### 5.2.2.2 Sandy turbidites (unit 5, 7, 11 and 13)

The lowermost turbidite (unit 5) has an age estimate of 96,000 – 136,000 cal yr BP and is assumed to be deposited during the transition from the Eemian interglacial to Early Weichselian. At 697 – 776 cm core depth in unit 7 the second turbidite is interpreted. The estimated age of the sequence is between 68,000 – 106,000 cal yr BP and is assumed to be deposited sometime during early Weichselian (MIS 5c-5b). The largest turbidite identified in MD992301 is located at 201 – 271 cm core depth in unit 11. This deposit is assumed to have an age of ~19,278 cal yr BP, corresponding to sometime within Late Weichselian (MIS 2). The smaller turbidites present in unit 13 from 52 – 148 cm core depth is thought to have an age between 6,000 – 18,788 cal yr BP, corresponding to the transitional phase from Last Glacial Maximum to Holocene. The turbidites found within MD992301 in part 2 are made up by silty sand with a grain size ranging between fine sand to very fine sand.

In X-ray it is clear that the different turbidites do not contain any ice derived material (IRD). Both above and below the sandy turbidites sequences in unit 7 and 11 IRD are identified, which may indicate that input of IRD was present but may be masked or interrupted by the rapid deposition of the turbidites. The interlayered glaciomarine mud also gives indications that the turbidites were active during full-scale glaciations on the Barents Sea Shelf (Vorren et al., 1998).

As previously mentioned, the different turbidite sections are thought to have been transported through the INBIS channel. The currents use the channel as a conduit from the area of initiation towards the deep sea. Turbidite deposits are hence assumed to represent periods of activity within the channel. During transportation within the channel confinement the turbidity currents had a smaller interface to the ambient water, leaving the density high until the flow became unconfined at greater depths (Fohrmann et al., 2001), depositing material in the overbank area.

Mangerud & Svendsen (1992) has previously interpreted four re-advances of the Barents Sea Ice sheet, which corresponds to MIS 5d, 5b, 4 and 2. By comparing this to the deposition of

turbidites within part 2, it shows that only three of these re-advances out to the shelf edge is marked within MD992301: MIS 5d (unit 5), MIS 5b (unit 7) and MIS 2 (unit 11) (figure 5.2 d, f and h). There is however possible that there was turbidites present during MIS 4 (59,000 – 74,000 cal yr BP), but that the mass-transport deposits from this interval didn't materialize within the core.

In the XRF data (figure 4.4c) it is clear that the turbidites deposited has a different mineralogy compared to the surrounding glaciomarine mud. Each individual turbidite has its own characteristic composition, indicating changes in origin and composition of the provenance area. This also indicates a possible shift between the northern Bear Island Trough Mouth Fan, the Storfjorden Trough Mouth Fan and the Kveithola Trough as source area. By comparing the XRF data, the turbidites deposited within part 2 are assumed to have a different origin than the turbidite represented within part 1. While there was an increase in Strontium/Calcium and a decrease in Silicon within part 1, the turbidites deposited within part 2 shows an enrichment in Silicon, Zirconium, Iron (unit 7), Zirconium/ Rubidium, and Strontium/Calcium (figure 4.4c). An increased amount of Silicon indicates a terrigenous material input, and a high value of Zirconium and Zirconium/Rubidium is often enhanced in turbidite bases. The relationship between Strontium/Calcium indicates a shallow marine provenance. The increase in Iron may be due to redox-related diagenesis, seen in oxic and formerly oxic parts of sediment (Croudace et al., 2006; Rothwell et al., 2006).

Turbidity currents are thought to either have been initiated by the initiation of density currents from brine rejection or developed from other mass-wasting events such as e.g. debris flows (chapter 2.6.4.4). Due to an interpretation of full-scale glaciation both is likely (Alley et al., 1989; Hooke & Elverhøi, 1996), however, the huge amounts of sediments deposited in glacial periods, a mass-wasting origin is favored for unit 5, 7 and 11, while initiation by density currents are the assumed origin for unit 13 (figure 5.2a: d, f, h and j).

#### 5.2.2.3 Glaciomarine mud (unit 6, 8, 9, 10 and 12)

The second part is dominated by glaciomarine mud which occur in units 6, 8, 9, 10 and 12. The composition of the mud shows a fairly similar trend throughout, with no distinct marks within the XRF data besides an increase in the content of Manganese for unit 9. This facies is hence divided into two sub-facies: one comprising unit 6, 8, 10 and 12 and one with unit 9

(figure 5.2.2.3). In the uppermost 273 cm, the glaciomarine mud is interlayered with a higher frequency of sandy deposits thought to represent the Last Glacial Maximum.

The clast found is thought to be deposited by sea ice/iceberg calved as IRD from the Barents Sea Ice Sheet during interstadial periods (described in chapter 2.6.4.5). Interpretation done of the IRD deposited further north on the Barents Sea margin have suggested a northern and western Norway origin of the clasts (Jessen et al., 2010). The interpretation of the paleoceanography done by Hebbeln et al., (1998) in figure 2.3.2a supports this, where the IRD is thought to be derived from mainland Norway and Svalbard (figure 2.3.2a: c, g, h and i). They have suggested a similar ocean circulation pattern as Present during the deposition. However, they also suggest main input from Greenland during MIS 5c and 5a (figure 2.3.2a: d and f). Within the glaciomarine mud, some intervals remains clast free. This may indicate that the abundance of IRD and icebergs may have been limited, alternatively that this intervals or some of them represents muddy (distal) turbidites. The intervals without presence of clasts are:

- 281 – 367 cm (24,000 – 37,000 cal yr BP),
- 502 – 623 cm (44,000 – 80,000 cal yr BP),
- 776 – 822 cm (78,000 – 114,000 cal yr BP),
- 855 - 942 cm (84,000 – 132,000 cal yr BP).

Previous work have interpreted the grayish and olive colored mud as glaciomarine, deposited from glacial derived sediment-laden meltwater plumes (Solheim et al., 1990; Laberg & Vorren, 1995; Gataullin et al., 2001). The sediments carried in suspension may be deposited within a few kilometers from the meltwater flux, while smaller local accumulations may represent shorter and/or smaller meltwater outlets (Pfirman et al., 1989). Variations in the amount of material may come from still stand but can also be related to temporal and spatial variations in the sediment and meltwater supply. Due to depositions related to the Bear Island Trough, a change in the main meltwater input is thus unlikely, since the main outlets in the region are located within the trough (figure 5.2: e, g and i).

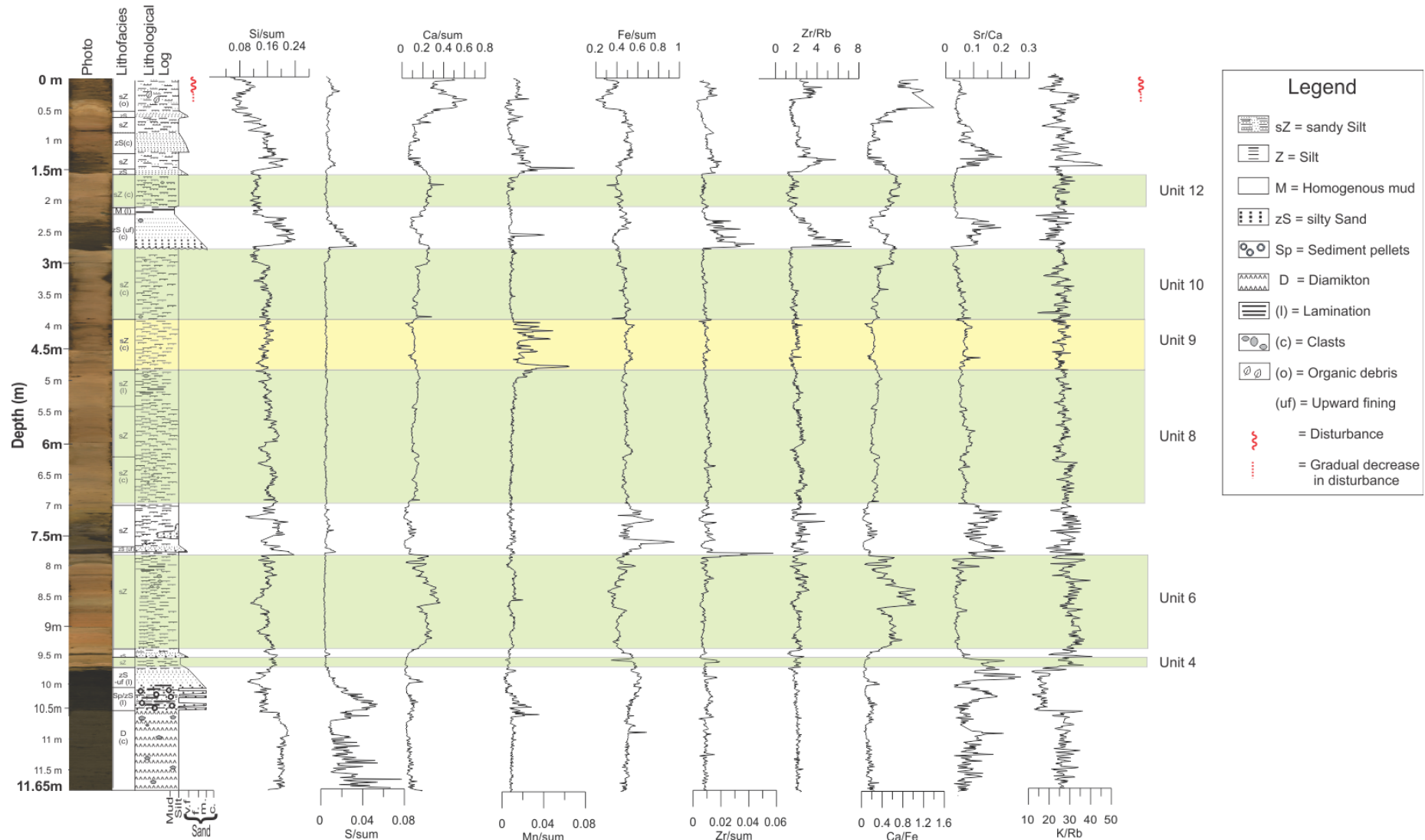


Figure 5.2.2.3: The units comprising glaciomarine mud within part 2. The change in highlight indicates changes in genesis.

#### 5.2.2.4 Summary part 2

Based on the characteristics of the sediment deposited within part 2 a glaciomarine depositional environment is favored except for the lowermost 18 cm and the uppermost 63 cm. In a deep sea setting, clasts observed are assumed to have been transported by sea ice and/or icebergs. Since clasts are present in large proportions of the cored interval, sea ice and/or icebergs must have been present for longer durations, which also is indicated by the paleoceanography model suggested by Hebbeln et al., (1998). In their model, clasts are suggested to be deposited frequently from the Saalian to LGM (figure 2.3.2a: b-i). These large intervals of glaciomarine mud with scattered clasts are interlayered with several sandy turbidites, increasing in frequency the uppermost 273 cm. The turbidites deposited are interpreted to have used the upper slope gullies and the INBIS channel as a conduit towards the deep sea. However, the turbidites present within MD992301 must have been large enough to spill over the channel confinement to be deposited in the overbank area where the core is located. Unit 4 from 961 – 943 cm, and unit 14 in the uppermost ~52 cm is dominated by interglacial sediments, deposited in an open marine environment.

In the XRF data, there is a clear change in geochemical composition from the glaciomarine mud and the different turbidites. This may indicate a change in the origin of the turbidites derived from the Bear Island TMF, the Kveithola Trough and the Storfjorden TMF. The change in origin of the turbidites deposited, hence indicates sediments deposited from different troughs and ice streams, which entraps material from different provenances on the shelf and surrounding continental areas.

### 5.3 Glacial/interglacial history and paleoenvironment of the Barents Sea

In the following subchapters the glacial/interglacial history and sedimentary paleoenvironment in the southwestern Barents Sea throughout the cored interval will be discussed. The reconstruction is based on lithological changes, sedimentation rates, IRD content, assumed age model, physical parameters and comparison to previously published data. A schematic overview of the main sedimentary process and paleoenvironment at the location of MD992301 is given in figure 5.2a.

The division into six main time periods is based on the boundaries in lithology, measured physical properties and geochemical properties and previous work describing the paleoenvironment of the study area. The dates of the boundaries were approximated using an age model assuming constant sediment accumulation rates between the provided radiocarbon dates. The oldest sediments deposited within MD992301 has a suggested age of 106,000 – 166,000 cal yr BP, suggesting that the cored sediments were deposited during the last 166,000 years from the Saalian glaciation to Present.

#### 5.3.1 Saalian (240,000 – 130,000: MIS 6)

Sediments deposited during Saalian are represented in the lowermost parts (1156-1031 cm) in MD992301 (figure 5.2: a and b and figure 5.3.2). Since there was no foraminifera able to be dated within this interval, an estimated age were given, assuming a linear accumulation rate. The applied method gave an age of 166,000 – 130,000 cal yr BP. No studies have previously described such depositions during the Saalian glaciation. In addition, large proportion of the Saalian depositions is eroded and removed during the Weichselian ice configuration, leading to restrictions in the amount of material leaving the knowledge of this glaciation sparse.

In the Barents Sea the Saalian period marks the second Last Glacial Maximum in the area (Mangerud et al., 1998). The period is characterized by a massive ice sheet covering the whole Barents Sea margin. The major glaciations led to a pronounced eustatic sea level fall due to the entrapment of precipitation into the ice sheet (Rabineau et al., 2006) and left huge deposits of subglacial till along the margin (Miller et al., 1989), which was later redeposited by mass-wasting events. During Saalian, the income of the different water masses were sparse, with only Arctic and polar water masses, leaving most of the ocean with a perennial ice cover with some areas that were seasonally ice free (Hebbeln et al., 1998) (figure 2.3.2a: d).

The first unit deposited during Saalian is characterized by a massive dark grey diamicton facies interpreted as the top of an ancient debris flow, and shows no inner bioturbation. The lack of bioturbation is interpreted to be that the diamicton represents the upper parts of a debris flow lobe, deposited with a high sedimentation rate, resulting in an unfavorable environment for microfauna (Gingras et al., 2015).

In the end of the Saalian glaciation the ice sheet started to retreat, releasing large amounts of fresh water into the ocean. The freshening of the ocean promoted the buildup of large covers of sea ice (Knies & Vogt, 2003). Unit 2 and 3 is hence assumed to be deposited within the transition from MIS 6 to 5e, before the total retreat of the Saalian Ice Sheet. However, due to the type of sediments deposited, it is most likely that the sediment pellets and turbidite is deposited during the end of the Saalian glaciation.

### 5.3.2 Eemian (130,000 – 117,000: MIS 5e)

The Eemian period is based on the age model presented in chapter 5.1. Within this interval there were no foraminifera present, and the age of the deposits is therefore only tentatively estimated. By applying this method, the age of the interval is estimated to be 130,000 – 117,000 cal yr BP assuming a linear accumulation rate. The unit is characterized hemipelagic sediments assumed to be deposited in an open water environment (figure 5.2a: c).

Within the Eemian period (130,000 – 117,000 cal yr. BP) there were no longer an ice cover in the Barents sea and Scandinavia (Mangerud, 2004; Vorren & Mangerud, 2008). The depositional environment is characterized by a warmer climate and an increased heat flux at the sea surface temperature, warmer than Holocene and present (Kellogg, 1980; Mangerud et al., 1981; Raukas, 1991). Hebbeln et al., (1998) has interpreted that there was an income of temperate Atlantic water in this period, contributing to the already present Arctic and polar water masses (figure 2.3.2a: d). The retreat of the regional ice sheet lead to an subsequent glacio-isostatic uplift during the Eemian interglacial (Miller et al., 1989). Interpreted marine sediments deposited during the Eemian interglacial hence suggests a water depth similar to early Holocene (Mangerud et al., 1998), with deposition of hemipelagic material.

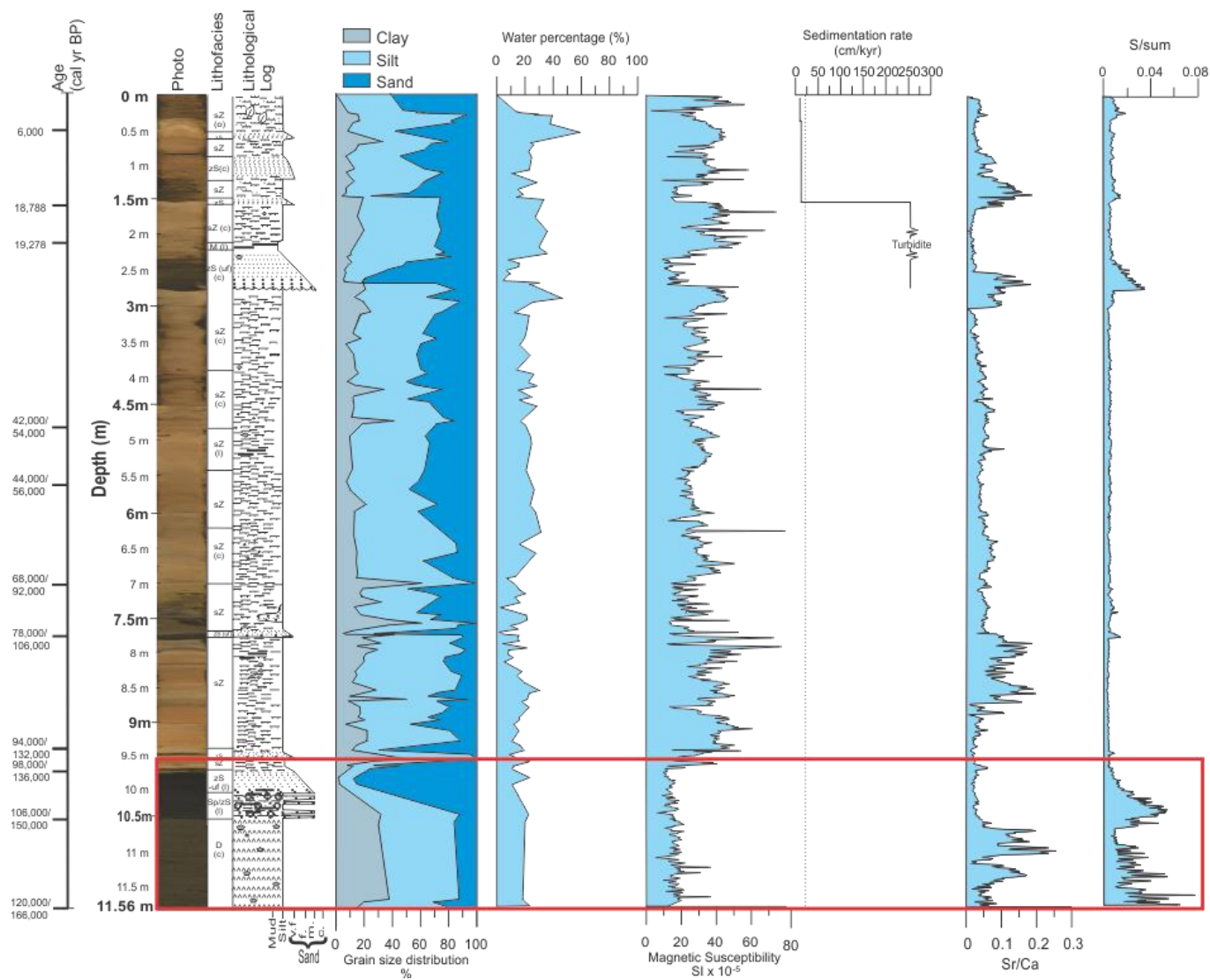


Figure 5.3.2: Lithological log, grain-size distribution, measured physical properties, sedimentation rate and element geochemistry for MD992301 plotted against depth. Radiocarbon age is given in calibrated years BP. A linear age model is presented to the left. The inferred intervals of the Saalian glaciation to the Eemian interglacial is marked with red box.

### 5.3.3 Early (117,000 – 74,000: MIS 5d-5a) and Mid-Weichsel (74,000 – 24,000: MIS 4-3)

After the Eemian interglacial the climate cooled again, starting in the transition to the Weichselian glacial period. The interval from 961 – 484 cm is thought to reassemble deposits from Early and Mid-Weichselian (figure 5.3.3). Within this interval several smaller readvances and retreats of the Barents Sea Ice Sheet and sea ice extension has led to the deposition of large amounts of material (figure 5.2a: d – g). The estimated age for the units deposited within this interval is set to be between 24,000 - 117,000 cal yr BP. Neither within this interval is it seen any signs of bioturbation. The reason for this may be due to a colder climate, leading to restrictions in the income of Atlantic water (figure 2.3.2a: g and h) causing unfavorable bottom conditions or rapid sedimentation rate. Due to a relatively low sedimentation rate within this interval (~8.8 cm/kyr) the main restriction is assumed to be a colder climate and the increase in ice masses. Within MD992301 the deposits found within this period is dominated by glacial marine sedimentation, and a few sandy turbidites (unit 5 and 7).

During the Early (~117,000 – 74,000 cal. yr. BP) and Mid-Weichselian (~74,000 – 24,000 cal. yr. BP) the extent of the Barents Sea and Scandinavian Ice Sheet were significantly more restricted than during the Saalian and Late Weichselian (Andersen & Mangerud, 1990). The depositions of glacial till was restricted to the Svalbard archipelago and northern Barents Sea (Mangerud et al., 1998). During the interstadials the ocean circulation pattern were restricted, with income of Arctic and Polar Water and smaller contributions of cold temperate Atlantic Water masses (figure 2.3.2a c-h) indicated by a low-diversity fauna on the Scandinavian mainland (Fronval & Jansen, 1997).

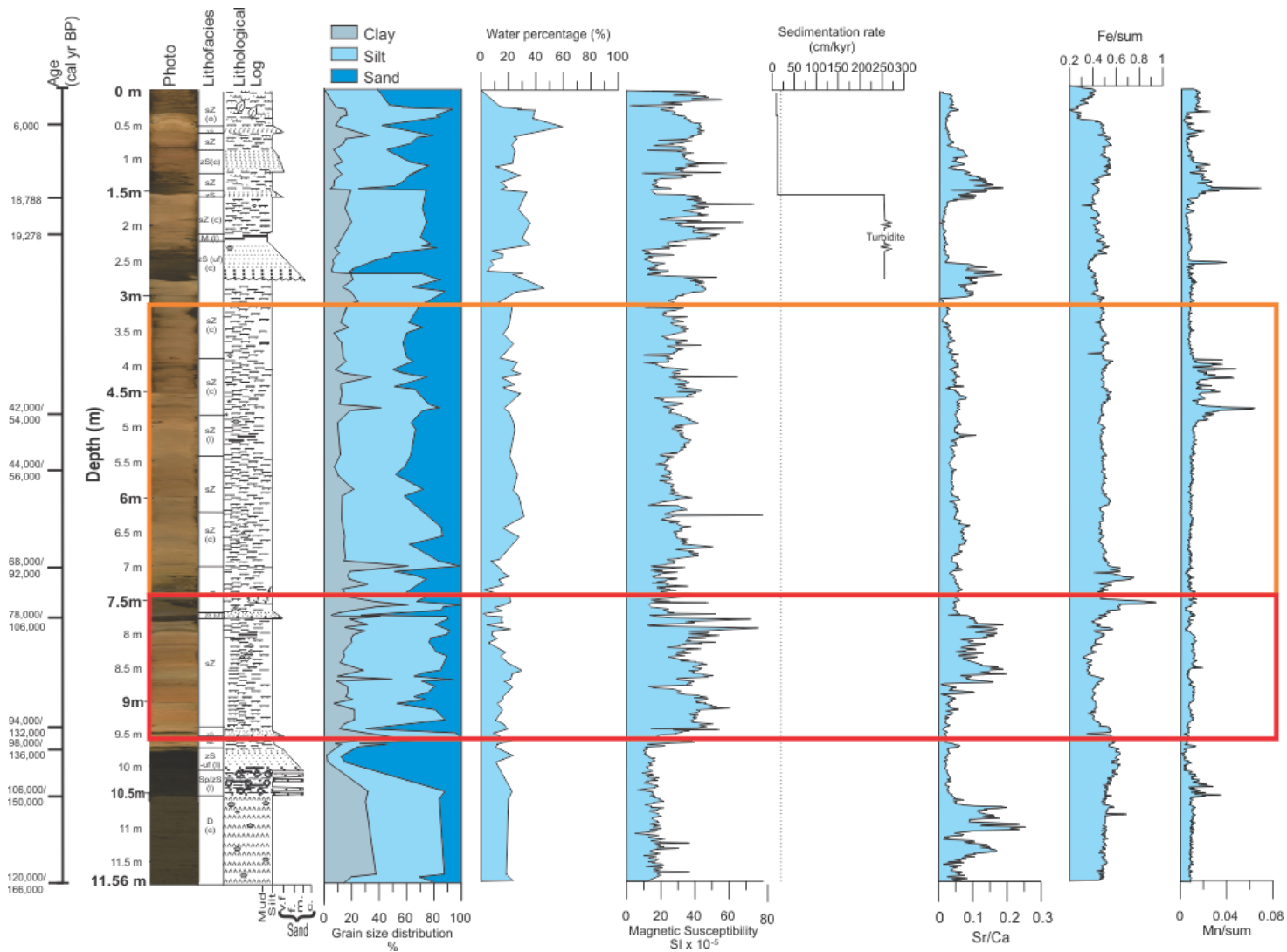


Figure 5.3.3: Lithological log, grain-size distribution, measured physical properties, sedimentation rate and element geochemistry for MD992301 plotted against depth. Radiocarbon age is given in calibrated years BP. A linear age model is presented to the left. The inferred intervals of Early Weichselian is marked with a red box, and Mid-Weichsel is marked with orange box.

#### 5.3.4 Late Weichsel: Last glacial Maxima (24,000 – 17,000: MIS 2)

The sediments deposited during Last Glacial Maximum is thought to include the sediments within the interval from ~98 - 290 cm (figure 5.3.4). Based on the age model given in chapter 5.1 the interval is assumed to contain material deposited between 17,000 – 24,000 cal yr BP. The accumulation rate through the interval has an average of 27.4 cm/kyr, dominated by a massive layer of graded sandy turbidite, overlain by glaciomarine mud and two smaller deposits of fine grained sand.

The renewed climatic cooling was initiated during the Late Weichselian (~25,000-17,000 cal. yr. BP), and marks the stage when the Barents Sea Ice Sheet reached the shelf edge for the last time. Several factors have been suggested for its onset, with fluctuating solar activity causing a prolonged minimum in sunspot activity and solar output being the main theory along with changes in the ocean circulation pattern of the Norwegian Greenland Sea (Benn & Evans, 1998; Hebbeln et al., 1998; Mangerud et al., 1998; Vorren & Mangerud, 2008). Within this period, the ice from the inland areas drained out onto the continental shelf with the main drainage route through the coast parallel troughs (Ottesen et al., 2005; Ottesen et al., 2008). By dating mass deposits on the Bear Island TMF two maximum sages are identified by Laberg & Vorren (1996) within this period 1) ~22,000 cal. yr. BP and 2) 17,500 cal. yr. BP. On the Barents Sea shelf, the Bear Island Trough where the main drainage conduit in the area, accumulating sediments in the trough mouth fans, while the cold based ice located on the banks remained passive (Andreassen et al., 2008; Winsborrow et al., 2010). During LGM there water masses in the Norwegian-Greenland Sea remained the same as in early- and mid-Weichel, dominated by Polar and Arctic Water (figure 2.3.2a: i). The cold water masses led to the formation of a perennial and seasonally sea ice cover (Hebbeln et al., 1998).

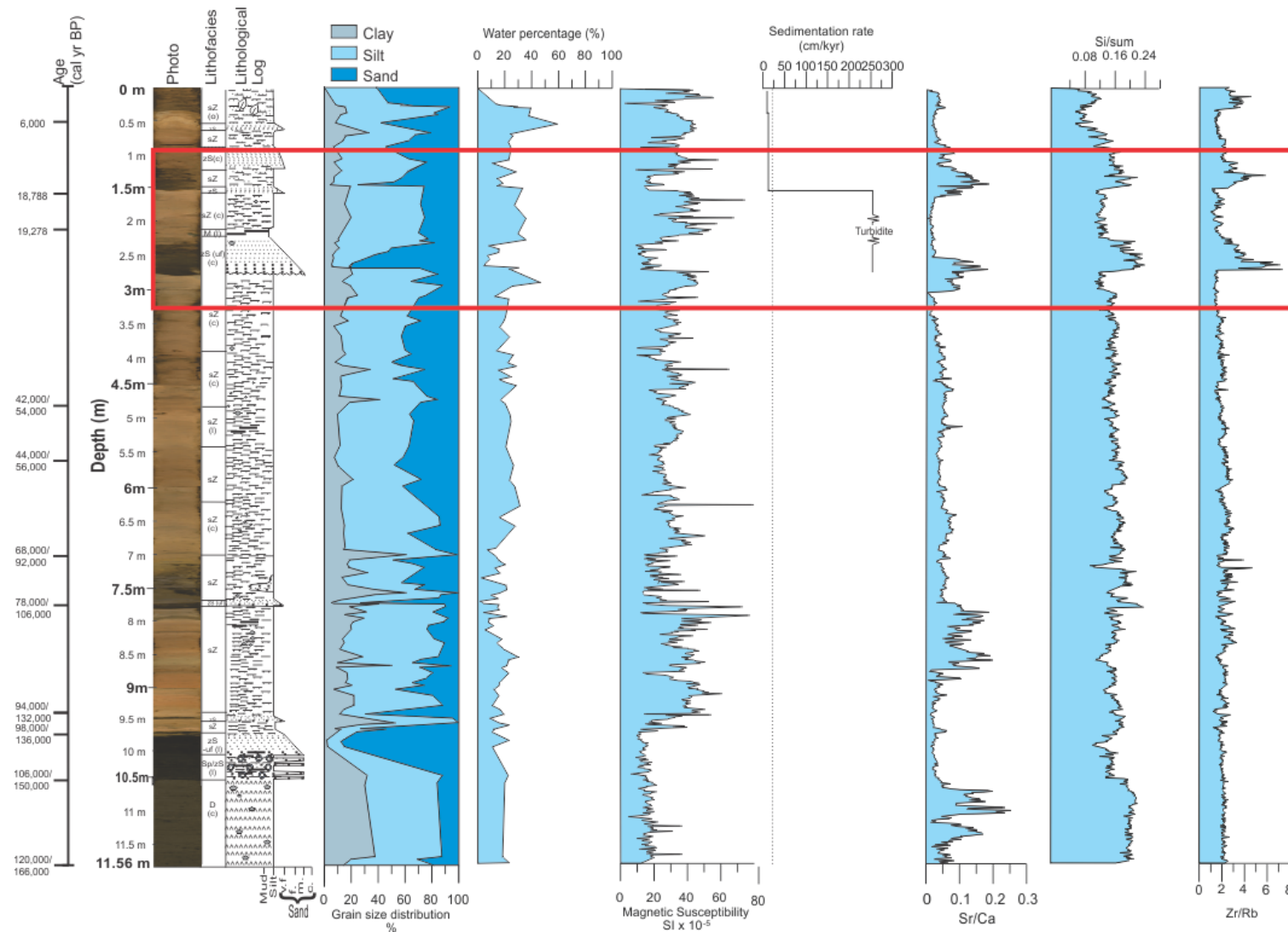


Figure 5.3.4: Lithological log, grain-size distribution, measured physical properties, sedimentation rate and element geochemistry for MD992301 plotted against depth. Radiocarbon age is given in calibrated years BP. A linear age model is presented to the left. The inferred intervals of Late Weichselian (LGM) is marked with red box.

### 5.3.5 Deglaciation (17,000 – 11,500 MIS 2/1)

Deposits from the last deglaciation in the Barents Sea is found from 62 – 98 cm (figure 5.3.5), and is dominated by sandy silt and clay without any signs of clasts. The deglaciation in the southwestern Barents Sea began around 17,000 cal. yr. BP with a significant retreat of the ice margin as described in chapter 2.5.4.

The glacial geomorphology indicates spatial and temporal variations in the ice dynamics, where there are evidences of both active ice streaming and frozen-bed conditions at both maximal glacial extent and during phases of deglaciation (Winsborrow et al., 2010).

The retreat was initiated within the troughs, where the ice streams were most sensitive to ocean warming and sea-level rise. In this manner the ice sheet would start to float as the deepest parts were retreated, causing calving (Benn & Evans, 1998). As the grounding line of the glacier retreated towards shallower areas, several ice-marginal features were deposited in e.g. the Bear Island Trough and along the slope (Solheim et al., 1990). In this phase, the large coast parallel troughs worked as drainage channels, fed by the tributary fjords on the mainland keeping the troughs on the shelf active (Vorren & Kristoffersen, 1986). The transition from a glaciomarine to a marine environment is estimated to be around 11,500 cal. yr. BP (Hald et al., 1989; Solheim et al., 1990), were there once again were income of warm and cold temperate Atlantic Water Masses (Hebbeln et al., 1998) (figure 2.3.2a: j).

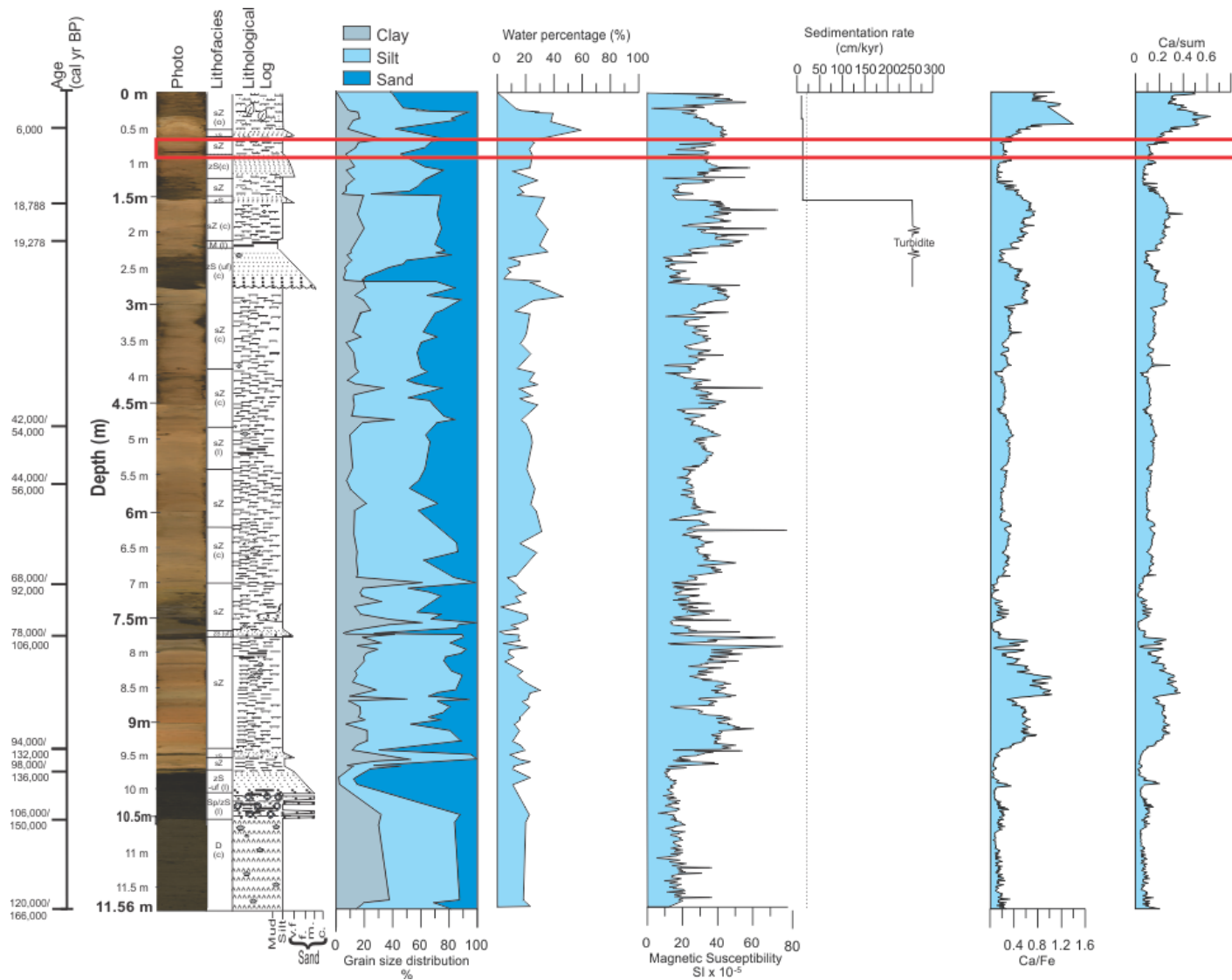


Figure 5.3.5: Lithological log, grain-size distribution, measured physical properties, sedimentation rate and element geochemistry for MD992301 plotted against depth. Radiocarbon age is given in calibrated years BP. A linear age model is presented to the left. The inferred intervals of the last deglaciation is marked with red box.

### 5.3.6 Holocene (11,500 – present: MIS 1)

Holocene are the second warmest period recorded in the Barents Sea region. After Last Glacial Maximum the temperature once again increased at the start of Holocene. The deposits from this period is generally sparse within MD992301 and includes only the uppermost 63 cm of the cored interval (figure 5.3.6). The sediments deposited shows an decrease in the number of IRD and the mineral content are more stable, reflecting a higher degree of ocean current transportation. Holocene sediments is found in the two uppermost units within Md992301, where unit 13 is from a transitional phase. The age of the interval is dated to 18,788 cal. yr. BP, where the shift to Holocene is assumed to be around 11,500 cal. yr. BP. The average with an average sedimentation rate for this period is estimated to be of 5.5 cm/kyr, where the main depositional processes is dominated by hemipelagic suspension fall out. The foraminiferal fauna in this interval shows a larger number of the benthic warm water species *Pyrgo williamsoni*, indicating stronger income of Atlantic water masses and increased bottom current activity. This is supported by Hebbeln et al., (1998) (figure 2.3.2a: j) which indicated ice free conditions in the region, and income of warm, nutrition rich, saline Atlantic Surface Water transported northward by the North Atlantic Surface Water.

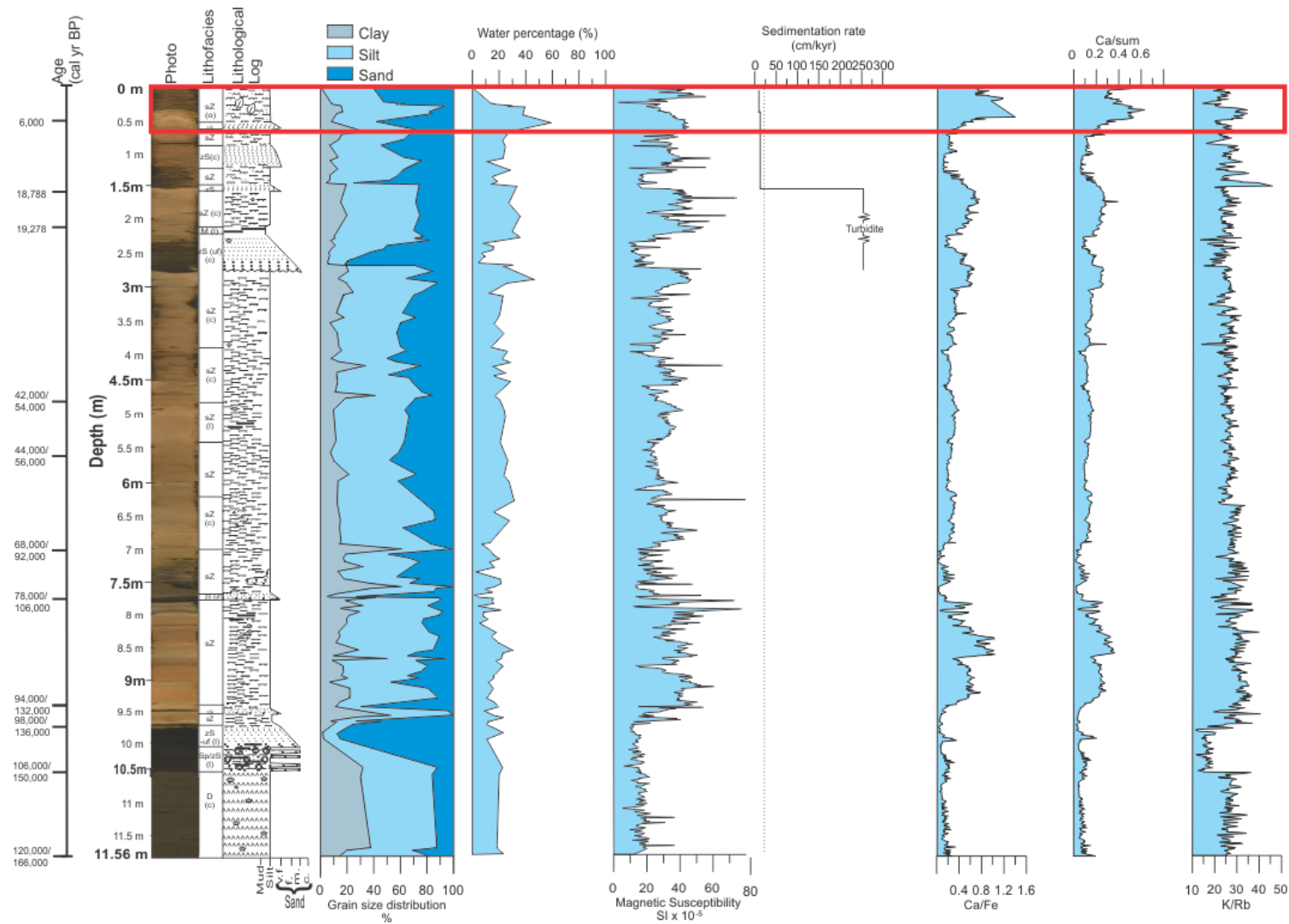


Figure 5.3.6: Lithological log, grain-size distribution, measured physical properties, sedimentation rate and element geochemistry for MD992301 plotted against depth. Radiocarbon age is given in calibrated years BP. A linear age model is presented to the left. The inferred intervals of Holocene is marked with red box.

## 5.4 Activity related to the INBIS channel

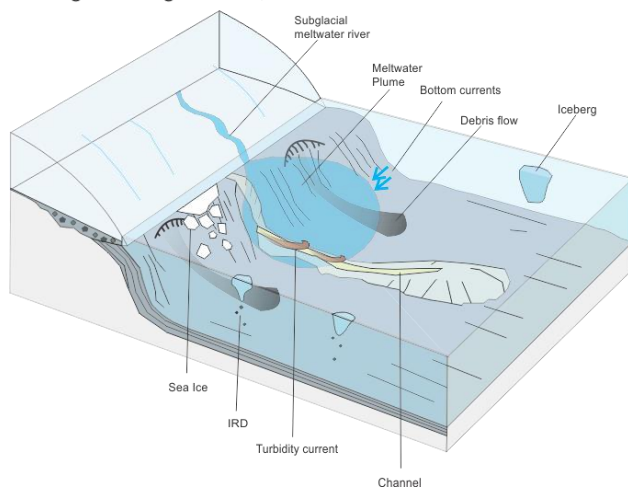
Submarine channels are known for being an important conduit for sediment transportation from the continental shelf towards the deep sea. Mass-transportation evolves from deformed subglacial sediments deposited at the ice edge during large-scale glaciation (Alley et al., 1989; Hooke & Elverhøi, 1996). When triggered a mass-flows are transported through the confinement of the channel it may evolve into a turbidity current (figure 5.4a).

The turbidites found within MD992301 is hence assumed to have been deposited from turbidity currents traveling down the channel, and marks periods of activity. It is therefore reasonable to believe that the INBIS channel were formed, and activated during episodes dominated by large-scale glaciations, which in this study is estimated to be in the following time intervals (figure 5.4b):

- from ~102,000-142,000 cal yr BP (unit 2 and 3), during the transition from the Saalian glaciation towards the Eemian interglacial,
- from ~94,000 – 134,000 cal yr BP (Unit 5),
- from ~68,000 – 106,000, during Early Weichselian (Unit 7), and,
- during Late Weichselian from 19,278 – 11,500 (unit 11)

In the bathymetry seen in figure 4.2.1 b and c the debris lobes of LGM age is interpreted to the east are assumed to cut of the channel. This is assumed to have resulted in restrictions of the domination of mass-flows through the channel, and infill over time. During Holocene the activity of the channel has hence been significantly reduced, as the sediment income has decreased.

A: Large-scale glaciation, active channel conditions



B: Interglacial, restricted activity within the channel (infill)

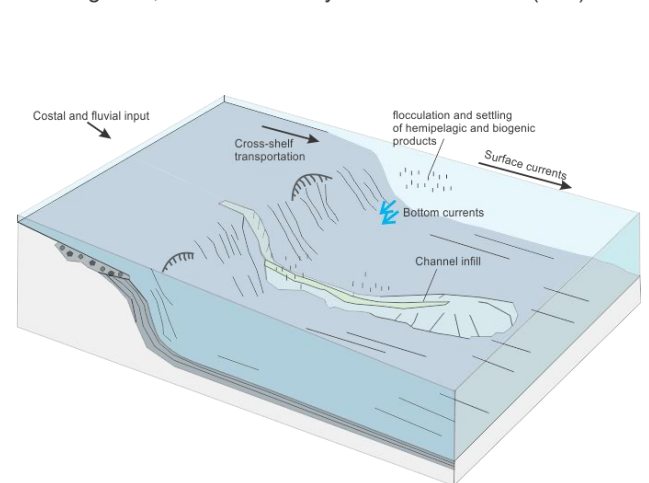


Figure 5.4a: Principal sketch showing the change in activity in the INBIS channel between glacial and interglacial conditions.





## 6. Summary and conclusion

The Calypso core MD992301 was acquired from the southern levee of the INBIS channel, located between the distal parts between the Bear Island TMF and the Storfjorden TMF. During this study the core has been analyzed, interpreted and correlated to a nearby core in order to investigate the origin of the cored sediment, the sedimentary processes involved and the paleoenvironment with focus on possible activity of the deep-sea channel.

- Based on swath bathymetry data, three main morphological features have been identified within the study area and the adjacent northern Bear Island TMF: upper slope gullies, debris flow lobes, and the INBIS channel with surrounding levees.
- Within MD992301 a total of 14 lithological units have been identified. The units represents mainly deposits within a glaciomarine environment or an open marine setting, and turbidites. The recovered units have probably been deposited from the Saalian glaciation up to the Present (~166,000 – 0 cal yr BP).

The dominating lithofacies of the glaciomarine deposits are sandy silt with scattered clasts larger than 2 mm (IRD), interlayered by sandy turbidites with a silty sand lithofacies. Sediment pellets has also been recovered, inferred to have been deposited during severe sea ice condition (~102,000 – 150,000 cal yr BP). In the open marine deposits the lithofacies identified varies between sandy silt, silt and very fine sand, without any content of clasts.

- The dominating sedimentary processes present within MD992301 is interpreted to have been suspension fall-out from glacial meltwater plumes entering the open ocean at the front of the Barents Sea Ice Sheet. The clasts are interpreted to have been transported and deposited by sea ice and/or icebergs. The glaciomarine mud is interrupted by episodically mass-transport deposits is inferred to been deposited during full-scale glaciation. These deposits are related to the development of oversteepened slopes due to high sediment supply and/or pushing of sediments at or near the grounding line of the ice sheet. The open marine material is interpreted to be deposited by hemipelagic sedimentation by organic rich- and skeletal debris.
- Mass-transport activity probably occurred episodically throughout the cored interval. Types of mass-transport deposits present in MD992301 are cohesive debris flows and turbidites. The most comprehensive mass-transport deposit identified as an ancient debris flow located at the lowermost 125 cm in the core, suggested to been deposited

during the Saalian glaciation. The remaining mass-transport deposits are interpreted as turbidites deposited episodically through the core, with an increase in frequency during the LGM.

- The sedimentation rate is estimated to be largest in a glaciomarine environment during full-scale glaciation, and decreases during interglacials. The lowest accumulation rate calculated within MD992301 is in the uppermost 63 cm deposited during Holocene. Compared to similar work done previously on the Bear Island TMF the rates within the cored interval is estimated to be lower, probably due to a more distal location.
- The INBIS channel is interpreted to have been a turbidity system, and hence, the activity within the channel seems to be restricted to intervals of full-scale glaciation. Within the cored interval four intervals of activity within the channel are recognized. But, it has to be taken into account that only the larger flows will be represented within MD992301, as the flow were able to spill over the confinement of the channel walls onto the overbank area. Activity within the channel are hence not clearly mapped in the retrieved core, and cored samples taken within the channel or at the mouth of the channel may provide a more complete record of channel activity.

## 7. Recommended further work

The results from this study has revealed new information regarding the depositional environment and paleoenvironment in the distal areas of the Bear Island TMF and Storfjorden TMF from the Saalian glaciation to present. The methods applied has given results which requires further research and interpretation to improve the understanding of the area and the activity of the INBIS channel. The recommended further work includes:

- Obtain seismic lines over cores interval to be able to correlate the data.
- More dating will improve the age model, and make it possible to estimate the sedimentation rate further down core. It would also improve the chronology and paleoenvironment reconstruction of the cored area.
- Provide a SEM scan of the sediment pellets to provide more accurate provenance data.
- Track  $\delta O^{18}$  within the core to make it easier to correlate to previous studies.
- Biological studies to study the ecological paleoenvironment: ocean currents, salinity, and temperature.
- Obtain seismic lines and cored samples within the INBIS channel to get a better understanding of the activity within the channel.



## 8. References

- Aagaard, K., & Coachman, L. (1968). The East Greenland Current north of Denmark Strait, Part I. *Arctic*, 21, 181-200.
- Alley, R. B., Blankenship, D. D., Rooney, S. T., & Bentley, C. R. (1989). Sedimentation beneath Ice Shelves - the View from Ice Stream-B. *Marine Geology*, 85(2-4), 101-120.
- Amundsen, H. B., Laberg, J. S., Vorren, T. O., Haflidason, H., Forwick, M., & Buhl-Mortensen, P. (2015). Late Weichselian-Holocene evolution of the high-latitude Andoya submarine Canyon, North-Norwegian continental margin. *Marine Geology*, 363, 1-14.
- Andersen, B. G., & Mangerud, J. (1990). The Last Interglacial-Glacial Cycle in Fennoscandia. *Quaternary International, Vols 3-4*, 21-29.
- Andreassen, K., Laberg, J. S., & Vorren, T. O. (2008). Seafloor geomorphology of the SW Barents Sea and its glaci-dynamic implications. *Geomorphology*, 97(1-2), 157-177.
- Andreassen, K., Odegaard, C. M., & Rafaelsen, B. (2007). Imprints of former ice streams, imaged and interpreted using industry three-dimensional seismic data from the south-western Barents Sea. *Seismic Geomorphology: Applications to Hydrocarbon Exploration and Production*, 277, 151-169.
- Andreassen, K., & Winsborrow, M. (2009). Signature of ice streaming in Bjornoyrenna, Polar North Atlantic, through the Pleistocene and implications for ice-stream dynamics. *Annals of Glaciology*, 50(52), 17-26.
- Barnes, P. W., Reimnitz, E., & Fox, D. (1982). Ice Rafting of Fine-Grained Sediment, a Sorting and Transport Mechanism, Beaufort Sea, Alaska. *Journal of Sedimentary Petrology*, 52(2), 493-502.
- Beckhoff, B., Kanngiesser, B., Langhoff, N., Wedell, R., & Wolff, H. (2006). *Handbook of Practical X-Ray Fluorescence Analysis*: Berlin Heidelberg: Springer-Verlag GmbH.
- Benn, D. I., & Evans, D. J. A. (1998). *Glaciers and Glaciation*: Arnold.
- Berner, H., & Wefer, G. (1990). Physiographic and Biological Factors Controlling Surface Sediment Distribution in the Fram Strait. *Geological History of the Polar Oceans : Arctic Versus Antarctic*, 308, 317-335.
- Bertrand, S., Hughen, K. A., Sepulveda, J., & Pantoja, S. (2012). Geochemistry of surface sediments from the fjords of Northern Chilean Patagonia (44-47 degrees S): Spatial variability and implications for paleoclimate reconstructions. *Geochimica Et Cosmochimica Acta*, 76, 125-146.
- Bjørlykke, K., Bue, B., & Elverhøi, A. (1978). Quaternary Sediments in Northwestern Part of Barents Sea and Their Relation to Underlying Mesozoic Bedrock. *Sedimentology*, 25(2), 227-246.

- Blindheim, J. (1989). Cascading of Barents Sea bottom water into the Norwegian Sea. *Rapp. P. V. Réun. Cons. Int. Explor. Mer.*, 188, 49–58.
- Blindheim, J. (1990). Arctic Intermediate Water in the Norwegian Sea. *Deep-Sea Research Part a-Oceanographic Research Papers*, 37(9), 1475-1489.
- Boulton, G. S. (1978). Boulder Shapes and Grain-Size Distributions of Debris as Indicators of Transport Paths through a Glacier and Till Genesis. *Sedimentology*, 25(6), 773-799.
- Boulton, G. S. (1979). Model of Weichselian Glacier Variation in the North-Atlantic Region. *Boreas*, 8(3), 373-395.
- Bouma, A. (1962). *Sedimentology of some Flysch deposits*. Amsterdam: Elsevier.
- Bowles, F. A., Faas, R. W., Vogt, P. R., Sawyer, W. B., & Stephens, K. (2003). Sediment properties, flow characteristics, and depositional environment of submarine mudflows, Bear Island Fan. *Marine Geology*, 197(1-4), 63-74.
- Bowman, S. (1990). *Radiocarbon dating*. Berkley and Los Angeles: University of California Press.
- Bowman, S., & Balaam, N. (1990). Using Radiocarbon. *Antiquity*, 64(243), 315-318.
- Butt, F. A., Elverhøi, A., Solheim, A., & Forsberg, C. F. (2000). Deciphering late Cenozoic development of the western Svalbard margin from ODP site 986 results. *Marine Geology*, 169(3-4), 373-390.
- Calvert, S. E., & Pedersen, T. F. (2007). Elemental proxies for paleoclimatic and paleoceanographic variability in marine sediments: interpretation and application. In C. Hillaire-Marcel, De Vernal, A. (Ed.), *Developments in Marine Geology: Proxies in late Cenozoic paleoceanography* (Vol. 1st, pp. 567-644): Elsevier.
- Clark, D. L., R. R. Whitman, K. A. Morgan, & Mackay, S. D. (1980). Stratigraphy and glacial-marine sediments of the Amerasian Basin, central Arctic Ocean *Geological Society of America special paper 181*, 57 pp.
- CLIMAP. (1976). The surface of the ice-age earth. *Science*, 191, 1131-1137.
- CLIMAP. (1984). The last interglacial ocean. *Quaternary Research*, 21, 123-224.
- Collinson, J., Mountney, N., & Thompson, D. (2006). *Sedimentary structures* (3rd ed.): Terra Publishing.
- Croudace, I. W., Rindby, A., & Rothwell, G. (2006). ITRAX: description and evaluation of a new multi-function X-ray core scanner. . R. G. Rothwell, *New techniques in sediment core analysis*, Vol. 267(Geological Society, Special Publications), pp. 51-63.
- Denbigh, P. N. (1989). Swath Bathymetry - Principles of Operation and an Analysis of Errors. *IEEE Journal of Oceanic Engineering*, 14(4), 289-298.
- Denton, G. H., & Hughes, T. J. (1981). *The Last Great Ice Sheets*. New York: John Wiley & Sons.

- Dokken, T. M., & Hald, M. (1996). Rapid climatic shifts during isotope stages 2-4 in the Polar North Atlantic. *Geology*, 24(7), 599-602.
- Dowdeswell, J. A. (1989). On the Nature of Svalbard Icebergs. *Journal of Glaciology*, 35(120), 224-234.
- Dowdeswell, J. A., & Dowdeswell, E. K. (1989). Debris in Icebergs and Rates of Glaci-Marine Sedimentation - Observations from Spitsbergen and a Simple-Model. *Journal of Geology*, 97(2), 221-231.
- Dowdeswell, J. A., Hambrey, M. J., & Wu, R. (1985). A Comparison of Clast Fabric and Shape in Late Precambrian and Modern Glacigenic Sediments. *Journal of Sedimentary Petrology*, 55(5), 691-704.
- Elverhøi, A., De Blasio, F. V., Butt, F. A., Issler, D., Harbitz, C., Engvik, L., . . . Marr, J. (2002). Submarine mass-wasting on glacially-influenced continental slopes: processes and dynamics. *Glacier-Influenced Sedimentation on High-Latitude Continental Margins*, 203, 73-87.
- Elverhøi, A., Norem, H., Andersen, E. S., Dowdeswell, J. A., Fossen, I., Hafliðason, H., . . . Vorren, T. (1997). On the origin and flow behavior of submarine slides on deep-sea fans along the Norwegian Barents Sea continental margin. *Geo-Marine Letters*, 17(2), 119-125.
- Elverhøi, A., & Solheim, A. (1983). The Barents Sea ice sheet - a sedimentological discussion. *Polar Research*, 1, 23-42.
- Eyles, N. (2006). The role of meltwater in glacial processes. *Sedimentary Geology*, 190(1-4), 257-268.
- Faleide, J. I., Solheim, A., Fiedler, A., Hjelstuen, B. O., Andersen, E. S., & Vanneste, K. (1996). Late Cenozoic evolution of the western Barents Sea-Svalbard continental margin. *Global and Planetary Change*, 12(1-4), 53-74.
- Faleide, J. I., Tsikalas, F., Breivik, A. J., Mjelde, R., Ritzmann, O., Engen, O., . . . Eldholm, O. (2008). Structure and evolution of the continental margin off Norway and Barents Sea. *Episodes*, 31(1), 82-91.
- Fohrmann, H., Backhaus, J. O., Blaumel, F., Haupt, B. J., Kampf, J., Michels, K., . . . Woodgate, R. (2001). Modern Ocean Current-Controlled Sediment Transport in the Greenland-Iceland-Norwegian (GIN) Seas. In W. R. P. Schafer, M. Schwter and J.Thiede (Ed.), *The Northern North Atlantic: A Changing Environment* (pp. 135-154). Berlin· Heidelberg Springer-Verlag
- Folk, R. (1954). The distinction between grain size and mineral composition in sedimentary rock nomenclature. *The Journal of Geology*, 62, 4 344-359.
- Forsberg, C. F., Solheim, A., Kvalstad, T. J., Vaidya, R., & Mohanty, S. (2007). Slope instability and mass transport deposits on the Godavari river delta, east Indian margin from a regional geological perspective. *Submarine Mass Movements and Their Consequences*, 27, 19-27.
- Forwick, M. (2013a ). How to use XRF core scanner data aquired with the Aavatech XRF core scanner at the Department of Geology.

- Forwick, M., & Vorren, T. O. (2009). Late Weichselian and Holocene sedimentary environments and ice rafting in Isfjorden, Spitsbergen. *Palaeogeography Palaeoclimatology Palaeoecology*, 280(1-2), 258-274.
- Forwick, M., Laberg, J. S., Hass, H. C., & Osti, G. (2015). The Kongsfjorden Channel System offshore NW Svalbard: downslope sedimentary processes in a contour-current-dominated setting. *Arktos: the journal of Arctic geosciences*, 17(1).
- Fronval, T., & Jansen, E. (1997). Eemian and early Weichselian (140-60 ka) paleoceanography and paleoclimate in the Nordic seas with comparisons to Holocene conditions. *Paleoceanography*, 12(3), 443-462.
- Fujifilm. (2014). *Fujifilm Technical Handbook: The Fundamentals of Industrial Radiography*. Tokyo: Fujifilm Corporation.
- Gales, J. A., Larter, R. D., Mitchell, N. C., & Dowdeswell, J. A. (2013). Geomorphic signature of Antarctic submarine gullies: Implications for continental slope processes. *Marine Geology*, 337, 112-124.
- Gard, G., & Backman, J. (1990). Synthesis of Arctic and Sub-Arctic Coccolith Biochronology and History of North-Atlantic Drift Water Influx during the Last 500.000 Years. *Geological History of the Polar Oceans : Arctic Versus Antarctic*, 308, 417-436.
- Gataullin, V., Mangerud, J., & Svendsen, J. I. (2001). The extent of the Late Weichselian ice sheet in the southeastern Barents Sea. *Global and Planetary Change*, 31(1-4), 453-474.
- GEOTEK. (2000). *Geotek Multi-Sensor Core Logger (MSCL) Manual*.
- GEOTEK. (2014a). Manual; Multi-Sensor Core Logger. Retrieved October 12, 2016. Retrieved from <http://www.geotek.co.uk/sites/default/files/MSCLmanual.pdf>
- GEOTEK. (2014b). GEOTEK X-ray Core Imaging with CT MSCL-XCT: Linear images & 3D reconstruction of sediment and rock cores. Retrieved October 12, 2014. Retrieved from [http://www.geotek.co.uk/sites/default/files/Geotek\\_MSCL-XCT.pdf](http://www.geotek.co.uk/sites/default/files/Geotek_MSCL-XCT.pdf)
- Gernigon, L., Olesen, O., Gaina, C., & Wienecke, S. (2009). Atypical post-breakup magmatism along the Jan Mayen Fracture Zone: Do we need a mantle plume? Retrieved February 04, 2016. Retrieved from: <http://www.mantleplumes.org/JanMayen.html>.
- Gilbert, R. (1990). Rafting in Glaciomarine Environments. *Glaciomarine Environments : Processes and Sediments*, 53, 105-120.
- Gingras, M. K., Pemberton, S. G., & Smith, M. (2015). Bioturbation: Reworking of sediments for better or worse. *Oilfield Review*, 26(4), 46-58.
- Goldschmidt, P. M., Pfirman, S. L., Wollenburg, I., & Henrich, R. (1992). Origin of Sediment Pellets from the Arctic Sea-Floor - Sea Ice or Icebergs. *Deep-Sea Research Part a-Oceanographic Research Papers*, 39(2a), 539-565.
- Goldstein, R. H. (1983). Stratigraphy and sedimentology of ice-rafted and turbidite sediment, Canada Basin, Arctic Ocean. In B. F. Molina (Ed.), *Glacial-marine sedimentation* (pp. 367-400. ). London: Springer.

- Gudlaugsson, S. T., Faleide, J. I., Johansen, S. E., & Breivik, A. J. (1998). Late Palaeozoic structural development of the South-western Barents Sea. *Marine and Petroleum Geology*, *15*(1), 73-102.
- Hald, M., Danielsen, T. K., & Lorentzen, S. (1989). Late Pleistocene-Holocene benthic foraminiferal distribution in the southwestern Barents Sea: Paleoenvironmental implication. *Boreas*, *18*, 367-388.
- Hald, M., Dokken, T., & Mikalsen, G. (2001). Abrupt climatic change during the last interglacial-glacial cycle in the polar North Atlantic. *Marine Geology*, *176*(1-4), 121-137.
- Hampton, M. A. (1972). The Role of Subaqueous Debris Flow in Generating Turbidity Currents. *Journal of Sedimentary Petrology*, *42*(4), 775-793.
- Hansen, B., & Osterhus, S. (2000). North Atlantic-Nordic Seas exchanges. *Progress in Oceanography*, *45*(2), 109-208.
- Hebbeln, D., Dokken, T., Andersen, E. S., Hald, M., & Elverhøi, A. (1994). Moisture Supply for Northern Ice-Sheet Growth during the Last-Glacial-Maximum. *Nature*, *370*(6488), 357-360.
- Hebbeln, D., Henrich, R., & Baumann, K. H. (1998). Paleoceanography of the last interglacial/glacial cycle in the Polar North Atlantic. *Quaternary Science Reviews*, *17*(1-3), 125-153.
- Hebbeln, D., & Wefer, G. (1991). Effects of Ice Coverage and Ice-Rafted Material on Sedimentation in the Fram Strait. *Nature*, *350*(6317), 409-411.
- Hebbeln, D., & Wefer, G. (1997). Late Quaternary paleoceanography in the Fram Strait. *Paleoceanography*, *12*(1), 65-78.
- Hennekam, R., & de Lange, G. (2012). X-ray fluorescence core scanning of wet marine sediments: methods to improve quality and reproducibility of high-resolution paleoenvironmental records. *Limnology and Oceanography-Methods*, *10*, 991-1003.
- Henrich, R., Kassens, H., Vogelsang, E., & Thiede, J. (1989). Sedimentary Facies of Glacial-Interglacial Cycles in the Norwegian Sea during the Last 350-Ka. *Marine Geology*, *86*(4), 283-319.
- Henrich, R., Wagner, T., Goldschmidt, P., & Michels, K. (1995). Depositional Regimes in the Norwegian Greenland Sea - the Last 2 Glacial to Interglacial Transitions. *Geologische Rundschau*, *84*(1), 28-48.
- Higham, T., Ramsey, C., Hogg, A., Petchey, F., & Cresswell, R. (2015). Accelerator mass spectrometry (AMS) measurement, Radiocarbon Web-info version 156. Retrived october 22, 2015. Retrived from: <https://c14.arch.ox.ac.uk/embed.php?File=ams.html>.
- Highland, L. M., & Bobrowsky, P. (2008). *The landslide handbook—A guide to understanding landslides*. Reston, Virginia.: U.S. Geological Survey.
- Hodel, K. L., Reimnitz, E., & Barnes, P. W. (1988). Microtextures of Quartz Grains from Modern Terrestrial and Subaqueous Environments, North Slope of Alaska. *Journal of Sedimentary Petrology*, *58*(1), 24-32.

- Hooke, R. L., & Elverhøi, A. (1996). Sediment flux from a fjord during glacial periods, Isfjorden, Spitsbergen. *Global and Planetary Change*, 12(1-4), 237-249.
- Jacobsson, M., Cherkis, N., Woodward, J., Coakley, B., & Macnab, R. (2000). A new grid of Arctic bathymetry: a significant resource for scientists and mapmakers. . *EOS Transactions, American Geophysical Union*, 81, 89, 93, 96.
- Jacobsson, M., Macnab, R., Mayer, L., Anderson, R., Edwards, M., Hatzky, J., . . . Johnson, P. (2008). An improved bathymetric portrayal of the Arctic Ocean: Implications for ocean modeling and geological, geophysical and oceanographic analyses. *Geophysical Research Letters*, 35(7).
- Jessen, S. P., Rasmussen, T. L., Nielsen, T., & Solheim, A. (2010). A new Late Weichselian and Holocene marine chronology for the western Svalbard slope 30,000-0 cal years BP. *Quaternary Science Reviews*, 29(9-10), 1301-1312.
- Johannessen, O. M. (1986). Brief overview of the physical oceanography *The Nordic Seas*. (pp. 103-127). New York: Springer.
- Kellogg, T. B. (1975). Late Quaternary climatic changes in the Norwegian-Greenland Sea. In S. A. B. a. G. Weller (Ed.), *Climate of the Arctic* (pp. 3-36).
- Kellogg, T. B. (1980). Paleoclimatology and Paleo-Oceanography of the Norwegian and Greenland Seas - Glacial-Interglacial Contrasts. *Boreas*, 9(2), 115-137.
- Kneller, B., & Buckee, C. (2000). The structure and fluid mechanics of turbidity currents: a review of some recent studies and their geological implications. *Sedimentology*, 47, 62-94.
- Knies, J., Matthiessen, J., Vogt, C., & Stein, R. (2002). Evidence of 'Mid-Pliocene (similar to 3 Ma) global warmth' in the eastern Arctic Ocean and implications for the Svalbard/Barents Sea ice sheet during the late Pliocene and early Pleistocene (similar to 3-1.7 Ma). *Boreas*, 31(1), 82-93.
- Knies, J., & Vogt, C. (2003). Freshwater pulses in the eastern Arctic Ocean during Saalian and Early Weichselian ice-sheet collapse. *Quaternary Research*, 60(3), 243-251.
- Knight, R. J., & Dalrymple, R. W. (1976). Winter conditions in a macrotidal environment, Cobequid Bay, Nova Scotia. *La Revue de Géographie de Montréal*, 30, 65-85.
- Laberg, J. S., Andreassen, K., Knies, J., Vorren, T. O., & Winsborrow, M. (2010). Late Pliocene-Pleistocene development of the Barents Sea Ice Sheet. *Geology*, 38(2), 107-110.
- Laberg, J. S., Andreassen, K., & Vorren, T. O. (2012). Late Cenozoic erosion of the high-latitude southwestern Barents Sea shelf revisited. *Geological Society of America Bulletin*, 124(1-2), 77-88.
- Laberg, J. S., Guidard, S., Mienert, J., Vorren, T. O., Haflidason, H., & Nygard, A. (2007). Morphology and morphogenesis of a high-latitude canyon; the Andoya Canyon, Norwegian Sea. *Marine Geology*, 246(2-4), 68-85.

- Laberg, J. S., & Vorren, T. O. (1995). Late Weichselian Submarine Debris Flow Deposits on the Bear-Island-Trough-Mouth-Fan. *Marine Geology*, 127(1-4), 45-72.
- Laberg, J. S., & Vorren, T. O. (1996a). The glacier-fed fan at the mouth of Storfjorden trough, western Barents Sea: A comparative study. *Geologische Rundschau*, 85(2), 338-349.
- Laberg, J. S., & Vorren, T. O. (1996b). The Middle and Late Pleistocene evolution of the Bear Island Trough Mouth Fan. *Global and Planetary Change*, 12(1-4), 309-330.
- Lambeck, K., Purcell, A., Funder, S., Kjaer, K. H., Larsen, E., & Moller, P. (2006). Constraints on the Late Saalian to early Middle Weichselian ice sheet of Eurasia from field data and rebound modelling. *Boreas*, 35(3), 539-575.
- Landvik, J. Y., Bondevik, S., Elverhøi, A., Fjeldskaar, W., Mangerud, J., Salvigsen, O., . . . Vorren, T. O. (1998). The last glacial maximum of Svalbard and the Barents Sea area: Ice sheet extent and configuration. *Quaternary Science Reviews*, 17(1-3), 43-75.
- Larsen, E., Kjaer, K. H., Demidov, I. N., Funder, S., Grosfjeld, K., Houmark-Nielsen, M., . . . Lysa, A. (2006). Late Pleistocene glacial and lake history of northwestern Russia. *Boreas*, 35(3), 394-424.
- Larsen, E., Sejrup, H. P., Johnsen, S. J., & Knudsen, K. L. (1995). Do Greenland Ice Cores Reflect NW European Interglacial Climate Variations. *Quaternary Research*, 43(2), 125-132.
- Leeder, M. (2011). *Sedimentology and sedimentary basins; From tubulence to tectonics* (2nd ed.): Wiley-Blackwell.
- Lowe, J. J., & Walker, M. J. C. (1997). *Reconstructing Quaternary Environments* (Vol. 2nd). London and New York: Routledge.
- Lutgens, F. K., & Tarbuck, E. J. (2009). *Essentials of Geology* (11 th ed.): Pearson Education, inc.
- Mangerud, J. (1972). Radiocarbon dating of marine shells, including a discussion of apparent age of Recent shells from Norway. *Boreas*, 1, 143-172.
- Mangerud, J. (1991). The Scandinavian Ice Sheet through the last interglacial/glacial cycle. In B. Frenzel (Ed.), *Klimageschichtliche Probleme der letzten 130,000 Jahre* (pp. 307-330). Stuttgart, New York.
- Mangerud, J. (2004). Ice sheet limits on Norway and the Norwegian continental shelf. In J. Ehlers & P. L. Gibbard (Eds.), *Quaternary Glaciations: Extent and Chronology* (Vol. 1, pp. 271-294). Amsterdam: Elsevier.
- Mangerud, J., Bolstad, M., Elgersma, A., Helliksen, D., Landvik, J. Y., Lønne, I., . . . Svendsen, J. I. (1992). The last glacial maximum on Spitsbergen, Svalbard. *Quaternary Research*, 38, 1-31.
- Mangerud, J., Dokken, T., Hebbeln, D., Heggen, B., Ingólfsson, Ó., Landvik, J. Y., . . . Vorren, T. O. (1998). Fluctuations of the Svalbard-Barents sea ice sheet during the last 150 000 years. *Quaternary Science Reviews*, 17, 11-42.

- Mangerud, J., & Gulliksen, S. (1975). Apparent Radiocarbon Ages of Recent Marine Shells from Norway, Spitsbergen, and Arctic Canada. *Quaternary Research*, 5(2), 263-273.
- Mangerud, J., Jansen, E., & Landvik, J. (1996). Late Cenozoic history of the Scandinavian and Barents Sea ice sheets *Global and Planetary Change*, 12, 11-26.
- Mangerud, J., Sonstegaard, E., Sejrup, H. P., & Haldorsen, S. (1981). A Continuous Eemian-Early Weichselian Sequence Containing Pollen and Marine Fossils at Fjosanger, Western Norway. *Boreas*, 10(2), 137-208.
- Mangerud, J., & Svendsen, J. I. (1992). The last interglacial-glacial period on Spitsbergen, Svalbard. *Quaternary Science Reviews*, 11, 633-664.
- Marum. (2013a). Marum, Center for Marine Environmental Science, "Multi-sensor core logger (MSCL)". Retrived October 07, 2015. Retrieved from [https://www.marum.de/en/Multisensor\\_core\\_logger\\_MSCL.html#Section3742](https://www.marum.de/en/Multisensor_core_logger_MSCL.html#Section3742)
- Marum. (2013b). Marum, Center for Marine Environmental Science , "XRF Core Scanner". Published septemer 26, 2013. Retrieved october 07, 2015. Retrieved from [http://www.marum.de/en/XRF\\_Core\\_Scanner.html](http://www.marum.de/en/XRF_Core_Scanner.html)
- Meiburg, E., & Kneller, B. (2010). Turbidity Currents and Their Deposits. *Annual Review of Fluid Mechanics*, 42, 135-156.
- Miller, G. H., Sejrup, H. P., Lehman, S. J., & Forman, S. L. (1989). Glacial History and Marine Environmental-Change during the Last Interglacial Glacial Cycle, Western Spitsbergen, Svalbard. *Boreas*, 18(3), 273-296.
- Minicucci, D. A., & Clark, D. L. (1983). A Late Cenozoic stratigraphy for glacial-marine sediments of the eastern Alpha Cordillera, central Arctic Ocean. In B. F. Molnia (Ed.), *Glacial-Marine Sedimentation* (pp. 331-365). London: Springer.
- Mulder, T., & Alexander, J. (2001). The physical character of subaqueous sedimentary density flows and their deposits. *Sedimentology*, 48(2), 269-299.
- Nichols, G. (2009). *Sedimentology and stratigraphy* (2 ed.): Wiley-Blackwell.
- Ottesen, D., Dowdeswell, J. A., & Rise, L. (2005). Submarine landforms and the reconstruction of fast-flowing ice streams within a large Quaternary ice sheet: The 2500-km-long Norwegian-Svalbard margin (57 degrees-80 degrees N). *Geological Society of America Bulletin*, 117(7-8), 1033-1050.
- Ottesen, D., Stokes, C. R., Rise, L., & Olsen, L. (2008). Ice-sheet dynamics and ice streaming along the coastal parts of northern Norway. *Quaternary Science Reviews*, 27(9-10), 922-940.
- Pedrosa, M. T., Camerlenghi, A., De Mol, B., Urgeles, R., Rebesco, M., Lucchi, R. G., & Cruises, S. E. (2011). Seabed morphology and shallow sedimentary structure of the Storfjorden and Kveithola trough-mouth fans (North West Barents Sea). *Marine Geology*, 286(1-4), 65-81.

- Pfirman, S., Lange, M. A., Wollenburg, I., & Schlosser, P. (1990). Sea Ice Characteristics and the Role of Sediment Inclusions in Deep-Sea Deposition - Arctic Antarctic Comparisons. *Geological History of the Polar Oceans : Arctic Versus Antarctic*, 308, 187-211.
- Pfirman, S., Wollenburg, I., Thiede, J., & Lange, M. A. (1989). Lithogenic Sediment on Arctic Pack Ice - Potential Aeolian Flux and Contribution to Deep-Sea Sediments. *Paleoclimatology and Paleometeorology : Modern and Past Patterns of Global Atmospheric Transport*, 282, 463-493.
- Pfirman, S. L., Bauch, D., & Gammelsrød, T. (1994). The Northern Barents Sea: Water Mass Distribution and Modification *The Polar Oceans and Their Role in Shaping the Global Environment* (Vol. Geophysical Monograph 85): American Geophysical Union.
- Pfirman, S. L., & Solheim, A. (1989). Subglacial Meltwater Discharge in the Open-Marine Tidewater Glacier Environment - Observations from Nordaustlandet, Svalbard Archipelago. *Marine Geology*, 86(4), 265-281.
- Piper, D. J. W., Cochonat, P., & Morrison, M. L. (1999). The sequence of events around the epicentre of the 1929 Grand Banks earthquake: initiation of debris flows and turbidity current inferred from sidescan sonar. *Sedimentology*, 46(1), 79-97.
- Polarstern Shipboard Scientific Party. (1988). *Breakthrough in Arctic deep-sea research: the R/V Polarstern expedition 1987*.
- Polyak, L., Alley, R. B., Andrews, J. T., Brigham-Grette, J., Cronin, T. M., Darby, D. A., . . . Wolff, E. (2010). History of sea ice in the Arctic. *Quaternary Science Reviews*, 29(15-16), 1757-1778.
- Polyak, L., Lehman, S. J., Gataullin, V., & Jull, A. J. T. (1995). 2-Step Deglaciation of the Southeastern Barents Sea. *Geology*, 23(6), 567-571.
- Polyak, L., & Mikhailov, V. (1996). Post-glacial environments of the southeastern Barents Sea: Foraminiferal evidence. *Late Quaternary Palaeoceanography of the North Atlantic Margins*(111), 323-337.
- Poole, D. A. R., Saettem, J., & Vorren, T. O. (1994). Foraminiferal Stratigraphy, Paleoenvironments and Sedimentation of the Glacigenic Sequence Southwest of Bjornoya. *Boreas*, 23(2), 122-138.
- Rabineau, M., Berne, S., Olivet, J. L., Aslanian, D., Guillocheau, F., & Joseph, P. (2006). Paleo sea levels reconsidered from direct observation of paleoshoreline position during Glacial Maxima (for the last 500,000 yr). *Earth and Planetary Science Letters*, 252(1-2), 119-137.
- Rasmussen, E., & Fjeldskaar, W. (1996). Quantification of the Pliocene-Pleistocene erosion of the Barents Sea from present-day bathymetry. *Global and Planetary Change*, 12(1-4), 119-133.
- Rasmussen, T. L., Thomsen, E., Slubowska, M. A., Jessen, S., Solheim, A., & Koc, N. (2007). Paleoceanographic evolution of the SW Svalbard margin (76 degrees N) since 20,000 C-14 yr BP. *Quaternary Research*, 67(1), 100-114.
- Raukas, A. (1991). Eemian Interglacial record in the Northwestern European part of the Soviet Union. *Quaternary International*, 10-12, 183-189.

- Rebesco, M., Pedrosa, M. T., Camerlenghi, A., Lucchi, R. G., Sauli, C., De Mol, B., . . . Bohm, G. (2012). One Million Years of Climatic Generated Landslide Events on the Northwestern Barents Sea Continental Margin. *Submarine Mass Movements and Their Consequences*, 31, 747-756.
- Reimer, P. J., Bard, E., Bayliss, A., Beck, J. W., Blackwell, P. G., Ramsey, C. B., . . . van der Plicht, J. (2013). Intcal13 and Marine13 Radiocarbon Age Calibration Curves 0-50,000 Years Cal Bp. *Radiocarbon*, 55(4), 1869-1887.
- Reimnitz, E., Kempema, E. W., & Barnes, P. W. (1987). Anchor Ice, Seabed Freezing, and Sediment Dynamics in Shallow Arctic Seas. *Journal of Geophysical Research-Oceans*, 92(C13), 14671-14678.
- Richter, T. O., Van Der Gaast, S., Koster, B., Vaars, A., Gieles, R., De Stiger, H. C., . . . Van Weering, T. C. E. (2006). The Avaatech XRF Core Scanner: technical description and applications to NE Atlantic sediments. In R. G. Rothwell (Ed.), *New Techniques in Sediment Core Analysis* (Vol. Special Publications, 267, pp. 39-50). London: The Geological Society of London.
- Rothwell, R., Hoogakker, B., Thomson, J., Croudace, I., & Frenz, M. (2006). Turbidite emplacement on the southern Balearic Abyssal Plain (western Mediterranean Sea) during Marine Isotope Stages 1-3: an application of ITRAX XRF scanning of sediment cores to lithostratigraphic analysis. *R. rothwell, New techniques in sediment core analysis*, 267, 79-98.
- Rudels, B., & Friedrich, H. J. (2000). The transformations of Atlantic water in the Arctic Ocean and their significance for the freshwater budget. *Freshwater Budget of the Arctic Ocean*, 70, 503-532.
- Sauli, C., Rebesco, M., Camerlenghi, A., Urgeles, R., Diviacco, P., De Mol, B., . . . Lucchi, R. (2010). Thin-skinned and giant submarine landslides on the southern Storfjorden Trough Mouth Fan (Barents Sea). *Geophysical Research Abstracts*, 12, 1.
- Schad, L. (2008). Physics of Imaging Systems Basic Principles of X-Ray Diagnostic I [PowerPoint Slides], Published December 9, 2008. Retrieved October 11, 2015:. Retrieved from [http://www.umm.uniheidelberg.de/inst/cbtm/ckm/lehre/techniquesofimagingystems/2\\_m\\_edphys\\_roen\\_1\\_2sw.pdf](http://www.umm.uniheidelberg.de/inst/cbtm/ckm/lehre/techniquesofimagingystems/2_m_edphys_roen_1_2sw.pdf)
- Shanmugam, G. (2012a). *New perspectives on deep -water sandstones: Origin, recognition, initiation, and reservoir quality* (Vol. 9: 524): Elsevier.
- Shipboard Scientific Party. (1996). Site 986, in Jansen, E., et al., Proceedings of the Ocean Drilling Program. *Initial reports*, 162(Ocean Drilling Program), 287–343.
- Siegert, M. J., Dowdeswell, J. A., Hald, M., & Svendsen, J. I. (2001). Modelling the Eurasian Ice Sheet through a full (Weichselian) glacial cycle. *Global and Planetary Change*, 31(1-4), 367-385.
- Simonsen, K., & Haugan, P. M. (1996). Heat budgets of the Arctic Mediterranean and sea surface heat flux parameterizations for the Nordic Seas. *Journal of Geophysical Research-Oceans*, 101(C3), 6553-6576.
- Slubowska-Woldengen, M., Koc, N., Rasmussen, T. L., Klitgaard-Kristensen, D., Hald, M., & Jennings, A. E. (2008). Time-slice reconstructions of ocean circulation changes on the continental shelf

- in the Nordic and Barents Seas during the last 16,000 cal yr BP. *Quaternary Science Reviews*, 27(15-16), 1476-1492.
- Solheim, A., & Elverhøi, A. (1996). Structure and Lithological composition of Quaternary sediments of the Kara Sea In R. Stein, G. Ivanov, M. Levitan, & K. Fahl (Eds.), *Surface-sediment composition and sedimentary processes in the central Arctic Ocean and along the Eurasian Continental Margin. Reports on Polar Research* (Vol. 212, pp. 144-158). Bremerhaven: Alfred Wegener Institute
- Solheim, A., Faleide, J. I., Andersen, E. S., Elverhøi, A., Forsberg, C. F., Vanneste, K., . . . Channell, J. E. T. (1998). Late Cenozoic seismic stratigraphy and glacial geological development of the East Greenland and Svalbard Barents Sea continental margins. *Quaternary Science Reviews*, 17(1-3), 155-184.
- Solheim, A., Russwurm, L., Elverhøi, A., & Berg, M. N. (1990). Glacial Geomorphic Features in the Northern Barents Sea - Direct Evidence for Grounded Ice and Implications for the Pattern of Deglaciation and Late Glacial Sedimentation. *Glacimarine Environments : Processes and Sediments*, 53, 253-268.
- Stefansson, V. (1921). *The friendly Arctic*. New York: Macmillan Company.
- Stoner, J., Channell, J., & Hillaire-Marcel, C. (1996). The magnetic signature of rapidly deposited detrital layers from the deep Labrador Sea: Relationship to North Atlantic Heinrich layers. . *Paleoceanography*, 11, 3, 309-325.
- Stuvier, M., Reimer, P., & Reimer, R. (2016). CALIB Radiocarbon Calibration. Retrieved from Marine Reservoir Correction Database. Retrieved May 4th 2016. Retrieved from: <http://calib.qub.ac.uk/calib/>.
- Svendsen, J. I., Alexanderson, H., Astakhov, V. I., Demidov, I., Dowdeswell, J. A., Funder, S., . . . Stein, R. (2004). Late quaternary ice sheet history of northern Eurasia. *Quaternary Science Reviews*, 23(11-13), 1229-1271.
- Svindland, K. T., & Vorren, T. O. (2002). Late Cenozoic sedimentary environments in the Amundsen Basin, Arctic Ocean. *Marine Geology*, 186(3-4), 541-555.
- Swift, J. H. (1986). The Arctic Waters. In B. G. Hurdle (Ed.), *The Nordic Seas* (pp. 129-153): Springer-Verlag.
- Sætre, R., & Ljøen, R. (1972). The Norwegian Coastal Current *Port and ocean engineering under arctic conditions* (pp. 514-535). Bergen: The Technical University of Norway.
- Sættem, J., Poole, D. A. R., Ellingsen, L., & Sejrup, H. P. (1992). Glacial Geology of Outer Bjornoyrenna, Southwestern Barents Sea. *Marine Geology*, 103(1-3), 15-51.
- Taylor, J., Dowdeswell, J. A., & H, K. N. (2003). Canyon and Channel Systems in the Lofoten Basin, Norwegian Margin *European Margin Sediment Dynamics* (pp. 93-97): Springer Berlin Heidelberg.
- Taylor, J., Dowdeswell, J. A., & Kenyon, N. H. (2000). Canyons and late Quaternary sedimentation on the North Norwegian margin. *Marine Geology*, 166(1-4), 1-9.

- Taylor, J., Dowdeswell, J. A., & Siebert, M. J. (2002). Late Weichselian depositional processes, fluxes, and sediment volumes on the margins of the Norwegian Sea (62-75 degrees N). *Marine Geology*, 188(1-2), 61-77.
- Thiede, J., Winkler, A., Wolf-Welling, T., E., O., M., A.M., B., . . . Stein, R. (1998). Late Cenozoic history of the Polar North Atlantic: results from ocean drilling. *Quaternary Science Reviews*, 17, 185-208.
- Tjallingii, R., Rohl, U., Kolling, M., & Bickert, T. (2007). Influence of the water content on X-ray fluorescence core-scanning measurements in soft marine sediments. *Geochemistry Geophysics Geosystems*, 8.
- Udden, J. (1914). Mechanical composition of clastic sediments. *The Geological Society of America Bulletin*, 25, 543-548.
- Vorren, T., & Mangerud, J. (2008). Glaciations come and go. Pleistocene, 2.6 million-11,500 years ago. In I. Ramberg, Bryhni, I., Nøttvedt, A., Rangnes, K. (Ed.), *The Making of a Land-Geology of Norway* (pp. 480-533). Trondheim: Norsk Geologisk Forening.
- Vorren, T. O., Hald, M., Edverdsen, M., & Lind-Hansen, O. W. (1983). Glacigenic sediments and sedimentary environments of continental shelves: General principles with a case study from the Norwegian shelf. In E. J. (Ed.), *Glacial deposits in Northwest Europe* (pp. 61-73): Balkema.
- Vorren, T. O., Hald, M., & Thomsen, E. (1984). Quaternary Sediments and Environments on the Continental-Shelf Off Northern Norway. *Marine Geology*, 57(1-4), 229-257.
- Vorren, T. O., & Kristoffersen, Y. (1986). Late Quaternary Glaciation in the Southwestern Barents Sea. *Boreas*, 15(1), 51-59.
- Vorren, T. O., & Laberg, J. S. (1996). Late glacial air temperature, oceanographic and ice sheet interactions in the southern Barents Sea region. *Late Quaternary Palaeoceanography of the North Atlantic Margins*(111), 303-321.
- Vorren, T. O., & Laberg, J. S. (1997). Trough mouth fans - Palaeoclimate and ice-sheet monitors. *Quaternary Science Reviews*, 16(8), 865-881.
- Vorren, T. O., Laberg, J. S., Blaume, F., Dowdeswell, J. A., Kenyon, N. H., Mienert, J., . . . Werner, F. (1998). The Norwegian Greenland Sea continental margins: Morphology and late Quaternary sedimentary processes and environment. *Quaternary Science Reviews*, 17(1-3), 273-302.
- Vorren, T. O., Lebesbye, E., Andreassen, K., & Larsen, K. B. (1989). Glacigenic Sediments on a Passive Continental-Margin as Exemplified by the Barents Sea. *Marine Geology*, 85(2-4), 251-272.
- Vorren, T. O., & Plassen, L. (2002). Deglaciation and palaeoclimate of the Andfjord-Vagsfjord area, North Norway. *Boreas*, 31(2), 97-125.
- Vorren, T. O., Richardsen, G., Knutsen, S. M., & Henriksen, E. (1990). The Western Barents Sea during the Cenozoic. *Geological History of the Polar Oceans : Arctic Versus Antarctic*, 308, 95-118.

- Vorren, T. O., Richardsen, G., Knutsen, S. M., & Henriksen, E. (1991). Cenozoic Erosion and Sedimentation in the Western Barents Sea. *Marine and Petroleum Geology*, 8(3), 317-340.
- Wacker, L., Lippold, J., Molnár, M., & Schulz, H. (2013). Towards radiocarbon dating of single foraminifera with a gas ion source. *Nuclear Instruments and Methods in Physics Research B*, 294, 307-310.
- Walker, R. G., & Phil, D. (1965). The origin and significance of the internal sedimentary structures of turbidites. *Yorkshire Geological Society*, 35, 1-32.
- Watts, A. (2010). Greenland glaciers – melt due to sea current change, not air temperature. Watts Up With That? Retrieved November 3, 2015. Retrieved from <http://wattsupwiththat.com/2010/02/16/greenland-glaciers-melt-due-to-sea-currentchange-not-air-temperature/>
- Weltje, G. J., & Tjallingii, R. (2008). Calibration of XRF core scanners for quantitative geochemical logging of sediment cores: Theory and application. *Earth and Planetary Science Letters*, 274(3-4), 423-438.
- Wentworth, C. (1922). A scale of grade and class terms for clastic sediments. *Journal of Geology*, 377-392.
- Winsborrow, M. C. M., Andreassen, K., Corner, G. D., & Laberg, J. S. (2010). Deglaciation of a marine-based ice sheet: Late Weichselian palaeo-ice dynamics and retreat in the southern Barents Sea reconstructed from onshore and offshore glacial geomorphology. *Quaternary Science Reviews*, 29(3-4), 424-442.
- Worthington, L. V. (1970). Norwegian-Sea as a Mediterranean Basin. *Deep-Sea Research*, 17(1), 77-84.



## Appendix 1

Unit	Lithology	Si/sum	S/sum	Ca/sum	Mn/sum	Fe/sum	Zr/sum	Ca/Fe	Sr/Ca	K/Rb	Zr/Rb
Unit 14	Hemipelagic mud	Decrease	Uniform	Increase	Uniform	Decrease	Uniform	Uniform	Increase	Uniform	Increase
Unit 13	Sand	Uniform	Uniform	Decrease	Increase	Increase	Increase	Increase	Uniform	Increase	Increase
Unit 12	Glaciomarine mud	Decrease	Uniform	Decrease							
Unit 11	Graded sand	Increase	Increase	Decrease	Increase	Increase	Increase	Increase	Uniform	Increase	Uniform
Unit 10	Glaciomarine mud	Uniform									
Unit 9	Glaciomarine mud	Uniform	Uniform	Uniform	Increase	Uniform	Uniform	Uniform	Uniform	Uniform	Uniform
Unit 8	Glaciomarine mud	Uniform									
Unit 7	Graded sand	Increase	Uniform	Uniform	Uniform	Increase	Increase	Increase	Uniform	Uniform	Increase
Unit 6	Glaciomarine mud	Uniform	Uniform	Increase	Uniform						
Unit 5	Sandy layer	Decrease	Increase	Uniform	Uniform	Uniform	Increase	Uniform	Increase	Uniform	Decrease
Unit 4	Hemipelagic mud	Increase	Uniform	Uniform	Uniform	Uniform	Uniform	Uniform	Increase	Uniform	Uniform
Unit 3	Graded sand	Decrease	Uniform	Uniform	Uniform	Increase	Uniform	Increase	Decrease	Uniform	Decrease
Unit 2	Sediment pellets (mud)	Decrease	Increase	Uniform	Increase	Uniform	Uniform	Decrease	Decrease	Uniform	Decrease
Unit 1	Debris flow diamicton (mud)	Increase	Increase	Uniform	Uniform	Uniform	Uniform	Increase	Uniform	Uniform	Uniform

Table 1: Table showing the geochemical composition through the core.

